Question 26

MV-6570-001, Rev. A

PROBABILISTIC EVALUATION OF THE CRYSTAL RIVER POWER STATION CONTAINMENT PERFORMANCE FOR BEYOND DESIGN BASIS CONDITIONS

Prepared for:

RISK MANAGEMENT ASSOCIATES
2309 Dietz Farm Road N. W.
Albuquerque, New Mexico 87107

Prepared by:

ABB IMPELL CORPORATION
27401 Los Altos Suite 480
Mission Viejo, California 92691

D. A. Wesley
D. K. Nakaki
H. Hadidi-Tamjed
S. Lu

March, 1991

ABB
ASEA BROWN BOVERI
ABB Impell Corporation

27401 Los Altos, Suite 480
Mission Viejo, California 92691

Telephone (714) 582-9178
Fax (714) 582-1083

IMPELL CORPORATION

REPORT APPROVAL COVER SHEET

CLIENT: RISK MANAGEMENT ASSOCIATES

PROJECT: Crystal River Unit 3 Containment Overpressure Evaluation

JOB NUMBER(S): 6570-001-1359

REPORT TITLE: PROBABILISTIC EVALUATION OF THE CRYSTAL RIVER POWER STATION CONTAINMENT PERFORMANCE FOR BEYOND DESIGN BASIS CONDITIONS

REPORT NUMBER: MV-6570-001

REVISION RECORD

REV.	PREPARED	REVIEWED	APPROVED	DATE
A	Hassan Hadidi-T	David F. Nakahiki	D A Wesley	3/1/91

Effective 06/88

TABLE OF CONTENTS

RECORD OF REVISIONS

Revision No.	Description
A	Original issue of draft report

LIST OF TABLES

ABSTRACT

A probabilistic evaluation of the Crystal River Unit 3 Nuclear Power Station containment performance has been conducted in support of a probabilistic safety assessment program. Potential failure modes of the reactor building due to temperature and pressure loadings well beyond the design basis conditions were considered in this evaluation. In all cases, failure was defined to be incipient leakage or a breach of the pressure boundary. The failure modes considered were gross structural failures of the concrete containment structure. Smaller, local failures at the containment penetrations were not considered. The capacities of the various failure modes were described in terms of the internal containment pressure required to induce failure. It was assumed that the pressure capacities associated with all of the failure modes could be treated as quasi-static. No dynamic amplification effects of the pressure loading were considered. Three temperature cases were considered in which the interior containment temperatures were assumed to be 300°, 500°, and 800° F. The temperature conditions considered in this investigation were assumed to correspond to steady state material temperatures.

To fit within the context of a probabilistic safety assessment, the pressure capacities of the respective failure modes were treated as lognormally distributed random variables, with the distribution of each pressure capacity described by a median (50th percentile) pressure and a logarithmic standard deviation. The logarithmic standard deviation represented the uncertainty in the median value due to variability in the material properties and analytical modeling. This formulation allows for the probability of failure to be estimated as a function of pressure for each of the failure modes. Thus, in this investigation, the median pressure capacities and logarithmic standard deviations are estimated for the potential failure modes.

Several potential failure modes of the concrete containment structure were evaluated. The failure modes of the reactor building shell and the basemat included: membrane tension failures of the cylinder and dome portions of the shell, flexural failure at the base of

the containment wall, and flexure and shear failures of the basemat. All of these failure modes corresponded to gross structural failures and were assumed to lead to large leak areas and rapid depressurization of the containment.

Overall, by ranking the potential failure modes by their median pressure capacities, the controlling failure mode identified in this study was associated with the flexural failure of the wall-basemat junction. However, by ranking the potential failure modes by their High Confidence of Low Probability of Failure (HCLPF) capacities, the controlling failure mode for the first two temperature cases was the basemat flexural failure, while that for the third temperature case was the wall-basemat junction flexural failure.

1. INTRODUCTION

A probabilistic safety assessment is being conducted for the Crystal River Nuclear Power Station to estimate the risk arising from a release of radioactivity from the site. ABB Impell Corporation is under contract with Risk Management Associates to evaluate the capacity of the Crystal River Unit 3 containment structure for elevated temperature and pressure loadings. Consistent with the nature of the probabilistic safety assessment, the evaluation methodology is based on estimating the capacity of the containment structure in terms of probabilistic parameters.

The Crystal River containment structure is a pre-stressed concrete shell having the form of a circular cylindrical shell capped by a torispherical dome. The inside radius of the concrete cylinder and the dome is 65 feet. The cylinder wall is 3.5 feet thick, while the dome is 3.00 feet thick. The springline for the dome is located 157 feet above the top of the basemat. The containment is lined with a 3/8 inch thick mild, ductile steel plate. In the containment shell, the primary structural resistance is provided by unbonded, post-tensioned tendons in both the hoop and meridional directions. The basemat is a 12.5 feet thick conventional reinforced concrete foundation mat.

This report documents the evaluation of the probabilistic capacity of the containment structure. Several potential failure modes were investigated for the containment in which failure was defined as incipient leakage or a breach of the pressure boundary. Failure resulting from direct pressure induced modes such as membrane building shell failure was considered only. Failure from indirect, deformation induced modes such as pipe penetration failure resulting from the relative deformation of the building shell and the essentially stationary pipe support, either inside or outside the containment, was not considered. Thus, the failure modes included only gross structural failures and not smaller leak failures. These failure modes are evaluated for temperature conditions well in excess of the design accident temperature. Median (50th percentile) failure pressures and their associated variabilities are estimated. Using these values, the probability of failure can be estimated as a function of pressure for the controlling failure modes.

For the investigation reported here, it was assumed that the failure pressures associated with all modes of failure could be treated as quasi-static (i.e., pressure rise times of at least several seconds are assumed). Effects such as dynamic amplification of the pressure pulse on the reactor building shell or internal pressure wave loading on cables and equipment are not considered here. In addition, all temperatures in the materials were assumed to correspond to steady state conditions.

2. PROBABILISTIC DESCRIPTION OF CAPACITY

In order to fit into the probabilistic safety assessment context, a probabilistic description of the pressure capacity of the containment structure is required. Also, since the pressure capacity is treated as a random variable, it is possible for more than one failure mode to significantly contribute to the overall risk. Therefore, several potential failure modes must be evaluated. This section discusses how the capacities are described in a probabilistic form.

2.1 Development of Failure Probabilities

The pressure capacities are evaluated using limit state analyses for the various failure modes considered. In this investigation, failure is interpreted as incipient leakage due to a large catastrophic rupture. The calculated capacities are dependent on several factors, including the material properties, modeling assumptions, and the postulated failure criteria. A major source of uncertainty in the failure criteria is the expected strain resulting in failure. Biaxial strains, gage length effects, and strain concentrations can greatly reduce the expected strain at failure when compared to the elongation data developed from standard specimen ultimate tests. Considerable variability is introduced, not only in the failure criteria but in analytical modeling and other assumptions as well. In view of the expected variability in the base parameters and the analytical methods, the pressure capacity for any failure mode is considered to be a random variable. It is assumed that the pressure capacities are characterized by a lognormal probability distribution. The lognormal distribution is a mathematically tractable distribution and has been shown to be a valid description for the variability in material strengths. In addition, for a random variable that can be expressed as the product and quotient of several random variables, the distribution of the dependent variable tends to be lognormal regardless of the distributions of the independent base variables.

With the pressure capacity for a given failure mode assumed to be a lognormal random variable and denoting it as P, the probability of failure occurring at a pressure less than a specific value p is expressed as

$$P_f = \text{Prob}(P \le p) = \Phi\left[\frac{\ln(p/\hat{P})}{\beta}\right] \qquad (2\text{-}1)$$

where

P_f = probability that failure occurs at a pressure $P \le p$

P = random pressure capacity

β = logarithmic standard deviation of P

$\hat{P}$ = median (50th percentile) pressure capacity

$\Phi(\cdot)$ = cumulative distribution function for a standard normal random variable

In equation (2-1), the pressure capacity for a given failure mode is probabilistically described by the following expression

$$P = \hat{P} \cdot M \cdot S \qquad (2\text{-}2)$$

In the above equation, $\hat{P}$, the median pressure capacity, represents the internal pressure level for which there is a 50% probability of failure, or equivalently, the best estimate of the pressure capacity. M is a lognormally distributed random variable having a unit median value and a logarithmic standard deviation, β_M, which represents the uncertainty due to analytical modeling. S is also a lognormally distributed random variable having a unit median value and the logarithmic standard deviation, β_S, representing the uncertainty associated with the material properties. The overall uncertainty in the pressure capacity is obtained by taking the square root of the sum of the squares of β_M and β_S.

$$\beta = (\beta_M^2 + \beta_S^2)^{1/2} \qquad (2\text{-}3)$$

As a result, the probabilistic pressure capacity is described by three parameters: the median pressure, the modeling uncertainty, β_M, and the material strength uncertainty, β_S.

The logarithmic standard deviations, β_M and β_S, quantify the variability due to a lack of knowledge resulting from differences between the analytical model and the real structure. Modeling uncertainties are introduced by assumptions used to develop analytical models and their ability to adequately represent the failure condition. The strength uncertainties correspond to variabilities related to material resistance. Examples of the sources of such uncertainties include: variability in concrete strength, steel yield strength, stress-strain relationships, and the influence of temperature on material strength.

2.2 Variability in Material Properties

Test data on the strengths of the structural materials of the Crystal River nuclear power station are presented in References 4 and 5. These data included the sample data points for the liner (Ref. 4), and the concrete (Ref. 5). Using these data, the sample statistics (mean and standard deviation) were evaluated for the characteristic material strengths. The median values and logarithmic standard deviations were then evaluated, with the assumption that all of the material strengths could be characterized by a lognormal distribution. Appendix A contains a brief discussion on the features of the lognormal distribution and the relationship between the median and the logarithmic standard deviation and the sample statistics. For the tendons and the reinforcing, the information provided in Reference 1 was supplemented by generic data available in the literature (References 3, 6, and 8).

In References 4, and 5, the material strength test data corresponded to room temperature conditions. Since higher temperatures are considered in this investigation, it was necessary to estimate the influence of elevated temperatures on the Crystal River materials. This was accomplished by estimating temperature dependent strength reduction factors from other available data on the same materials. Given a median characteristic material strength at room temperature, $\hat{S}_{RM,T}$, the median material strength at a higher temperature was estimated by

$$\hat{S}_T = \hat{R}_T \cdot \hat{S}_{RM.T} \qquad (2\text{-}4)$$

where $\hat{R}_T$ is the median temperature strength reduction factor. Noting that there is uncertainty in both the material strength at room temperature and in the reduction factor, the overall logarithmic standard deviation of the material strength at the elevated temperatures was estimated as

$$\beta_S = \left(\beta_{R_T}^2 + \beta_{RM.T}^2\right)^{1/2} \qquad (2\text{-}5)$$

in which β_{R_T} is the logarithmic standard deviation associated with the temperature strength reduction factor and $\beta_{RM.T}$ is the logarithmic standard deviation of the material strength at room temperature.

The following subsections discuss the estimated median values and the logarithmic standard deviations for the various structural materials.

2.2.1 Prestressing Tendons

The typical prestressing tendon consists of 163 7-mm diameter low relaxation wires. These wires conform to ASTM A 421-65 Type BA (Reference 1) with a minimum ultimate tensile stress of 240 ksi. The characteristic minimum ultimate strength of the typical tendon is 2333.5 kips. No sample test data were available.

The median failure criterion for the tendons was estimated as 3% strain, which is 75% of the code minimum elongation reported in Reference 10 for A 421 low relaxation tendons. The median strength of the tendons at 3% strain was estimated to be 2205.2 k at room temperature, with a logarithmic standard deviation of 0.03.

Since the elevated temperature conditions are considered in this investigation, the loss in strength at higher temperatures was estimated using data contained in Reference 2.

2.2.2 Reinforcing Bars

Low tensile strength, deformed reinforcing bars were specified for the Crystal River reactor building. The mild steel reinforcing used was ASTM A 615-68 Grade 40 bars with minimum yield point of 40 ksi and minimum tensile strength of 70 ksi (Reference 1). Based on test data for Grade 40 bars (Reference 11), the median yield strength is estimated as follows:

$$f_y = 1.2 f_{y\,min} = 1.2(40) = 48 \quad ksi$$

Hence, the uncertainty associated with the median value are given by:

$$\beta_y = -\frac{1}{1.65} \ln(1.0/1.2) = 0.11$$

In other words, the code minimum values are considered to represent 95% lower bound values.

In order to estimate the reduction in strength and the added variability with elevated temperatures, the data in Reference 2 was used.

2.2.3 Liner Plate

The reactor building wall is lined with a 3/8 in. thick steel plate in the cylinder and dome portion which becomes 1/4" on the base mat floor. The transition knuckle plate between the wall and the base mat is 3/4" thick. The liner material conformed to the ASTM A 283 Grade C steel. Test data on the yield and tensile strengths of the liner plate was provided by Chicago Bridge & Iron Company (Referece 4). Based on these test results, a median yield stress of 44.6 ksi and an associated logarithmic standard deviation of 0.08 were estimated for the liner in the room temperature.

The appropriate reductions in the yield stress for elevated temperatures were estimated from the values given in the ASME Boiler and Pressure Vessel Code (Reference 3).

2.2.4 Concrete

The concrete specified for the reactor building shell and basemat has a minimum design 28 days compressive strength of 5000 psi (Reference 1). Typically, the actual in-place concrete will have a compressive strength substantially higher than the specified strength. There are two primary reasons for this. First, the contractor mixing the concrete will try to produce a concrete batch such that the average compressive strength is somewhat greater than the specified strength. Second, as concrete ages, it gains strength.

Test data were available on the in-place compressive strength of the dome concrete (Reference 5). Using this data, mean and coefficient of variation of the concrete compressive strength were calculated to be 6301 psi and 0.08, respectively. Based on a lognormal distribution, these in turn result in the median and logarithmic standard deviation values of 6280 psi and 0.08, respectively. Note that these values include the aging effects on the concrete strength, since the data were based on core samples from the dome.

The effect of temperature on the concrete compressive strength was based on the results reported in Reference 7. According to these results, concrete retains at least 80% of its original compressive strength at temperatures up to 800 °F. Therefore, the median concrete compressive strength at higher than room temperatures was taken as the 80% of the median value at room temperature or 5020 psi. In addition, a logarithmic standard deviation value of 0.10 was used to represent the additional uncertainties introduced due to the elevated temperatures resulting in total uncertainty of 0.13 as follows:

$$(0.08^2 + 0.10^2)^{1/2} = 0.13$$

It is assumed that the above median compressive strength and uncertainty are representative of the concrete in the reactor building wall, dome, and basemat.

2.3 Modeling Variability

Uncertainties will exist in the estimated pressure capacities due to differences between the analytical idealization of the structure and the real conditions. There are numerous possible sources of modeling uncertainties. Examples of the possible sources include: assumptions used to develop internal force distributions, failure criteria, and use of empirical formulae. Moreover, since they are dependent on the particular failure mode under consideration, they must be evaluated on a case-by-case basis. However, in many instances, the evaluation of these uncertainties would require very detailed analysis and/or extensive data which may not be available. As a result, it was necessary to use subjective evaluation and engineering judgment to estimate these uncertainties. The evaluation of the modeling uncertainties associated with the median pressure capacities is included in the discussion of the specific failure modes in the subsequent sections.

3. ANALYSIS OF REACTOR BUILDING CAPACITY

The capacity of the Crystal River reactor building is estimated based on incipient leakage as the failure criterion. In this section, several potential failure modes are investigated. The controlling failure modes are ranked according to their respective median pressure capacities, in which the loads considered include temperature, pressure, and dead load. The effects of temperature are treated by including the reduction in material strengths with elevated temperatures. The failure modes examined include:

1. Membrane failures of the containment shell
2. Failure at the containment wall - basemat junction
3. Failure of the basemat

All of the failure modes evaluated here were considered to be quasi-static. In other words, the pressure rise times were assumed to be of sufficient duration such that the dynamic response characteristics of the containment shell could be neglected and the temperatures in the material were assumed to have reached steady state. The failure modes evaluated in this section are associated with gross structural failure leading to rapid depressurization of the containment.

The median pressure capacities and the associated variabilities were evaluated for three temperature conditions; temperatures at the inside face of the wall of 300°, 500°, and 800° F. The corresponding temperatures at the outside face of the concrete wall were assumed to be 70°, 100°, and 200° F, respectively. The interior temperatures were selected to cover a range from the design basis temperature up to the temperatures postulated for severe accidents in typical PWR containments. Note that the wall temperatures are actual material temperatures rather than gas temperatures. In the following discussion, the temperature cases will be denoted as cases 1, 2, and 3 corresponding to the interior temperatures of 300°, 500°, and 800° F, respectively. Since the maximum interior temperature under the design basis accident was 281° F (Reference 1), the temperatures considered in this investigation are well beyond the design basis conditions.

3.1 Membrane Failures of the Reactor Building Shell

In order to estimate the membrane capacities of the containment shell, several issues must first be addressed, which include: the median failure criteria for the structural elements, the initial in-service state of stress and strain in the tendons, the stress-strain behavior of the reinforcing and liner, the temperature distribution through the concrete wall, and the thermal strains in the liner. Since the failure modes are associated with membrane tension, only the liner, the tendons, and the bonded reinforcing are assumed to provide resistance to the internal pressure. No credit was taken for the tensile strength of the concrete. Although design codes such as Division 2 of the ASME Boiler and Pressure Vessel Code do not permit inclusion of the liner strength in the containment design, it was included in the evaluation of the actual ultimate pressure capacities considered here.

The membrane strength of the reactor building shell is provided primarily by the pre-stressing tendons. The median failure strain for the tendons was taken to be 3%. By comparison, the expected uniaxial elongation capacity of the liner and the bonded reinforcing are both substantially larger than that for the tendons. Therefore, the median strain limit for the tendons was selected as the critical failure criterion. Noting that the median failure strain for the tendons was taken as 3%, the strains in the liner and the bonded reinforcing are expected to be between their respective yield and ultimate strains. However, to evaluate the contribution of the liner and the reinforcing to the overall membrane strength, the effect of strain hardening was neglected. In other words, at failure, both the liner and the reinforcing were assumed to be at their respective yield stresses. This greatly simplifies the calculations while introducing a relatively small amount of conservatism in the results.

The primary effect of the elevated temperatures was a reduction of the material strengths. Given the assumed temperatures at the inside and outside faces of the concrete wall for the different temperature cases, the liner, the tendons, and the bonded reinforcing will be at different temperatures. To estimate the temperatures of the different materials, a linear temperature gradient was assumed through the concrete wall and each material was treated as a distinct layer. In this way, the temperature of each material could be estimated by linear interpolation and an appropriate temperature dependent material strength reduction factor could be applied to the characteristic material stress.

Because the interior temperatures considered in this investigation are significantly higher than the exterior temperatures, the liner temperatures are much higher than the average temperature of the concrete wall. As a result, the thermal expansion of the liner is restrained by the concrete and compressive strains are induced in the liner due to temperature effects alone. There are also additional liner compressive strains due to prestressing and concrete creep and shrinkage. This tends to counteract the strains induced in the liner by the internal pressure, since the pressure will produce membrane tension in the liner. However, these compressive strains are small in comparison with the final liner strains at tendon rupture.

3.1.1 Hoop Membrane Failure in the Cylinder Wall

The critical section of the cylindrical portion of the reactor building wall was taken to be approximately at midheight of the cylinder. This section is the least influenced by the end effects caused by the basemat and the dome. At the midheight of the wall, the bonded reinforcement in both the hoop and meridional directions is provided by #8 bars at 12 inches, at both the inside and outside faces.

The hoop tendons have a typical spacing of 1'-1" and span approximately 120° circumferentially between the anchorage points at the buttresses. The hoop tendons are staggered such that, at any vertical cross section, two tendons act over a tributary length of 3'-3".

At tendon failure, the reinforcing bar forces were taken as the yield strength of the bars, since they were in uniaxial (hoop) strain. At the tendon failure condition, the liner is in biaxial tension and the hoop stress in the liner was estimated from the von Mises stress (an equivalent uniaxial stress), which is given by

$$\sigma_e = \frac{1}{\sqrt{2}}[(\sigma_r - \sigma_\theta)^2 + (\sigma_\theta - \sigma_z)^2 + (\sigma_z - \sigma_r)^2]^{1/2} \qquad (3\text{-}1)$$

Making the assumption of a stress distribution equal to that for an ideal cylinder subjected to internal pressure, the relationship between the liner hoop stress and the meridional stress was taken to be $\sigma_z = \frac{1}{2}\sigma_\theta$ and $\sigma_r = 0$. Substituting these values into Equation (3-1) led to a relationship between the liner hoop stress and the von Mises stress as

$$\sigma_\theta = 1.155\sigma_e$$

The von Mises stress, σ_e, was estimated as the uniaxial liner yield stress. In turn, the liner hoop stress was estimated.

The hoop membrane capacity of the containment wall was then estimated from the hoop tensile resistance provided by the tendons, the bonded reinforcing, and the liner. It was found that the hoop tendons provide approximately 80% of the total hoop resistance. The median pressure capacities for the three temperature cases are shown in Tables 3-1, 3-2, and 3-3.

The modeling variabilities included uncertainty in the tendon failure strain, and uncertainty in the temperature and internal force distribution. A logarithmic standard deviation of 0.06 was used to represent the modeling uncertainty in the failure criterion. This was based on the tendons constituting about 80% of the total hoop resistance and that tendons typically exhibit a relatively small amount of strain hardening behavior as well as relatively small scatter in their ultimate strength capacities. The uncertainty in the temperature and the internal force distribution was estimated to have a β value of 0.08. Therefore, the overall modeling uncertainty for the hoop membrane failure mode was estimated as

$$\beta_M = (0.06^2 + 0.08^2)^{1/2}$$
$$= 0.10$$

The material strength variability has contributions from each of the components providing hoop resistance. The reinforcing and the liner have larger uncertainties than the tendons. Since the tendons resisted about 80% of the hoop load, it would be overly conservative to directly combine the individual variabilities of the materials by the square root of

the sum of the squares (SRSS) method. Therefore, the overall material strength uncertainty was estimated by weighting the individual β values (including the uncertainty due to temperature) by the relative contributions of the respective materials to the total hoop resistance. Using this approach, the net variability in the hoop pressure capacity due to material strength was approximately equal to the uncertainty in the tendon strength. Thus, for each of the temperature cases, the logarithmic standard deviation associated with material strength, β_S, was estimated to be 0.06 as shown in Tables 3-1, 3-2, and 3-3.

Also shown in Tables 3-1 through 3-3 are pressure levels corresponding to a high confidence of low probability of failure (HCLPF). These pressure levels correspond to values of ultimate pressure which would be expected from a conservative deterministic analysis of the individual failure modes. These HCLPF values were determined based on the rather arbitrary assumption of a 95% confidence level. That is, based on the estimated median pressure capacity and the associated logarithmic standard deviations for a given failure mode, there is an estimated 95% confidence that the random pressure capacity is greater than the HCLPF value, or equivalently, an estimated 5% confidence that the random pressure capacity is less than or equal to the HCLPF value.

3.1.2 Meridional Membrane Failure in the Cylinder Wall

As with the hoop failure evaluation, the critical section of the wall was taken to be approximately at midheight of the cylinder (midheight between the springline and the top of the basemat). The meridional bonded reinforcing was provided by #8 bars at a 12" spacing at both the inside and outside faces of the wall. The meridional tendons in the cylinder run vertically and are anchored at the tendon gallery below the basemat and at the ring girder located at the springline. Through any horizontal cross section in the cylinder, there are a total of 144 vertical tendons, which are set on a circle having a radius of 67'-3 3/8" with a circumferential spacing of 2.93 ft.

Failure was considered to have occurred at a meridional tendon strain of 0.03. At this strain level some strain hardening could be expected in both the liner and the reinforcing. However, in evaluating the meridional pressure capacity, it was assumed that the liner and the reinforcing were at their respective yield stresses (i.e., strain hardening was neglected). This

greatly simplified the calculation while introducing a slight conservative bias. The conservatism introduced is small since the liner and the reinforcing provide less than 20% of the total meridional resistance and the contribution of strain hardening constitutes a small fraction of that percentage.

Similar to the method used to estimate the liner hoop stress, the meridional stress in the liner at the meridional tendon failure was estimated from the von Mises stress. The same relationship between the liner membrane stresses was assumed (i.e., $\sigma_z = \frac{1}{2}\sigma_\theta$ and $\sigma_r \approx 0$).

With the conservative assumption that the liner is at yield at failure, the von Mises stress, σ_e, is equal to the median liner yield stress at the liner temperature. Using Equation (3-1), the liner meridional stress was estimated as

$$\sigma_z = 0.577\,\hat{\sigma}_Y$$

where $\hat{\sigma}_Y$ is the median liner yield stress.

The median pressure capacities for meridional membrane failure for the three temperature cases are shown in Tables 3-1, 3-2, and 3-3. The median capacities are substantially greater than the hoop capacities. As with the hoop capacity evaluation, logarithmic standard deviation of 0.10 was used to account for the modeling uncertainty due to tendon failure criterion and the temperature and internal force distributions. The material strength variability was estimated by weighting the individual material variabilities by the relative contributions to the total meridional resistance. The modeling and material strength uncertainties are shown with the median capacities and the associated HCLPF values in Tables 3-1, 3-2, and 3-3.

3.1.3 Dome Membrane Failure

The torispherical dome has a reduced wall thickness of three feet. Based on the results reported in Reference 5, the dome capacity is controlled by the meridional capacity of the dome at the junction of the two spherical segments of the dome. Based on information in Reference 1, the dome reinforcing was assumed to have a reinforcement ratio of 0.15% in

the meridional direction at the inside face of the wall. The meridional dome reinforcing at the outside face of the wall was provided by #9 bars at 15" plus #11 bars at 12". As with the membrane capacity evaluation for the cylinder, tendon strain level of 3% was regarded to constitute failure of the dome.

As with the evaluation of the meridional capacity of the cylinder, at the tendon failure strain limit, the liner and the reinforcing were assumed to be at their respective yield stress and strain hardening effects were neglected. Again, this simplified the calculation while introducing a slight conservative bias. To estimate the membrane stress in the liner, the von Mises stress was used. For an ideal spherical shell subjected to internal pressure, the relationship between the principal stresses is given by $\sigma_\phi = \sigma_\theta$ and $\sigma_r = 0$. Substituting this into Equation (3-1) gives the following relation between the liner membrane stress and the von Mises stress

$$\sigma_\phi = \hat{\sigma}_y$$

in which the von Mises stress is equal to the median yield stress at the liner temperature, since strain hardening effects were neglected.

The median pressure capacities, variabilities, and HCLPF values are shown in Tables 3-1 through 3-3. Note that the dome capacities fall between the hoop capacity and the meridional capacities of the cylinder. The modeling and material strength uncertainties were evaluated by the same methods as for the cylinder membrane capacities. The modeling uncertainty included the uncertainty associated with the tendon failure criterion as well as the uncertainty associated with the temperature and internal force distributions. The material strength uncertainty was estimated by weighting the β values for the individual materials by their relative contributions to the overall membrane capacity.

3.2 Flexural and Shear Failure of the Wall-Basemat Junction

Both flexural as well as shear failure of the wall-basemat junction were evaluated. The flexural capacity was investigated by developing a failure envelope for combined merid-

ional membrane tension and meridional shell moment as a flexure-tension interaction diagram. The radial shear capacity was estimated using ultimate strength principles (Reference 10) in which the shear is resisted by the concrete and reinforcing steel.

The flexure-tension interaction was described by plotting the meridional moment versus the meridional membrane force. The failure envelope for the wall-basemat junction was represented by a straight line joining the two points (M_u, 0) and (0, N_u) on the interaction diagram; where M_u and N_u are the pure bending and pure membrane ultimate capacities at the junction. In calculating the pure membrane ultimate load capacity, N_u, the liner and the bonded reinforcing were taken to be at their yield stress. The tendon force was taken at 3% strain. In calculating the moment capacity, the ACI ultimate flexural strength principles were used. Due to the anchorage of the liner and the capability for strain compatibility, the liner was included along with the meridional bonded reinforcing in providing the flexural tensile force. However, due to their placement in the wall cross section, the meridional tendons were not considered to contribute to the flexural capacity. As the internal pressure increases from an initial state corresponding to the Dead Load (D.L.) + Prestress loading, the moment and tension at the junction were assumed to increase proportionally until reaching the failure envelope. The slope of this loading line, i.e., the change in meridional moment relative to the change in membrane tension due to the pressure loading, was estimated from the junction moment and meridional tension values reported in Reference 1 due to i) D.L. + Prestress and ii) D.L. + Prestress + 82.5 psi.

After the meridional moment and membrane tension at the failure condition are calculated, the median pressure capacity is estimated as the increase in pressure required to raise the moment and membrane force from their initial values under D.L. + Prestress loading to the values at failure.

It was found that the failure condition was predominantly a flexure failure. As a result, the uncertainties calculated for M_u were used to estimate the uncertainties associated with the median pressure capacities. For the material strength uncertainty, β_S, the uncertainty values corresponding to the yield stress of the bonded reinforcing were used for both M_u and P. For the modeling uncertainty, a β value of 0.11 was evaluated for the uncertainty in the

flexural capacity equation. Additional modeling uncertainty values were estimated to account for the temperature and force distribution effects, resulting in a total modeling uncertainty of 0.16 for all three temperature cases.

The radial shear capacity at the containment wall-basemat junction is provided by the concrete and the #7 wall stirrups. In addition, some radial shear force is also resisted by the horizontal component of the inner layers of the meridional reinforcing at the knuckle region at the base of the wall (which are oriented at about 15° from the vertical). The radial shear capacity was taken as the sum of the contributions of the concrete and reinforcing steel. Since the effects of the pressure loading can result in net meridional membrane tension at the base of the wall, it was necessary to account for the reduction in the shear capacity of the concrete due to the presence of the tension acting on the cross section. This effect was included by using the provisions in Reference 10 which address the shear capacity of concrete with axial tension. As a result, the radial shear capacity was dependent on the meridional membrane force and, hence, the internal pressure. The radial shear capacity could then be expressed as a function of the yield stress of the reinforcing steel, the square root of the compressive strength of the concrete, and the internal pressure. Using the results for the radial shear at the base of the wall as reported in Reference 1, an expression was developed for the radial shear demand force as a function of pressure. The median failure capacity was obtained by equating the radial shear demand force and the shear capacity, then solving for the pressure.

The variabilities associated with the median pressure capacity at which shear failure at the junction is predicted are evaluated as follows. Since the total shear capacity was taken as the sum of the shear capacities of the steel and the concrete, the material strength uncertainty for the pressure capacity has contributions from the variability in the yield stress of the reinforcing and from the variability associated with $\sqrt{f'_c}$ (since the concrete shear strength is a function of $\sqrt{f'_c}$). This lead to β_s values of 0.12, 0.12, and 0.14 for the three temperature cases, respectively. The modeling uncertainty of 0.19 for the three temperature cases includes contributions from the variability associated with the shear capacity equation and the internal force distribution. The median pressure capacities corresponding to the junction shear failure, associated variabilities, together with the HCLPF values are listed in Tables 3-1, 3-2, and 3-3 for the three temperature cases. For all three temperature cases, the pressure capacity of the shear failure mode is higher than that of the flexural failure mode. Therefore, the flexural failure mode is the controlling failure mode for the wall-basemat junction.

3.3 Failure of the Basemat

The pressure capacity of the concrete basemat slab was determined for both flexural and shear failures. For both failure modes, median pressure capacities and the associated uncertainty values were determined for the three temperature cases. The temperature inside the containment for the three temperature cases were the same as those used for the cylinder wall analysis. However, the temperature at the bottom of the 12.5 feet basemat was taken as 50° F for all three temperature cases. Again the temperature was assumed to vary linearly through the thickness of the basemat.

Since the mat is 12.5 feet thick, the bottom reinforcing was considered to be at about room temperature for all the three temperature cases. This, plus the fact that the same concrete compressive strength was used for all temperatures above room temperature (see Section 2.2.4), results in the basemat median ultimate moment capacity for radial bending to be the same for all three temperature cases. Hence, the basemat flexural pressure capacities, associated variabilities, and HCLPF values for all three temperature cases are identical.

The basemat median ultimate moment capacity at the center of the mat where the moment is maximum was estimated to be 5890 k-ft/ft. The bending moment at the center of the basemat was evaluated at various internal pressure values. An iterative procedure was used to estimate the bending moment demand at the center of the basemat at various internal pressures. The basemat was assumed to rest on an elastic foundation with a subgrade modulus of 411 kips per cubic inch (Reference 9). The loading and deflections due to dead load, prestress, pressure as well as soil pressure were superimposed. An iterative approach was required because the soil reaction profile (assumed to be parabolic) was dependent on the deflected shape of the mat. The iteration was based on assuming deflection at the center of the basemat which determined the magnitude of the soil reaction profile and the radius where uplift is predicted. The maximum radius where contact is maintained between the mat and the soil was estimated by equating the total soil reaction force with the total containment dead load. It was found that at an internal pressure of 142 psi, the moment at the center of the basemat is 5776 k-ft/ft. Hence, 142 psi was used as the median pressure capacity of the basemat in flexural failure mode.

Since the effect of the variation of the concrete compressive strength on the flexural capacity is small, the variability due to the material strength, β_S, was taken as the β_S value of the reinforcing at room temperature ($\beta_S = 0.11$). The modeling uncertainty has contributions from the estimated variability of the predicted moment capacity of the basemat and the internal force distribution. An overall modeling uncertainty, β_M, of 0.23 was estimated. Tables 3-1, 3-2, and 3-3 show the median pressure capacities for the flexural failure mode of the basemat, the corresponding β values, and the HCLPF values for the three temperature cases.

For shear failure, the critical section of the basemat is located at about 12 feet from the junction with the containment wall. The shear capacity is provided by the concrete and the #11 bar shear reinforcing which are inclined at 45° with respect to the radial reinforcing. A relationship between the internal pressure and the basemat shear at the critical section was developed. Using this relationship, the median pressure capacity (i.e., the pressure at which the shear demand equals the ultimate shear capacity of the basemat) was estimated. The material strength and modeling uncertainties associated with the shear failure of the basemat were estimated in a similar manner to that of the shear failure of the wall-basemat junction. For all three temperature cases, the median pressures for shear failure were higher than those for flexural failure. Therefore, the flexural failure mode was judged to be the critical failure mode for the basemat. The median pressure capacities, the corresponding β values, and the HCLPF values associated with the shear failure of the basemat for the three temperature cases are shown in Tables 3-1, 3-2, and 3-3 for comparison.

Table 3-1 Pressure Capacities for the Reactor Building Structural Failure Modes - Temperature Case 1

Interior Temperature = 300° F.

	Failure Mode	$\hat{P}$ (psig)	β_M	β_S	β	HCLPF (psig)
1	Wall-Basemat Junction Flexure	140	0.16	0.13	0.21	99
3	Basemat Flexure	142	0.23	0.11	0.25	94
2	Wall-Basemat Junction Shear	147	0.19	0.12	0.22	102
4	Basemat Shear	152	0.19	0.07	0.20	109
5	Cylinder Hoop Membrane	172	0.10	0.06	0.12	141
6	Dome Meridional Membrane	199	0.10	0.06	0.12	163
7	Cylinder Meridional Membrane	216	0.10	0.06	0.12	177

Table 3-2 Pressure Capacities for the Reactor Building Structural Failure Modes - Temperature Case 2

Interior Temperature = 500° F.

Failure Mode	$\hat{P}$ (psig)	β_M	β_S	β	HCLPF (psig)
Wall-Basemat Junction Flexure	134	0.16	0.14	0.21	95
Basemat Flexure	142	0.23	0.12	0.25	94
Wall-Basemat Junction Shear	146	0.19	0.12	0.22	102
Basemat Shear	151	0.19	0.08	0.21	107
Cylinder Hoop Membrane	167	0.10	0.06	0.12	137
Dome Meridional Membrane	194	0.10	0.06	0.12	159
Cylinder Meridional Membrane	211	0.10	0.06	0.12	173

Table 3-3 Pressure Capacities for the Reactor Building Structural Failure Modes - Temperature Case 3

Interior Temperature = 800° F

Failure Mode	$\hat{P}$ (psig)	β_M	β_S	β	HCLPF (psig)
Wall-Basemat Junction Flexure	122	0.16	0.16	0.23	83
Wall-Basemat Junction Shear	139	0.19	0.14	0.24	94
Basemat Flexure	142	0.23	0.11	0.25	94
Basemat Shear	150	0.19	0.09	0.21	106
Cylinder Hoop Membrane	157	0.10	0.06	0.12	129
Dome Meridional Membrane	166	0.10	0.08	0.13	134
Cylinder Meridional Membrane	199	0.10	0.06	0.12	163

4. REACTOR CAVITY ACCESS TUNNEL DOORS

Two doors which provide reactor cavity access were evaluated for expected pressure capacity. Doors DF-2 and DF-3 are located at top of concrete elevations 95'-0" and 94'-0", respectively. The doors are located in series (i.e., the failure of both doors is required prior to leakage).

Both doors are similar in size and construction. The doors are constructed of 1.25" A36 steel plate and are pressure loaded against heavy angle section frames. One quarter inch thick EPDM E603 gaskets provide the seals between the doors and frame. Door hinges are slotted to provide allowance for additional gasket compression resulting from cavity pressure. The outside dimensions of the doors are 2'-10" by 2'-4" for DF-2 and 2'-4.5" by 2'-2.5" for DF-3.

Pressure capacities for both doors are significantly greater than those determined for the various structural failure modes discussed in the previous section. Median pressure capacities for both doors at several temperatures are shown in Table 4-1. At high temperatures, some deterioration of the EPDM gasket will occur. However, the gasket is expected to continue to function provided it is continuously loaded by the internal pressure. Concrete deformations in the regions around the doors are not expected to result in uncovering the gasket. Thus, the door pressure capacity is expected to be controlled by deformation of the doors themselves.

Table 4-1 DF-2 and DF-3 Door Pressure Capacities

Temperature (°F)	DF-2			DF-3		
	Median Pressure (psig)	β	HCLPF (psig)	Median Pressure (psig)	β	HCLPF (psig)
70	296	0.14	235	361	0.14	287
300	262	0.14	208	320	0.14	254
500	239	0.15	187	292	0.15	228
800	197	0.15	154	240	0.15	187

5. CORRELATION OF FAILURE MODES

For the purpose of estimating the correlation between structural failure modes, the uncertainty was subdivided into two independent components:

1. Uncertainty in modeling
2. Uncertainty in strength

These uncertainties may be represented by two independent random factors with logarithmic standard deviations, β_M and β_S, respectively. The combined coefficient of variation is then given by:

$$\beta = \sqrt{\beta_M^2 + \beta_S^2}$$

The advantage of splitting the uncertainty into these two components is that for a given pair of failure modes the uncertainty factor for one of the components may be correlated for both modes, while the other is independent. However, for Crystal River, it was found in all cases that if the uncertainty in modeling for a given failure mode is expected to be correlated with the uncertainty in modeling for a different mode, the uncertainty in the strengths of the same two modes were also expected to be correlated. For example, the strengths of the various shell membrane capacities are then governed largely by the tendon capacities for which common strength values were used and hence a high degree of correlation in the uncertainty of the strength parameters is expected. Similarly, for these same failure modes, similar modeling assumptions were used including failure strain criteria, similar load redistribution due to tendon friction, etc. Likewise, while the strength and modeling assumptions used to evaluate the DF-2 and DF-3 doors are correlated, these assumptions are completely different from those used for the membrane capacities. Similar considerations for every pair of failure modes lead to the correlation matrix shown in Table 5-2. In this table, the uncertainty factors are assumed to be either perfectly correlated, in which case, a cross is placed in the appropriate box, or perfectly uncorrelated. Perfect correlation is assumed whenever the degree of correlation is estimated to be more than one-half.

Table 5-1

Failure Mode

Failure Mode Number	Failure Mode
1	Wall-Basemat Junction Flexure
2	Wall-Basemat Junction Shear
3	Basemat Flexure
4	Basemat Shear
5	Cylinder Hoop Membrane
6	Dome Meridional Membrane
7	Cylinder Meridional Membrane
8	Door DF-2
9	Door DF-3

Table 5-2

Correlation between Failure Modes
(Strength and Modeling Uncertainty)

	1	2	3	4	5	6	7	8	9
1	x	x							
2		x							
3			x	x					
4				x					
5					x	x	x		
6		Symmetric				x	x		
7							x		
8								x	x
9									x

REFERENCES

1. Final Safety Analysis Report (FSAR) for the Crystal River Unit 3 Nuclear Power Plant.

2. Holmes, M., Anchor, R.D., Cook, G.M.E., and Crook, R.N., "The Effects of Elevated Temperatures on the Strength Properties of Reinforcing and Prestressing Steels," The Structural Engineer, Volume 60B, No. 1, March, 1982.

3. "ASME Boiler and Pressure Vessel Code, Rules for Construction of Nuclear Power Plant Components," Section III, Appendices, 1989.

4. "Test Results on the Crystal River Unit 3 Liner Material," Chicago Bridge & Iron Company, July 28, 1969.

5. "Crystal River Unit 3, Reactor Building Dome Delamination Report," Gilbert Associates, Inc., Report No. 1913, December 1976.

6. Park, R., and Paulay, T., Reinforced Concrete Structures, John Wiley, 1975.

7. Abrams, M. S., "Compression Strength of Concrete at Temperatures to 1600 °F," Temperature and Concrete, American Concrete Institute, SP-25, 1971.

8. "Steel Reinforcement - Physical Properties and U.S. Availability," ACI Materials Journal, January-February 1989.

9. "Crystal River Unit No. 3 Reactor Building Shell Calc's, Book I 1:01.1 to 1:01.3," December 5, 1973.

10. "Building Code Requirements for Reinforced Concrete (ACI 318-89)," American Concrete Institute, November 1989.

11. Mirza, S.A. and MacGregor, J.G., "Variability of Mechanical Properties of Reinforcing Bars," Journal of Structural Division, ASCE, Vol. 105, No. ST5, May 1979.

12. "Median Material Properties and Variabilities," ABB Impell Corporation, Calculation CA-6570-001-001, Rev. 0.

13. "Containment Structure Membrane Capacities," ABB Impell Corporation, Calculation CA-6570-001-002, Rev. 0.

14. "Basemat and Wall - Basemat Junction Capacities," ABB Impell Corporation, Calculation CA-6570-001-003, Rev. 0.

15. "Reactor Cavity Access Tunnel Doors DF-2 & DF-3," ABB Impell Corporation, Calculation CA-6570-001-004, Rev. 0.

APPENDIX A

CHARACTERISTICS OF THE LOGNORMAL DISTRIBUTION

Some of the characteristics of the lognormal distribution which are useful to keep in mind when generating estimates of $\hat{P}$, β_M, and β_S are summarized in References A-1 and A-2. A random variable X is said to be lognormally distributed if its natural logarithm Y, given by:

$$Y = \ln(X) \qquad (A-1)$$

is normally distributed with the mean of Y equal to $\ln(\hat{X})$, where $\hat{X}$ is the median of X, and with the standard deviation of Y equal to β, which will be defined herein as the logarithmic standard deviation of X. The coefficient of variation of X, COV, is given by the relationship:

$$COV = \sqrt{\exp(\beta^2) - 1} \qquad (A-2)$$

For β values less than about 0.5, this equation becomes approximately

$$COV \approx \beta \qquad (A-3)$$

and COV and β are used interchangeably.

For a lognormal distribution, the median value is used as the characteristic parameter of central tendency (50 percent of the values are above the median value and 50 percent are below the median value). The logarithmic standard deviation, β, or the coefficient of variation, COV, is used as a measure of the dispersion of the distribution.

The relationship between the median value, $\hat{X}$, logarithmic standard deviation, β, and any value x of the random variable can be expressed as

$$x = \hat{X} \cdot e^{\eta \cdot \beta} \qquad (A-4)$$

where η is the standardized Gaussian random variable (with zero mean and unit standard deviation). Therefore, the frequency that X is less than any value x' equals the frequency that η is less than η' where

$$\eta' = \frac{\ln(x'/\hat{X})}{\beta} \qquad (A-5)$$

Because η is a standardized Gaussian random variable, one can simply enter standardized Gaussian tables to find the frequency that η is less than η' which equals the probability that X is less than x'. Using the cumulative distribution tables for the standardized Gaussian random variable, it van be shown that the $\hat{X} \cdot e^{\beta}$ value of a lognormal distribution corresponds to the 84th percentile value (i.e., 84 percent of the data fall below the $+\beta$ value). The $\hat{X} \cdot e^{-\beta}$ corresponds to the value for which 16 percent of the data fall below.

One implication of the usage of the lognormal distribution is that if A, B, and C are independent lognormally distributed random variables, and if

$$D = \frac{A^r \cdot B^s}{C^t} q \qquad (A-6)$$

where q, r, s, and t are given constants, then D is also a lognormally distributed random variable. Further, the median value of D, denoted by $\hat{D}$, and the logarithmic variance, β_D^2, which is the square of the logarithmic standard deviation, β_D, of D, are given by

$$\hat{D} = \frac{\hat{A}^r \cdot \hat{B}^s}{\hat{C}^t} q \qquad (A-7)$$

and

$$\beta_D^2 = r^2\beta_A^2 + s^2\beta_B^2 + t^2\beta_C^2 \qquad (A-8)$$

where $\hat{A}$, $\hat{B}$, and $\hat{C}$ are the median values, and β_A, β_B, and β_C are the logarithmic standard deviations of A, B, and C, respectively.

References

A-1 Benjamin, J. R. and Cornell, C. A., Probability, Statistics and Decision for Civil Engineers, McGraw-Hill, Inc., 1970.

A-2 Kennedy, R. P. and Chelapati, C. V., "Conditional Probability of A Local Flexural Wall Failure of A Reactor Building As A Result of Aircraft Impact," Holmes and Narver, Inc., prepared for General Electric Company, San Jose, California, June, 1970.

CR-3 IPE
Level 2 Appendices

APPENDIX A

CR3 K3BA-S1 LBLOCA all debris in Cell 1

Table A.1-1: Fission Products Distribution

SIMPLE FISSION PRODUCT MASSES (KG) IN CELL 1 AT TIME = 40000.000 (S)

HOST	TYPE	NAME	1 CSI	2 CSOH	3 TE	4 SR	5 BA	6 LA
2	AEROSOL	UO2	2.80260E-45	2.80260E-45	3.86011E-04	1.56831E-07	2.92680E-06	7.84650E-07
0	TOTAL	WALL	4.17648E-05	1.74064E-04	4.42677E-03	2.31355E-02	2.07518E-02	1.30216E-02
0	LOW-CELL + DUMMY		1.15317E-01	6.91905E-01	2.64370E+00	1.31118E+01	1.20852E+01	5.96872E+00
	TOTAL		1.15359E-01	6.92079E-01	2.64851E+00	1.31350E+01	1.21060E+01	5.98174E+00

HOST	TYPE	NAME	7 CE	8 RU	9 PI
2	AEROSOL	UO2	7.45403E-07	2.35775E-11	9.89590E-03
0	TOTAL	WALL	1.43409E-02	1.41835E-07	5.27013E-01
0	LOW-CELL + DUMMY		7.16724E+00	6.93879E-05	4.57085E+02
	TOTAL		7.18158E+00	6.95298E-05	4.57622E+02

HOST MATERIAL INFORMATION IN CELL 1 AT TIME = 40000.000 (S)

HOST	TYPE	NAME	POWER (WATTS)	TEMPERATURE (K)
2	AEROSOL	UO2	0.00000E+00	3.66800E+02
0	TOTAL	WALL	0.00000E+00	0.00000E+00
0	LOW-CELL + DUMMY		0.00000E+00	0.00000E+00
	TOTAL		0.00000E+00	

SIMPLE FISSION PRODUCT MASSES (KG) IN CELL 2 AT TIME = 40000.000 (S)

HOST	TYPE	NAME	1 CSI	2 CSOH	3 TE	4 SR	5 BA	6 LA
2	AEROSOL	UO2	1.40130E-44	1.40130E-44	2.38035E-03	9.71481E-07	1.81821E-05	4.83019E-06
0	TOTAL	WALL	5.50807E-04	3.17038E-03	1.06238E-02	3.21661E-02	2.54512E-02	3.52930E-02
0	TOTAL	FLOOR	1.30601E-03	7.72442E-03	5.41163E-02	3.71002E-01	3.05151E-01	1.65316E-01
		TOTAL	1.85682E-03	1.08948E-02	6.71205E-02	4.03169E-01	3.30620E-01	2.00613E-01

HOST	TYPE	NAME	7 CE	8 RU	9 PI
2	AEROSOL	UO2	4.58860E-06	1.45860E-10	6.10023E-02
0	TOTAL	WALL	3.17877E-02	3.73500E-07	6.06071E-01
0	TOTAL	FLOOR	2.49365E-01	2.26159E-06	6.55095E+00
		TOTAL	2.81157E-01	2.63523E-06	7.21803E+00

HOST MATERIAL INFORMATION IN CELL 2 AT TIME = 40000.000 (S)

HOST	TYPE	NAME	POWER (WATTS)	TEMPERATURE (K)
2	AEROSOL	UO2	0.00000E+00	3.66628E+02
0	TOTAL	WALL	0.00000E+00	0.00000E+00
0	TOTAL	FLOOR	0.00000E+00	0.00000E+00
		TOTAL	0.00000E+00	

SIMPLE FISSION PRODUCT MASSES (KG) IN CELL 4 AT TIME = 40000.000 (S)

HST	TYPE	NAME	1 CSI	2 CSOH	3 TE	4 SR	5 BA	6 LA
2	AEROSOL	UO2	0.00000E+00	0.00000E+00	1.89093E-04	7.72344E-08	1.44623E-06	3.83591E-07
0	TOTAL	WALL	1.48423E-01	8.88012E-01	1.01642E-01	2.05361E-03	7.91680E-03	3.62106E-04
0	LOW-CELL + DUMMY		1.91492E+01	1.15015E+02	8.27173E+00	1.17052E+00	2.21046E+00	3.30278E-01
	TOTAL		1.92976E+01	1.15903E+02	8.37356E+00	1.17257E+00	2.21838E+00	3.30641E-01

HOST	TYPE	NAME	7 CE	8 RU	9 PI
2	AEROSOL	UO2	3.64405E-07	1.15940E-11	4.84566E-03
0	TOTAL	WALL	4.71966E-04	4.13538E-09	8.17745E-01
0	LOW-CELL + DUMMY		4.05143E-01	3.60052E-06	1.81388E+02
	TOTAL		4.05616E-01	3.60467E-06	1.82211E+02

HOST MATERIAL INFORMATION IN CELL 4 AT TIME = 40000.000 (S)

HOST	TYPE	NAME	POWER (WATTS)	TEMPERATURE (K)
2	AEROSOL	UO2	0.00000E+00	3.33580E+02
0	TOTAL	WALL	0.00000E+00	0.00000E+00
0	LOW-CELL + DUMMY		0.00000E+00	0.00000E+00
	TOTAL		0.00000E+00	

SIMPLE FISSION PRODUCT MASSES (KG) IN CELL 5 AT TIME = 40000.000 (S)

HOST	TYPE	NAME	1 CSI	2 CSOH	3 TE	4 SR	5 BA	6 LA
2	AEROSOL	UO2	1.40130E-45	1.40130E-45	1.40302E-05	5.74504E-09	1.07750E-07	2.84347E-08
0	TOTAL	WALL	4.69204E-02	2.80631E-01	3.20581E-02	7.45573E-04	2.58473E-03	1.72542E-04
		TOTAL	4.69204E-02	2.80631E-01	3.20721E-02	7.45579E-04	2.58484E-03	1.72571E-04

HOST	TYPE	NAME	7 CE	8 RU	9 PI
2	AEROSOL	UO2	2.70123E-08	8.61982E-13	3.59463E-04
0	TOTAL	WALL	2.07058E-04	1.79444E-09	2.54044E-01
		TOTAL	2.07085E-04	1.79530E-09	2.54404E-01

HOST MATERIAL INFORMATION IN CELL 5 AT TIME = 40000.000 (S)

HOST	TYPE	NAME	POWER (WATTS)	TEMPERATURE (K)
2	AEROSOL	UO2	0.00000E+00	3.32998E+02
0	TOTAL	WALL	0.00000E+00	0.00000E+00
		TOTAL	0.00000E+00	

SIMPLE FISSION PRODUCT MASSES (KG) IN CELL 6 AT TIME = 40000.000 (S)

HST	TYPE	NAME	1 CSI	2 CSOH	3 TE	4 SR	5 BA	6 LA
2	AEROSOL	UO2	0.00000E+00	0.00000E+00	8.65718E-05	3.53685E-08	6.62381E-07	1.75603E-07
0	TOTAL	WALL	1.42311E-02	8.64111E-02	9.39763E-03	3.84184E-04	9.75044E-04	1.77192E-05
		TOTAL	1.42311E-02	8.64111E-02	9.48421E-03	3.84219E-04	9.75706E-04	1.78948E-05

HOST	TYPE	NAME	7 CE	8 RU	9 PI
2	AEROSOL	UO2	1.66819E-07	5.30898E-12	2.21844E-03
0	TOTAL	WALL	4.11746E-05	1.41502E-10	8.86628E-02
		TOTAL	4.13414E-05	1.46811E-10	9.08812E-02

HOST MATERIAL INFORMATION IN CELL 6 AT TIME = 40000.000 (S)

HOST	TYPE	NAME	POWER (WATTS)	TEMPERATURE (K)
2	AEROSOL	UO2	0.00000E+00	3.33650E+02
0	TOTAL	WALL	0.00000E+00	0.00000E+00
		TOTAL	0.00000E+00	

SIMPLE FISSION PRODUCT MASSES (KG) IN CELL 7 AT TIME = 40000.000 (S)

?ST	TYPE	NAME	1 CSI	2 CSOH	3 TE	4 SR	5 BA	6 LA
2	AEROSOL	UO2	2.66247E-44	2.66247E-44	4.82489E-04	1.97535E-07	3.70445E-06	9.77907E-07
0	TOTAL	ROOF	4.76490E-03	2.90771E-02	3.15624?-03	1.63462E-04	3.61757E-04	9.47787E-06
0	TOTAL	WALL	5430E-02	1.73334E-01	1.89603E-02	8.11361E-04	2.00551E-03	4.40818E-05
		TOTA	3 0?9E-02	2.02411E-01	2.25991E-02	9.75021E-04	2.37097E-03	5.45376E-05

HOST	TYPE	NAME	7 CE	8 RU	9 PI
2	AEROSOL	UO2	9.28992E-07	2.96390E-11	1.23618E-02
0	TOTAL	ROOF	2.05411E-05	8.27787E-11	3.03635E-02
0	TOTAL	WALL	9.89023E-05	3.77551E-10	1.74659E-01
		TOTAL	1.20372E-04	4.89969E-10	2.17385E-01

HOST MATERIAL INFORMATION IN CELL 7 AT TIME = 40000 ?.?? (S)

HOST	TYPE	NAME	POWER (WATTS)	TEMPERATURE (K)
2	AEROSOL	UO2	0.00000E+00	3.32041E+02
0	TOTAL	ROOF	0.00000E+00	0.00000E+00
0	TOTAL	WALL	0.00000E+00	0.00000E+00
		TOTAL	0.00000E+00	

SIMPLE FISSION PRODUCT MASSES (KG) IN CELL 8 AT TIME = 40000.000 (S)

HST	TYPE	NAME	1 CSI	2 CSOH	3 TE	4 SR	5 BA	6 LA
2	AEROSOL	UO2	4.20390E-45	8.40779E-45	4.82407E-04	1.98094E-07	3.72216E-06	9.76670E-07
0	TOTAL	WALL	2.95257E-03	1.75604E-02	1.90002E-03	1.75845E-03	1.98977E-03	2.99448E-04
0	LOW-CELL	+ DUMMY	2.57282E+01	1.52850E+02	1.00457E+01	3.61857E+00	4.72099E+00	9.01801E-01
		TOTAL	2.57312E+01	1.52868E+02	1.00481E+01	3.62033E+00	4.72298E+00	9.02102E-01

HOST	TYPE	NAME	7 CE	8 RU	9 PI
2	AEROSOL	UO2	9.27820E-07	2.97129E-11	1.23566E-02
0	TOTAL	WALL	4.79920E-04	3.40905E-09	6.91741E-02
0	LOW-CELL	+ DUMMY	1.32320E+00	1.20293E-05	3.39147E+02
		TOTAL	1.32368E+00	1.20327E-05	3.39229E+02

HOST MATERIAL INFORMATION IN CELL 8 AT TIME = 40000.000 (S)

HOST	TYPE	NAME	POWER (WATTS)	TEMPERATURE (K)
2	AEROSOL	UO2	0.00000E+00	3.44956E+02
0	TOTAL	WALL	0.00000E+00	0.00000E+00
0	LOW-CELL	+ DUMMY	0.00000E+00	0.00000E+00
		TOTAL	0.00000E+00	

SIMPLE FISSION PRODUCT MASSES (KG) IN CELL 9 AT TIME = 40000.000 (S)

HOST	TYPE	NAME	1 CSI	2 CSOH	3 TE	4 SR	5 BA	6 LA
2	AEROSOL	UO2	1.80138E-15	9.82980E-15	3.24917E-08	2.61741E-08	2.93760E-08	7.76884E-10
0	TOTAL	FLOOR	1.78251E-05	1.06455E-04	1.03306E-05	2.87391E-06	3.76692E-06	6.49865E-07
		TOTAL	1.78251E-05	1.06455E-04	1.03631E-05	2.90008E-06	3.79629E-06	6.50642E-07

HOST	TYPE	NAME	7 CE	8 RU	9 PI
2	AEROSOL	UO2	1.63078E-09	9.09113E-15	3.64908E-06
0	TOTAL	FLOOR	9.75544E-07	8.67538E-12	2.27186E-04
		TOTAL	9.77175E-07	8.68447E-12	2.30835E-04

HOST MATERIAL INFORMATION IN CELL 9 AT TIME = 40000.000 (S)

HOST	TYPE	NAME	POWER (WATTS)	TEMPERATURE (K)
2	AEROSOL	UO2	0.00000E+00	3.00000E+02
0	TOTAL	FLOOR	0.00000E+00	0.00000E+00
		TOTAL	0.00000E+00	

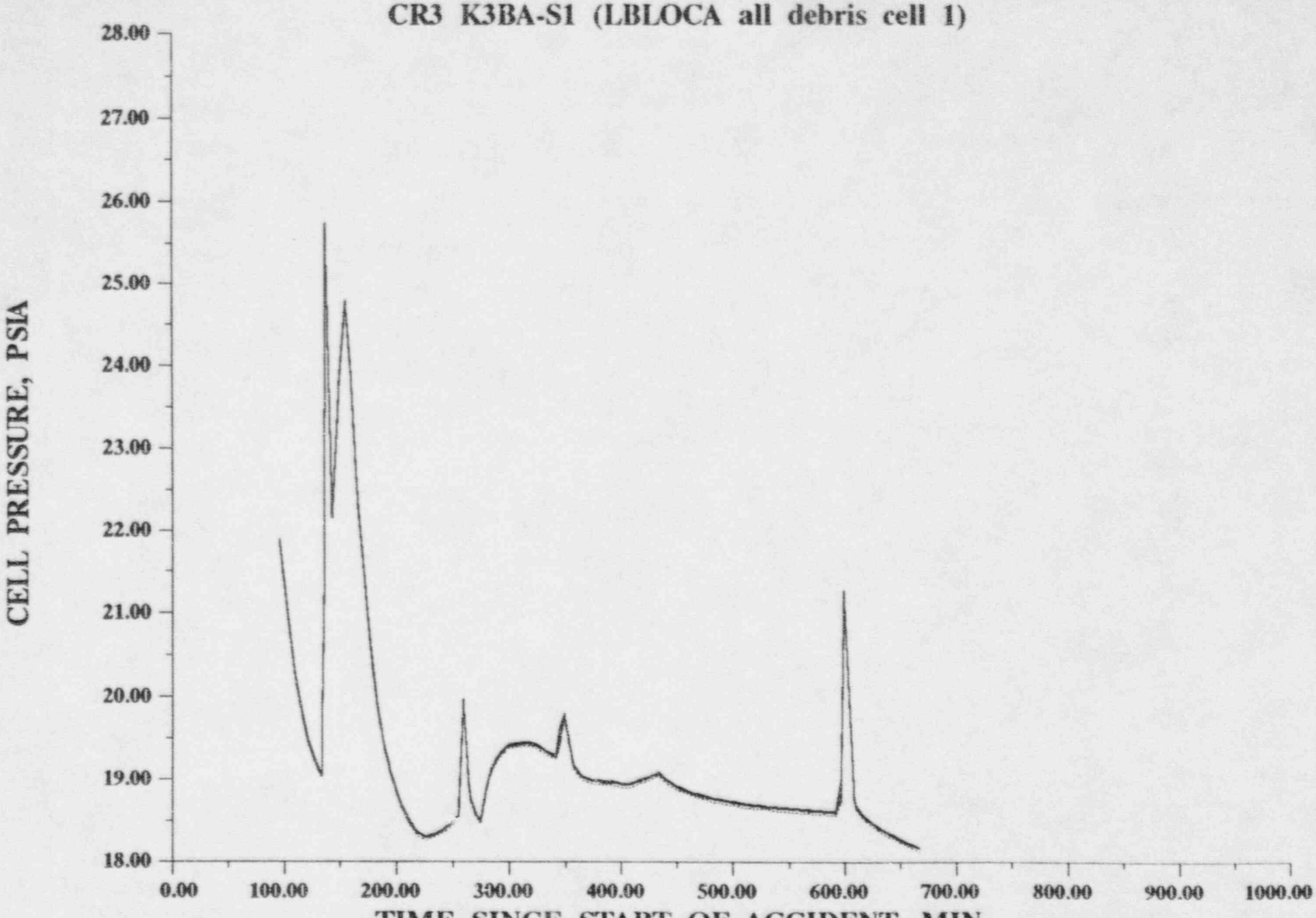

Figure A-1: CELL PRESSURE

11/25/91

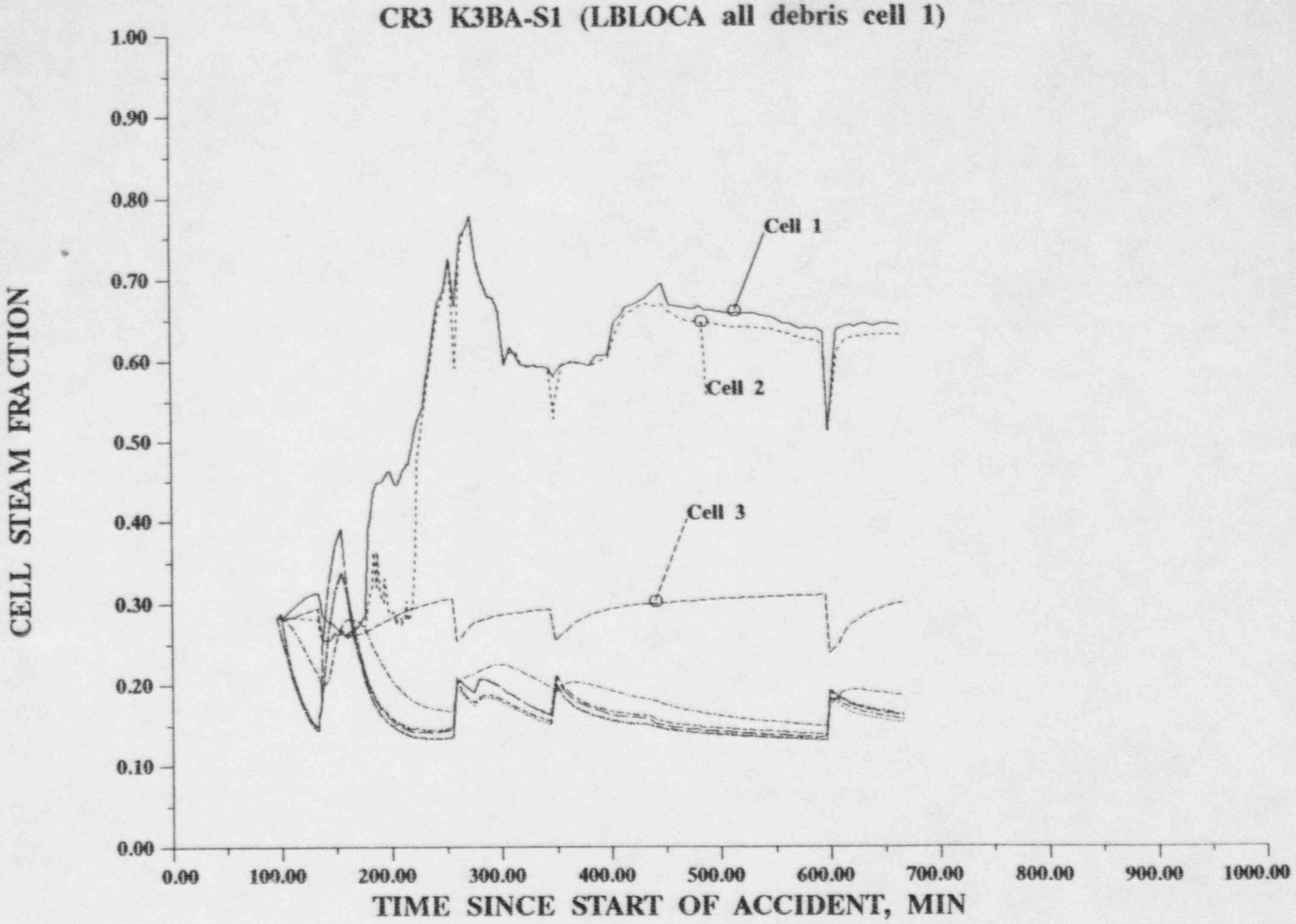

Figure A-5: CELL STEAM FRACTION

11/25/91

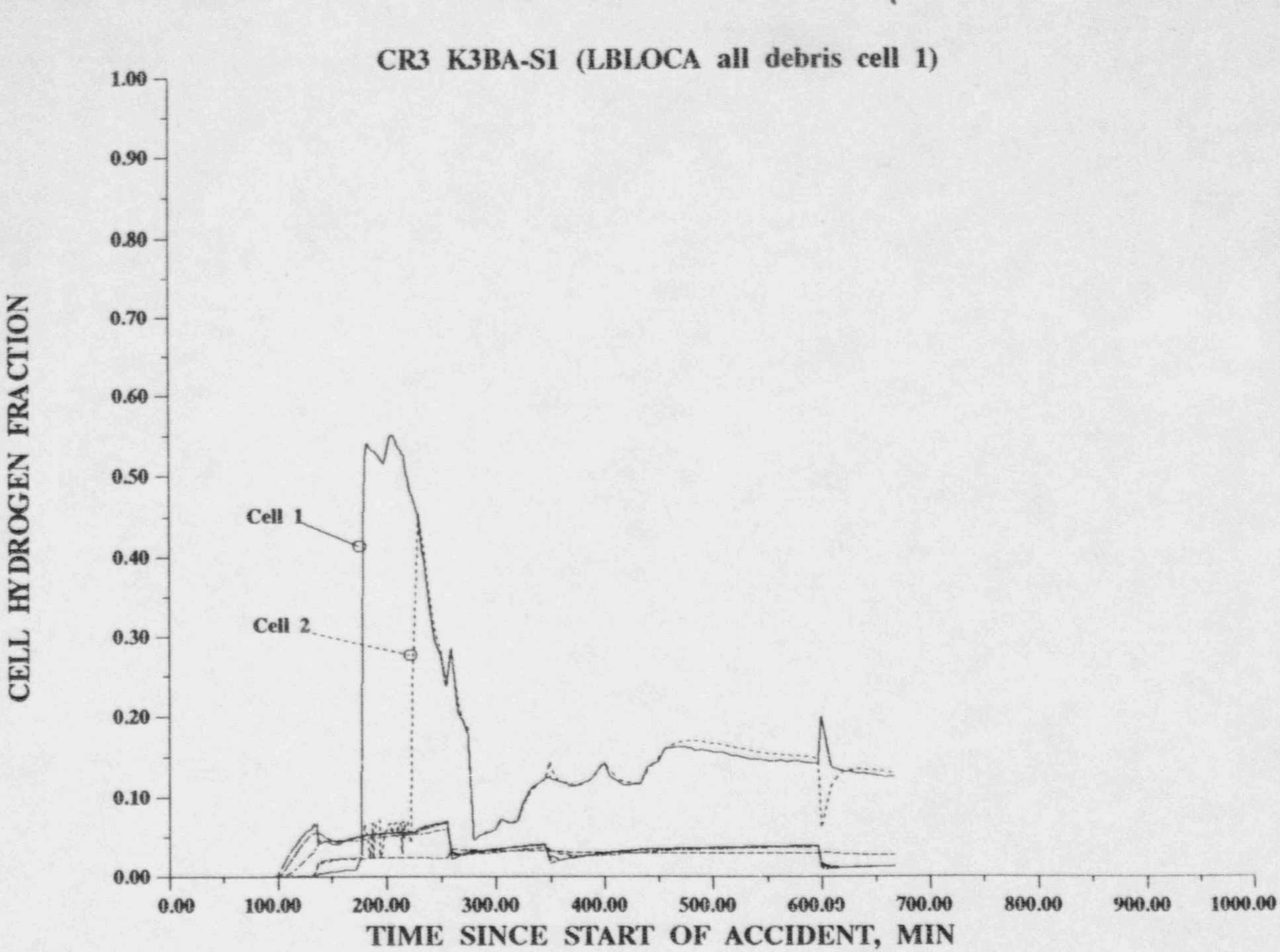

Figure A-6: CELL HYDROGEN FRACTION

11/25/91

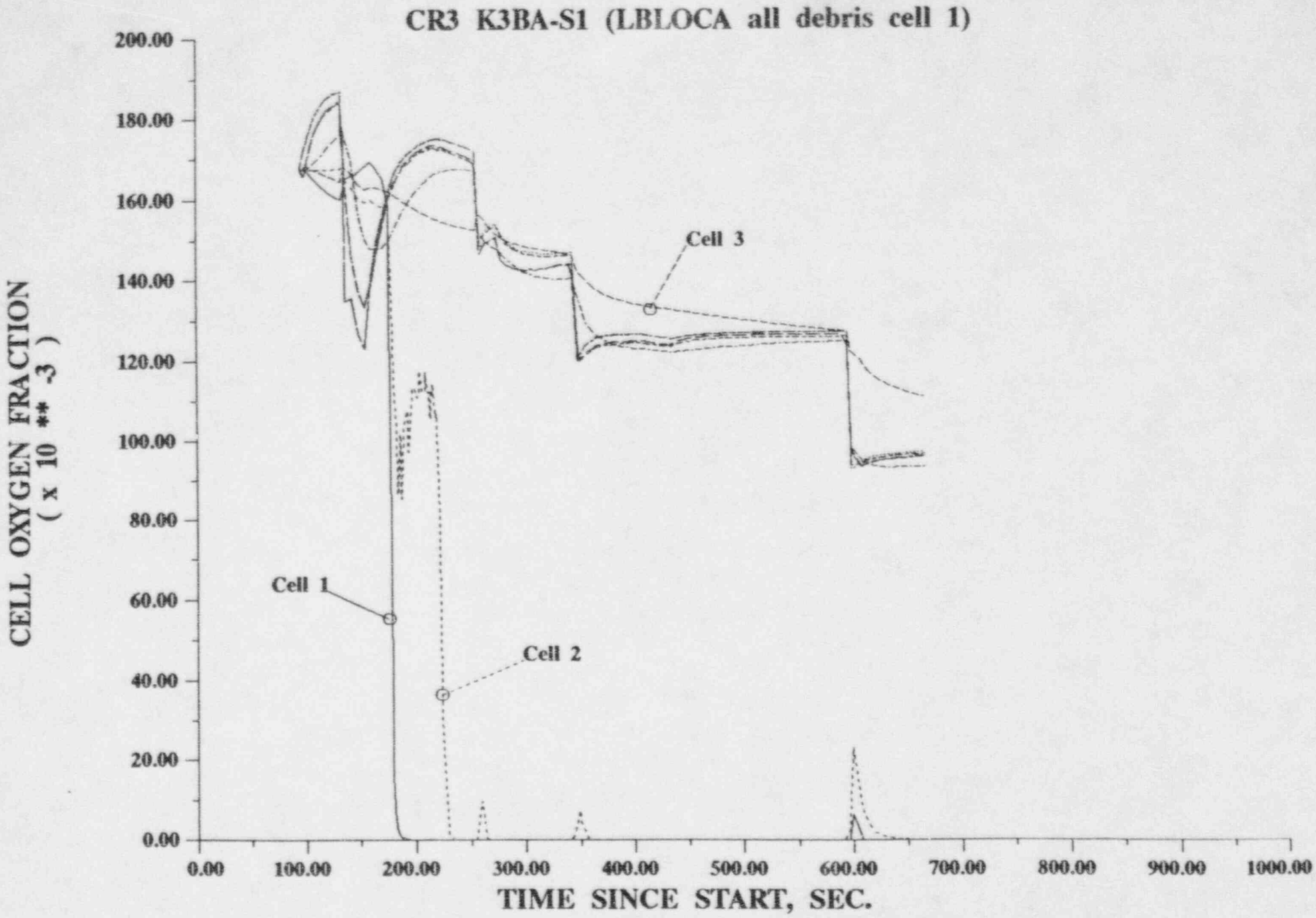

Figure A-7: CELL OXYGEN FRACTION

11/25/91

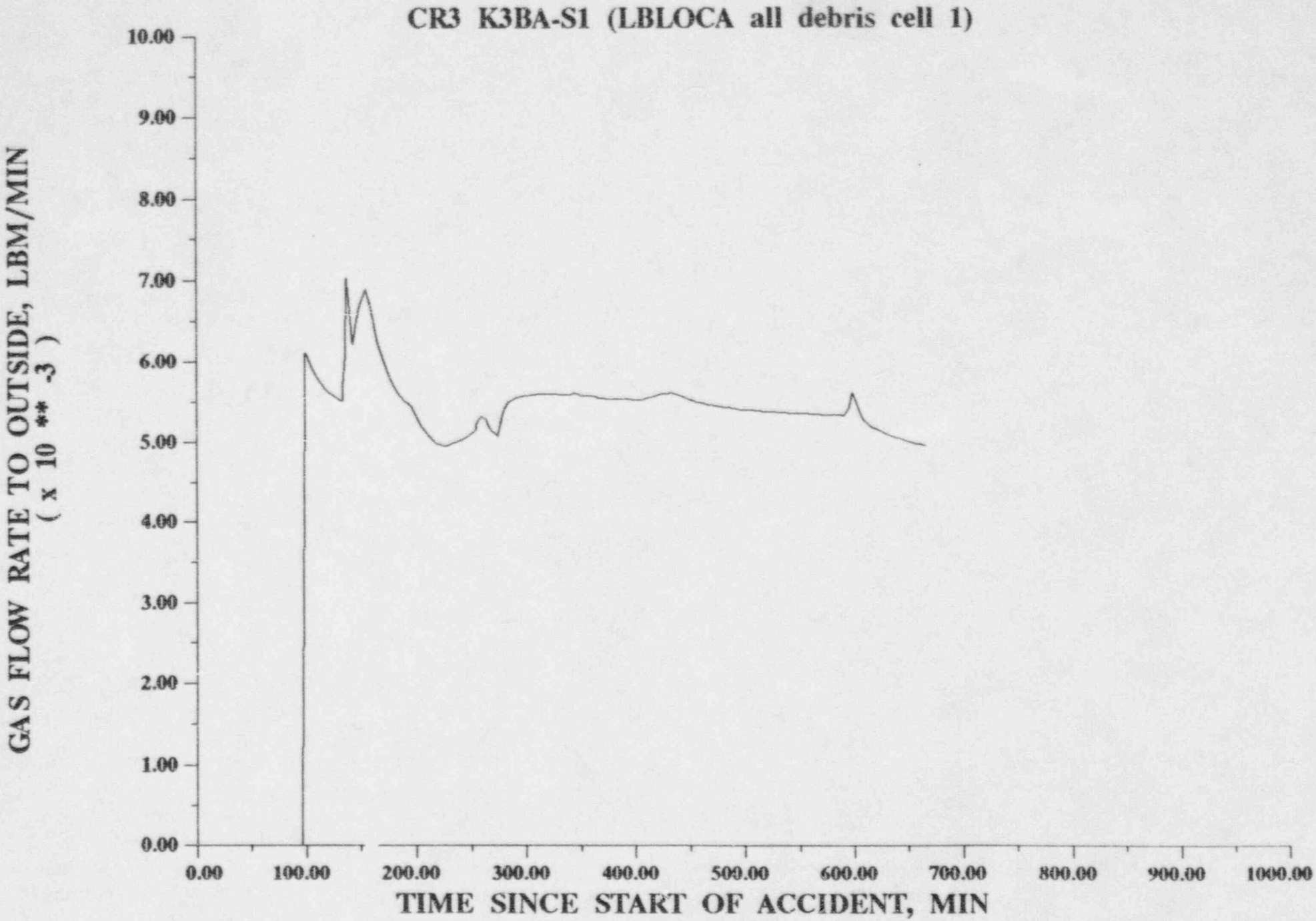

Figure A-8: GAS FLOW RATE TO OUTSIDE

11/25/91

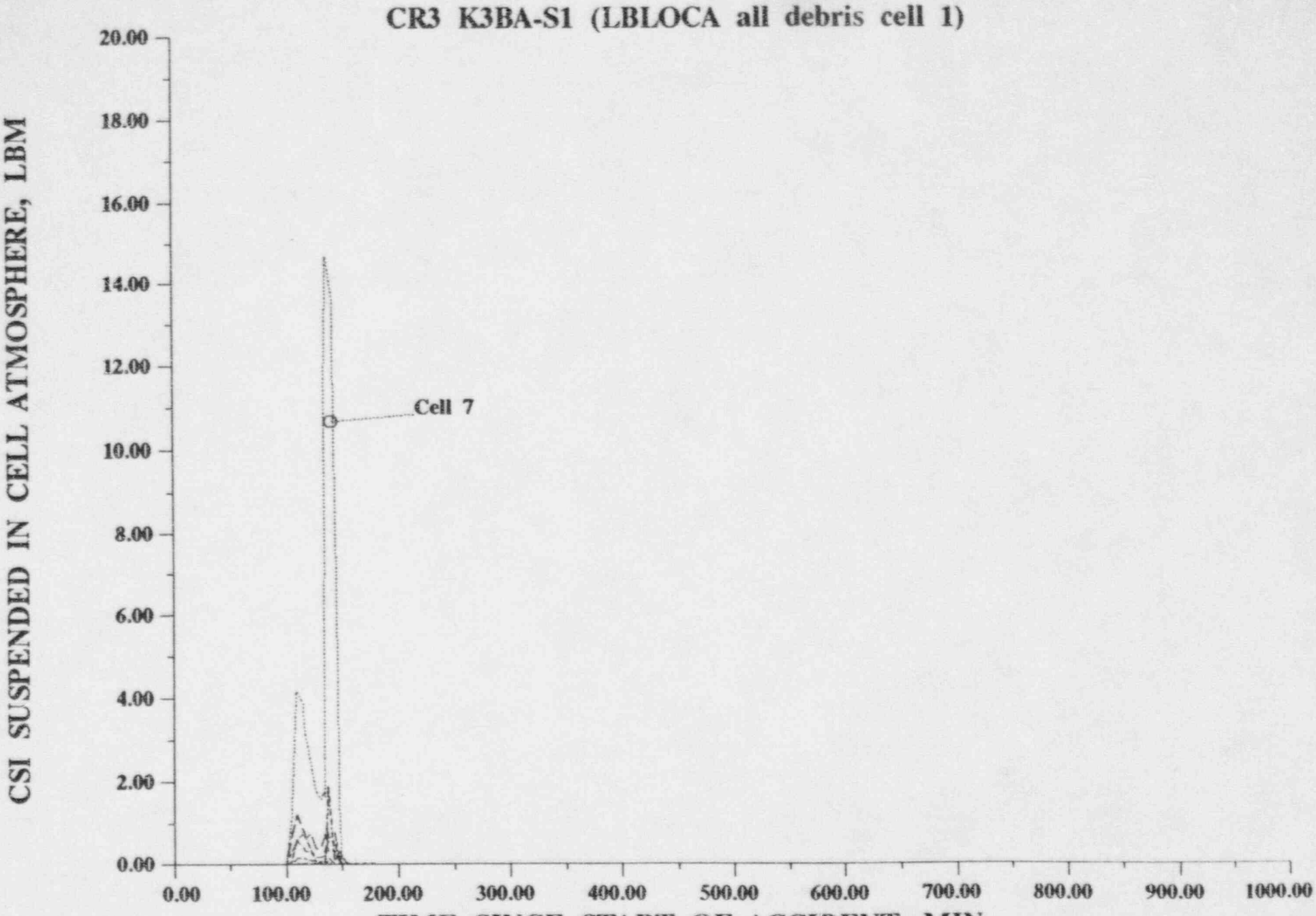

Figure A-9: CSI SUSPENDED IN CELL ATMOSPHERE

11/25/91

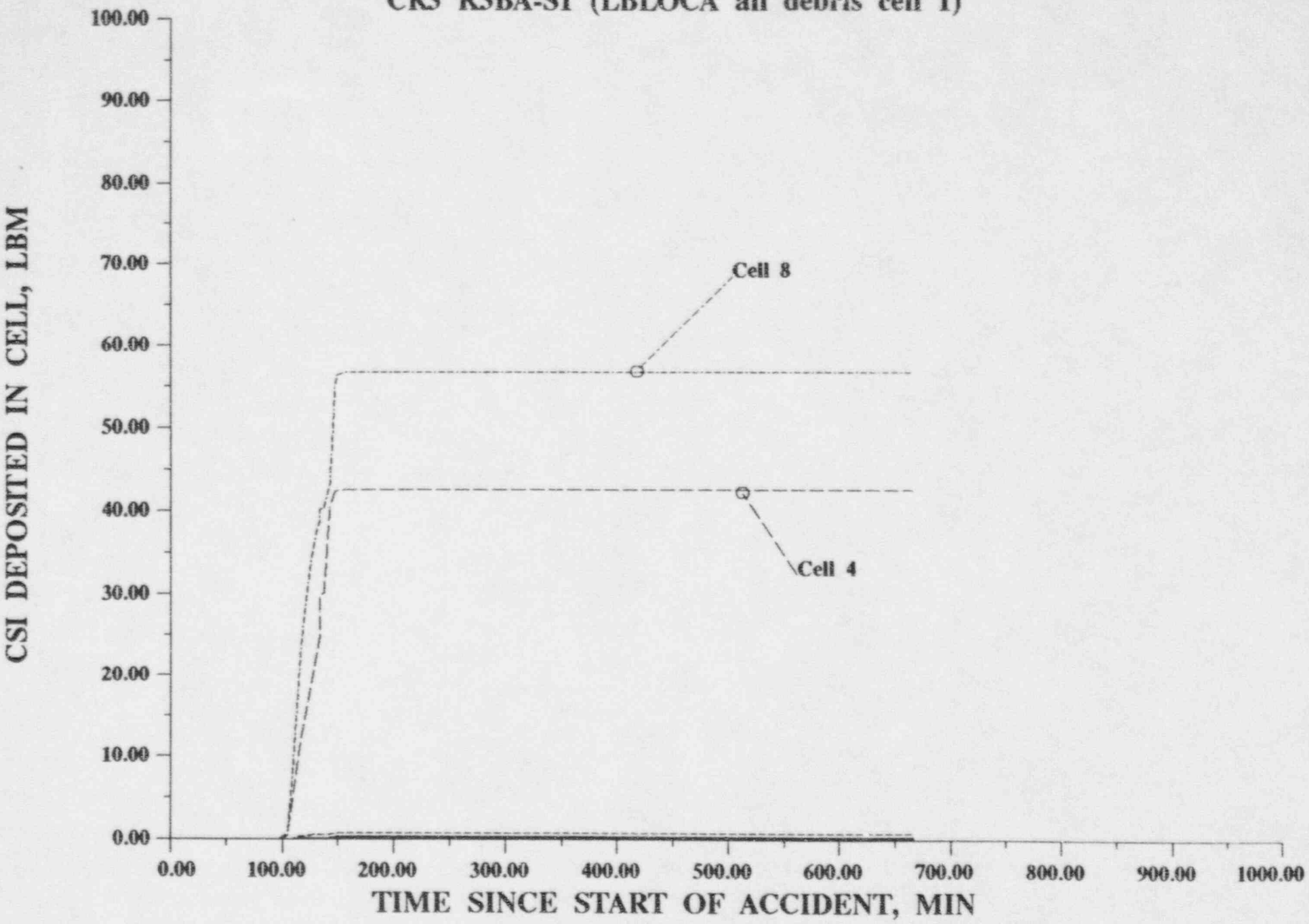

Figure A-10: CSI DEPOSITED IN CELL

11/25/91

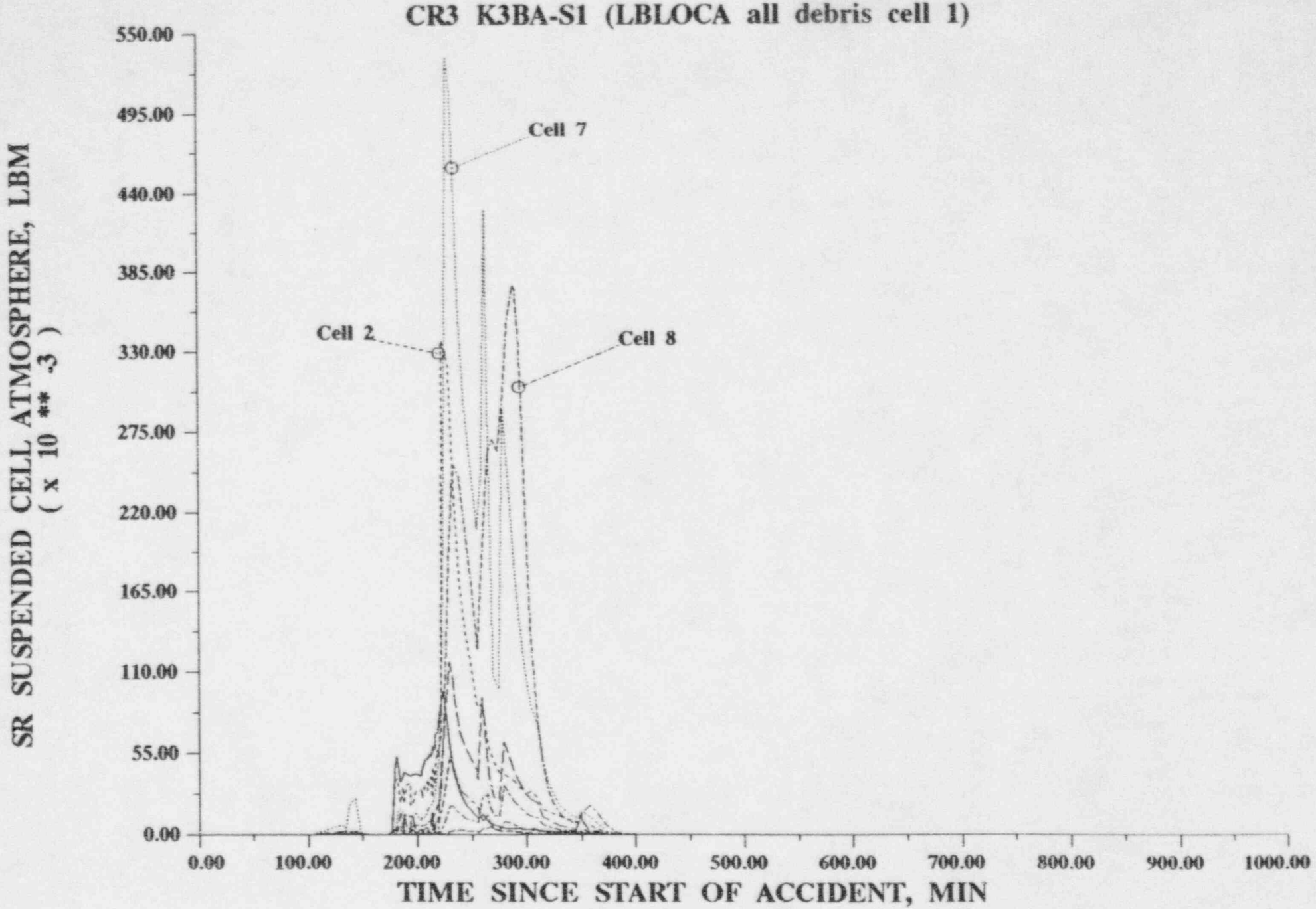

Figure A-11: SR SUSPENDED CELL ATMOSPHERE

11/25/91

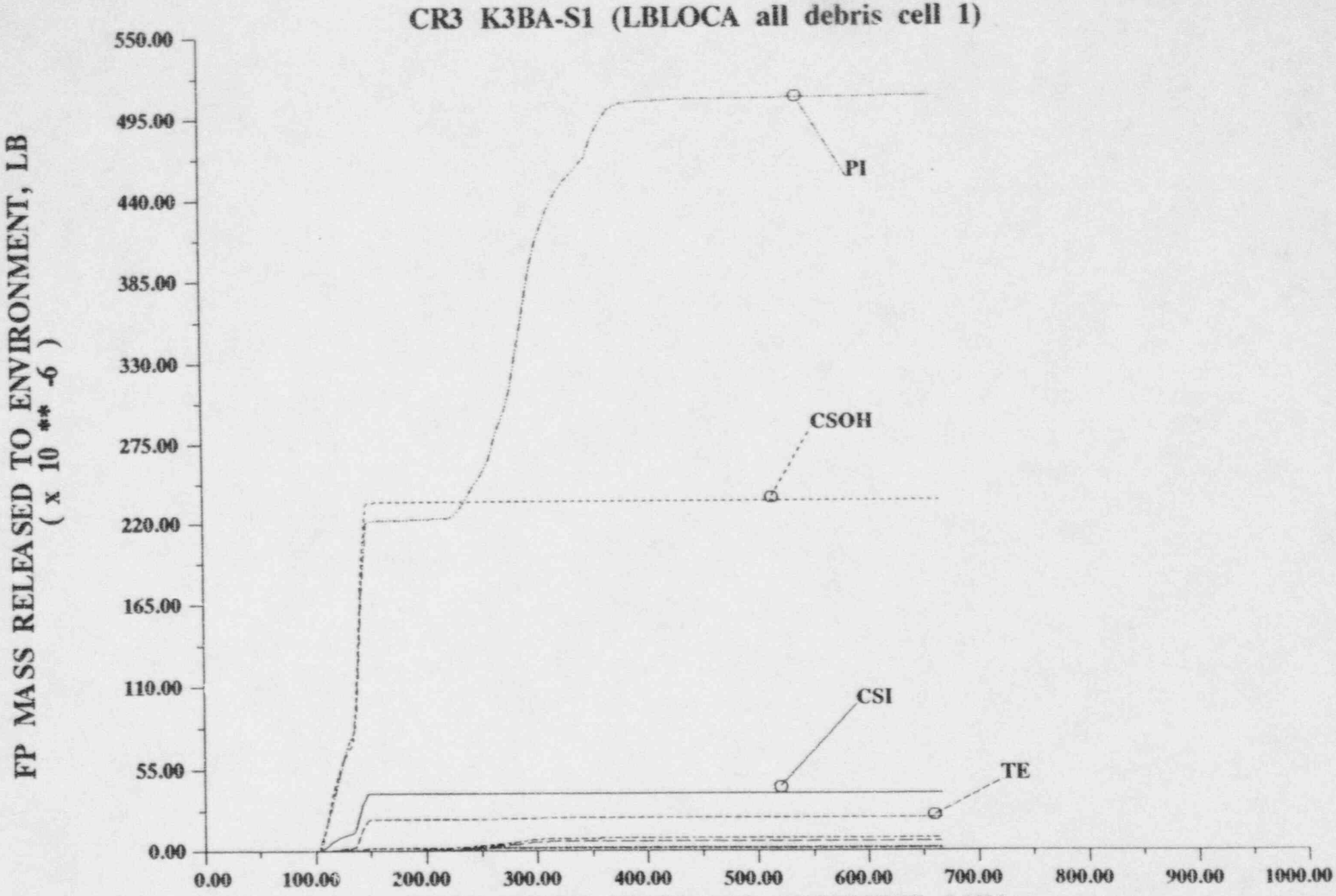

Figure A-13: FP MASS RELEASED TO ENVIRONMENT

11/25/91

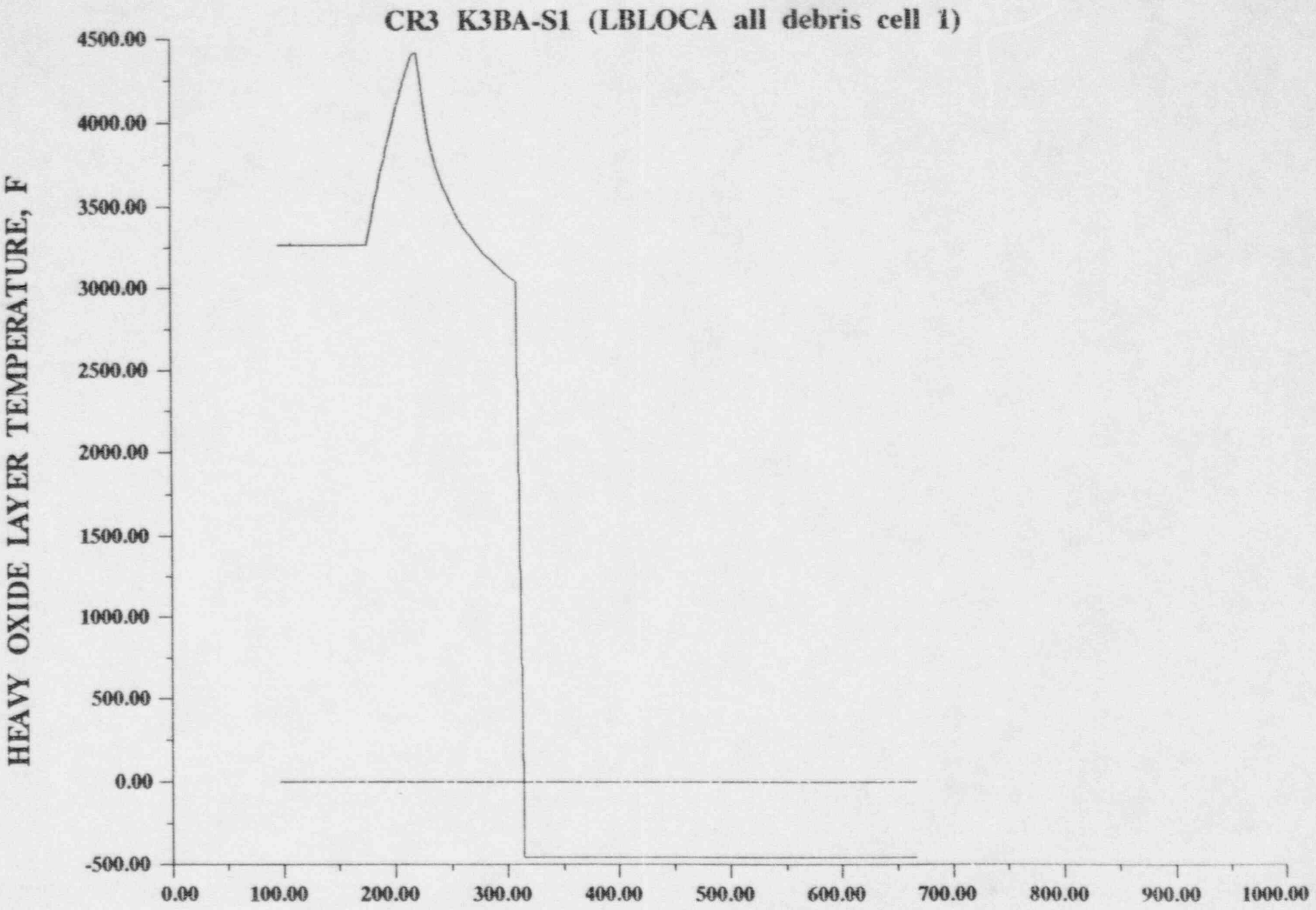

Figure A-14: HEAVY OXIDE LAYER TEMPERATURE

11/25/91

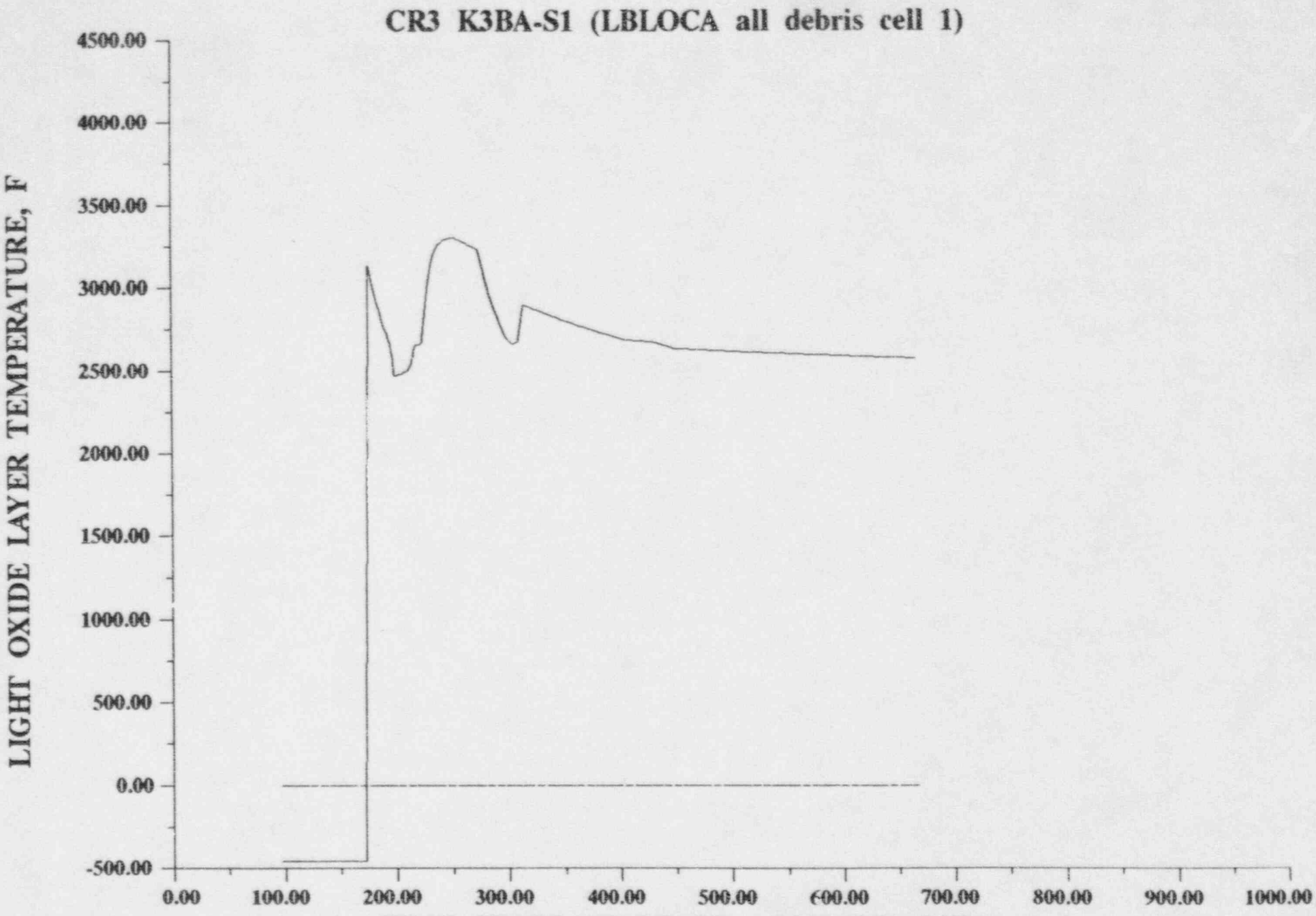

Figure A-16: LIGHT OXIDE LAYER TEMPERATURE

11/25/91

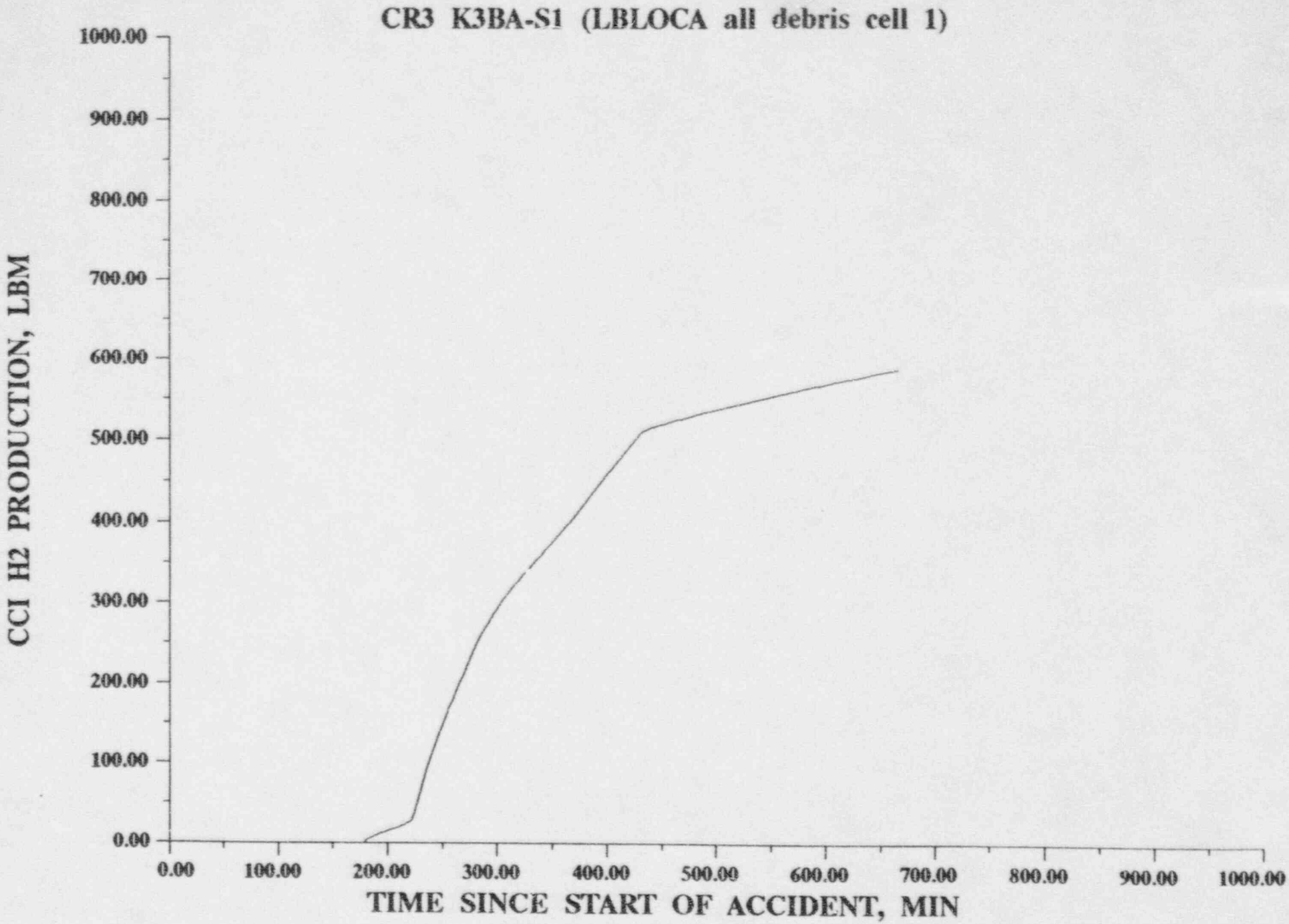

Figure A-17: CCI H2 PRODUCTION

11/25/91

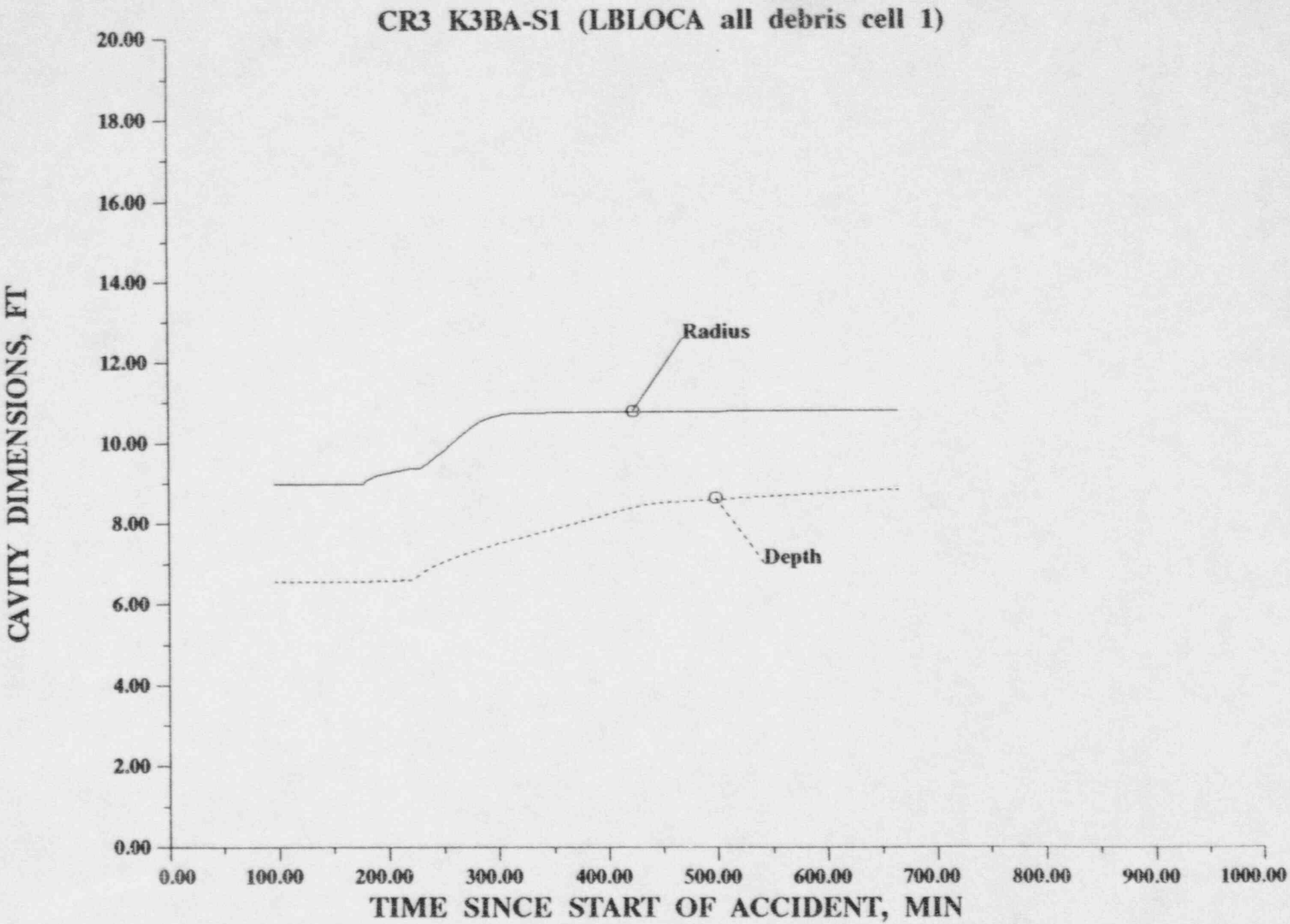

Figure A-21: CAVITY DIMENSIONS

11/25/91

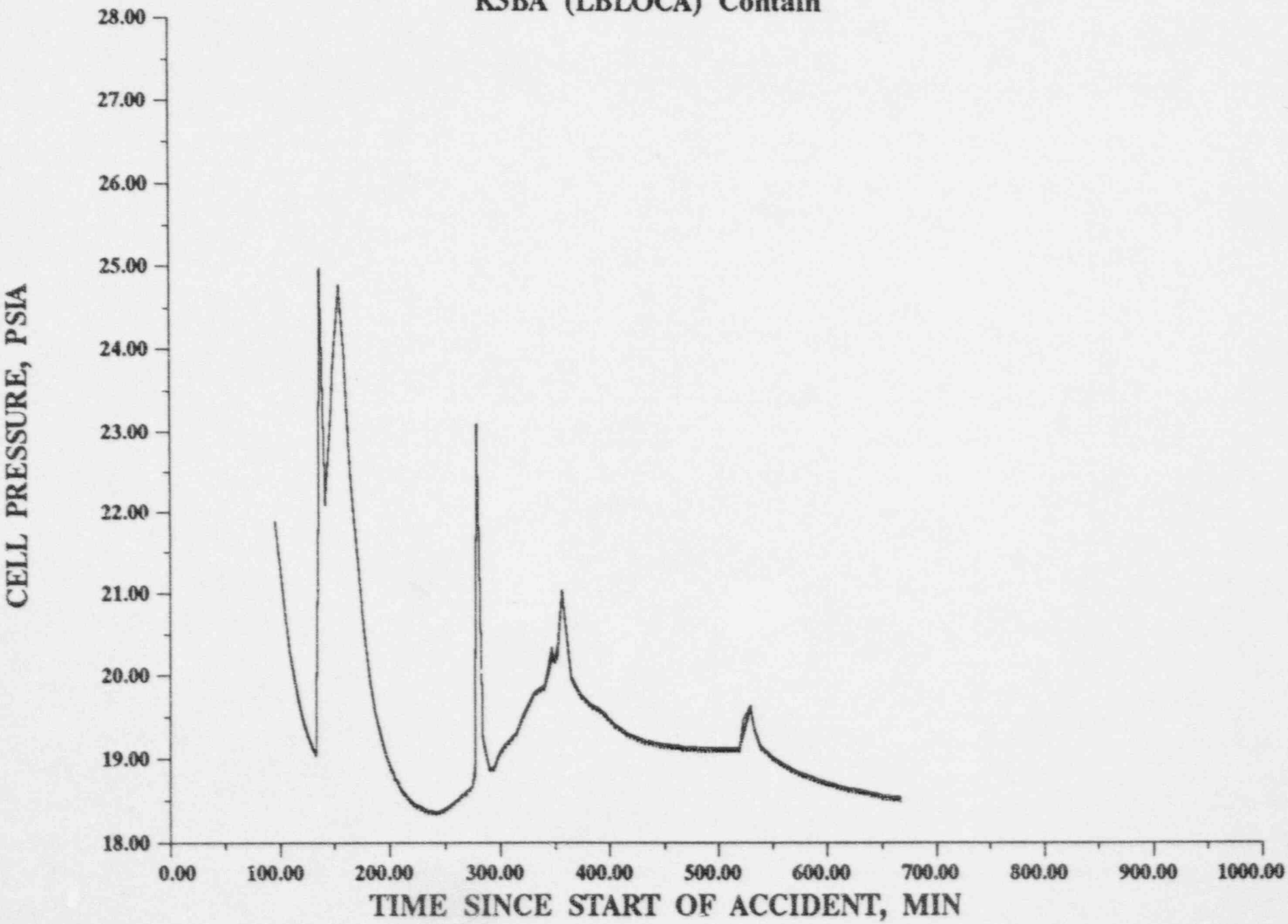

Question 42 - new Fig. 4.6.5-3

APPENDIX B

DCH Analysis Results

Table B.1-1: Fission Products Distribution

SIMPLE FISSION PRODUCT MASSES (KG) IN CELL 1 AT TIME = 90000.000 (S)

HOST	TYPE	NAME	1 CSI	2 CSOH	3 TE	4 SR	5 BA	6 LA
2	AEROSOL	UO2	2.97202E-08	7.16163E-09	2.16615E-04	1.44098E-06	4.12289E-06	2.25221E-07
0	TOTAL	ROOF	4.76773E-04	2.08931E-03	1.50405E-04	2.97015E-04	2.99675E-04	8.91387E-05
0	TOTAL	WALL	3.29824E-03	1.34675E-02	1.59925E-03	5.21227E-03	5.10516E-03	1.65177E-03
0	TOTAL	FLOOR	1.90007E-01	9.56478E-01	4.93591E-02	1.09754E-01	1.29817E-01	1.92109E-02
		TOTAL	1.93782E-01	9.72035E-01	5.13254E-02	1.15264E-01	1.35226E-01	2.09521E-02

HOST	TYPE	NAME	7 CE	8 RU	9 PI
2	AEROSOL	UO2	2.17329E-07	7.71241E-08	3.06698E-03
0	TOTAL	ROOF	8.04978E-05	2.19177E-08	9.76946E-03
0	TOTAL	WALL	1.42751E-03	1.47985E-07	1.29050E-01
0	TOTAL	FLOOR	1.77313E-02	9.34016E-07	7.10945E+00
		TOTAL	1.92395E-02	1.18104E-06	7.25134E+00

HOST MATERIAL INFORMATION IN CELL 1 AT TIME = 90000.000 (S)

HOST	TYPE	NAME	POWER (WATTS)	TEMPERATURE (K)
2	AEROSOL	UO2	0.00000E+00	1.41518E+03
0	TOTAL	ROOF	0.00000E+00	0.00000E+00
0	TOTAL	WALL	0.00000E+00	0.00000E+00
0	TOTAL	FLOOR	0.00000E+00	0.00000E+00
		TOTAL	0.00000E+00	

SIMPLE FISSION PRODUCT MASSES (KG) IN CELL 2 AT TIME = 90000.000 (S)

HOST	TYPE	NAME	1 CSI	2 CSOH	3 TE	4 SR	5 BA	6 LA
2	AEROSOL	UO2	1.73984E-07	4.19224E-08	9.48751E-04	8.31163E-06	1.92648E-05	1.06150E-06
0	TOTAL	WALL	9.50002E-03	3.47247E-02	1.11934E-02	1.02771E-02	1.07291E-02	2.52987E-03
0	TOTAL	FLOOR	3.71928E-02	1.47901E-01	4.06854E-02	9.42759E-02	9.80830E-02	1.88227E-02
		TOTAL	4.66930E-02	1.82626E-01	5.28275E-02	1.04561E-01	1.08831E-01	2.13536E-02

HOST	TYPE	NAME	7 CE	8 RU	9 PI
2	AEROSOL	UO2	1.02735E-06	2.97560E-07	1.43562E-02
0	TOTAL	WALL	1.47624E-03	1.71353E-06	6.74977E-01
0	TOTAL	FLOOR	1.52214E-02	2.18437E-06	5.01102E+00
		TOTAL	1.66986E-02	4.19546E-06	5.70035E+00

HOST MATERIAL INFORMATION IN CELL 2 AT TIME = 90000.000 (S)

HOST	TYPE	NAME	POWER (WATTS)	TEMPERATURE (K)
2	AEROSOL	UO2	0.00000E+00	5.03473E+02
0	TOTAL	WALL	0.00000E+00	0.00000E+00
0	TOTAL	FLOOR	0.00000E+00	0.00000E+00
		TOTAL	0.00000E+00	

SIMPLE FISSION PRODUCT MASSES (KG) IN CELL 3 AT TIME = 90000.000 (S)

HOST	TYPE	NAME	1 CSI	2 CSOH	3 TE	4 SR	5 BA	6 LA
2	AEROSOL	UO2	2.68919E-06	6.47937E-07	1.46663E-02	1.28460E-04	2.97794E-04	1.64087E-05
0	TOTAL	WALL	4.99151E-02	1.86072E-01	4.73255E-02	5.65103E-02	5.89655E-02	1.39796E-02
0	TOTAL	FLOOR	8.80347E-01	3.65522E+00	8.45159E-01	1.96678E+00	2.06055E+00	3.85393E-01
		TOTAL	9.30265E-01	3.84129E+00	9.07150E-01	2.02342E+00	2.11982E+00	3.99389E-01

HOST	TYPE	NAME	7 CE	8 RU	9 PI
2	AEROSOL	UO2	1.58807E-05	4.60020E-06	2.21915E-01
0	TOTAL	WALL	9.07215E-03	6.47682E-06	3.24951E+00
0	TOTAL	FLOOR	3.16266E-01	4.26222E-05	1.05393E+02
		TOTAL	3.25354E-01	5.36992E-05	1.08864E+02

HOST MATERIAL INFORMATION IN CELL 3 AT TIME = 90000.000 (S)

HOST	TYPE	NAME	POWER (WATTS)	TEMPERATURE (K)
2	AEROSOL	UO2	0.00000E+00	5.17865E+02
0	TOTAL	WALL	0.00000E+00	0.00000E+00
0	TOTAL	FLOOR	0.00000E+00	0.00000E+00
		TOTAL	0.00000E+00	

SIMPLE FISSION PRODUCT MASSES (KG) IN CELL 4 AT TIME = 90000.000 (S)

HOST	TYPE	NAME	1 CSI	2 CSOH	3 TE	4 SR	5 BA	6 LA
2	AEROSOL	UO2	4.61973E-06	1.10991E-06	2.53799E-02	2.19941E-04	5.14228E-04	2.83472E-05
0	TOTAL	WALL	7.19393E-01	3.70498E+00	1.18061E-01	1.36417E-01	1.65528E-01	3.35486E-02
0	TOTAL	FLOOR	4.26454E+00	2.28632E+01	1.01101E+00	1.98645E+00	2.51247E+00	3.17363E-01
		TOTAL	4.98394E+00	2.65682E+01	1.15445E+00	2.12308E+00	2.67851E+00	3.50940E-01

HOST	TYPE	NAME	7 CE	8 RU	9 PI
2	AEROSOL	UO2	2.74313E-05	7.99584E-06	3.82991E-01
0	TOTAL	WALL	2.48294E-02	6.98366E-06	9.26586E+00
0	TOTAL	FLOOR	2.84885E-01	1.84294E-05	2.14917E+02
		TOTAL	3.09742E-01	3.34089E-05	2.24565E+02

HOST MATERIAL INFORMATION IN CELL 4 AT TIME = 90000.000 (S)

HOST	TYPE	NAME	POWER (WATTS)	TEMPERATURE (K)
2	AEROSOL	UO2	0.00000E+00	6.34099E+02
0	TOTAL	WALL	0.00000E+00	0.00000E+00
0	TOTAL	FLOOR	0.00000E+00	0.00000E+00
		TOTAL	0.00000E+00	

SIMPLE FISSION PRODUCT MASSES (KG) IN CELL 5 AT TIME = 90000.000 (S)

HOST	TYPE	NAME	1 CSI	2 CSOH	3 TE	4 SR	5 BA	6 LA
2	AEROSOL	UO2	1.89494E-06	4.56217E-07	1.03523E-02	9.04372E-05	2.10094E-04	1.15777E-05
0	TOTAL	WALL	2.11283E-01	1.06565E+00	4.49992E-02	5.45779E-02	6.48391E-02	1.37388E-02
		TOTAL	2.11285E-01	1.06565E+00	5.53516E-02	5.46683E-02	6.50492E-02	1.37503E-02

HOST	TYPE	NAME	7 CE	8 RU	9 PI
2	AEROSOL	UO2	1.12048E-05	3.25059E-06	1.56537E-01
0	TOTAL	WALL	9.96590E-03	3.32162E-06	3.68991E+00
		TOTAL	9.97710E-03	6.57220E-06	3.84644E+00

HOST MATERIAL INFORMATION IN CELL 5 AT TIME = 90000.000 (S)

HOST	TYPE	NAME	POWER (WATTS)	TEMPERATURE (K)
2	AEROSOL	UO2	0.00000E+00	6.09881E+02
0	TOTAL	WALL	0.00000E+00	0.00000E+00
		TOTAL	0.00000E+00	

SIMPLE FISSION PRODUCT MASSES (KG) IN CELL 6 AT TIME = 90000.000 (S)

HOST	TYPE	NAME	1 CSI	2 CSOH	3 TE	4 SR	5 BA	6 LA
2	AEROSOL	UO2	2.21467E-06	5.31911E-07	1.21621E-02	1.05406E-04	2.46443E-04	1.35854E-05
0	TOTAL	WALL	1.27330E-01	5.65126E-01	4.03826E-02	7.22361E-02	7.97990E-02	1.85437E-02
		TOTAL	1.27332E-01	5.65127E-01	5.25447E-02	7.23415E-02	8.00454E-02	1.85573E-02

HOST	TYPE	NAME	7 CE	8 RU	9 PI
2	AEROSOL	UO2	1.31464E-05	3.83126E-06	1.83533E-01
0	TOTAL	WALL	1.34282E-02	3.40578E-06	3.82542E+00
		TOTAL	1.34414E-02	7.23704E-06	4.00895E+00

HOST MATERIAL INFORMATION IN CELL 6 AT TIME = 90000.000 (S)

HOST	TYPE	NAME	POWER (WATTS)	TEMPERATURE (K)
2	AEROSOL	UO2	0.00000E+00	6.26123E+02
0	TOTAL	WALL	0.00000E+00	0.00000E+00
		TOTAL	0.00000E+00	

SIMPLE FISSION PRODUCT MASSES (KG) IN CELL 7 AT TIME = 90000.000 (S)

HOST	TYPE	NAME	1 CSI	2 CSOH	3 TE	4 SR	5 BA	6 LA
2	AEROSOL	UO2	5.87498E-05	1.41430E-05	3.21024E-01	2.80356E-03	6.51458E-03	3.59004E-04
0	TOTAL	ROOF	1.49101E-02	6.54605E-02	9.07962E-04	2.33952E-04	6.51128E-04	4.82406E-05
0	TOTAL	WALL	1.26829E-01	5.77667E-01	1.81906E-02	1.75129E-02	2.41164E-02	3.56665E-03
		TOTAL	1.41798E-01	6.43142E-01	3.40122E-01	2.05504E-02	3.12821E-02	3.97389E-03

HOST	TYPE	NAME	7 CE	8 RU	9 PI
2	AEROSOL	UO2	3.47440E-04	1.00813E-04	4.85378E+00
0	TOTAL	ROOF	2.89081E-05	6.47085E-08	9.18698E-02
0	TOTAL	WALL	3.01389E-03	1.63024E-06	1.55448E+00
		TOTAL	3.39024E-03	1.02508E-04	6.50014E+00

HOST MATERIAL INFORMATION IN CELL 7 AT TIME = 90000.000 (S)

HOST	TYPE	NAME	POWER (WATTS)	TEMPERATURE (K)
2	AEROSOL	UO2	0.00000E+00	6.18730E+02
0	TOTAL	ROOF	0.00000E+00	0.00000E+00
0	TOTAL	WALL	0.00000E+00	0.00000E+00
		TOTAL	0.00000E+00	

SIMPLE FISSION PRODUCT MASSES (KG) IN CELL 8 AT TIME = 90000.000 (S)

HOST	TYPE	NAME	1 CSI	2 CSOH	3 TE	4 SR	5 BA	6 LA
2	AEROSOL	UO2	2.60811E-05	6.41928E-06	1.40137E-01	1.25935E-03	2.84964E-03	1.58000E-04
0	TOTAL	WALL	8.18229E-02	3.56996E-01	1.81606E-02	3.16128E-02	3.52135E-02	9.21412E-03
0	TOTAL	FLOOR	1.12233E+01	5.61161E+01	4.54524E+00	1.16661E+01	1.31806E+01	1.93050E+00
		TOTAL	1.13051E+01	5.64731E+01	4.70354E+00	1.16989E+01	1.32187E+01	1.93987E+00

HOST	TYPE	NAME	7 CE	8 RU	9 PI
2	AEROSOL	UO2	1.52954E-04	4.30976E-05	2.13835E+00
0	TOTAL	WALL	5.85682E-03	1.82834E-06	1.66853E+00
0	TOTAL	FLOOR	1.72677E+00	5.93265E-05	7.07830E+02
		TOTAL	1.73278E+00	1.04252E-04	7.11637E+02

HOST MATERIAL INFORMATION IN CELL 8 AT TIME = 90000.000 (S)

HOST	TYPE	NAME	POWER (WATTS)	TEMPERATURE (K)
2	AEROSOL	UO2	0.00000E+00	5.82851E+02
0	TOTAL	WALL	0.00000E+00	0.00000E+00
0	TOTAL	FLOOR	0.00000E+00	0.00000E+00
		TOTAL	0.00000E+00	

SIMPLE FISSION PRODUCT MASSES (KG) IN CELL 9 AT TIME = 90000.000 (S)

HOST	TYPE	NAME	1 CSI	2 CSOH	3 TE	4 SR	5 BA	6 LA
2	AEROSOL	UO2	5.70876E+00	2.14876E+01	6.16851E-01	2.13763E+00	2.30872E+00	8.69210E-01
0	TOTAL	FLOOR	1.46785E+00	5.52660E+00	1.19499E-01	5.32757E-01	5.76213E-01	2.21142E-01
		TOTAL	7.17661E+00	2.70142E+01	7.36350E-01	2.67039E+00	2.88494E+00	1.09035E+00

HOST	TYPE	NAME	7 CE	8 RU	9 PI
2	AEROSOL	UO2	3.48630E-01	3.09864E-05	6.33975E+01
0	TOTAL	FLOOR	8.78861E-02	1.09137E-06	1.43678E+01
		TOTAL	4.36516E-01	3.20777E-05	7.77652E+01

HOST MATERIAL INFORMATION IN CELL 9 AT TIME = 90000.000 (S)

HOST	TYPE	NAME	POWER (WATTS)	TEMPERATURE (K)
2	AEROSOL	UO2	0.00000E+00	3.00755E+02
0	TOTAL	FLOOR	0.00000E+00	0.00000E+00
		TOTAL	0.00000E+00	

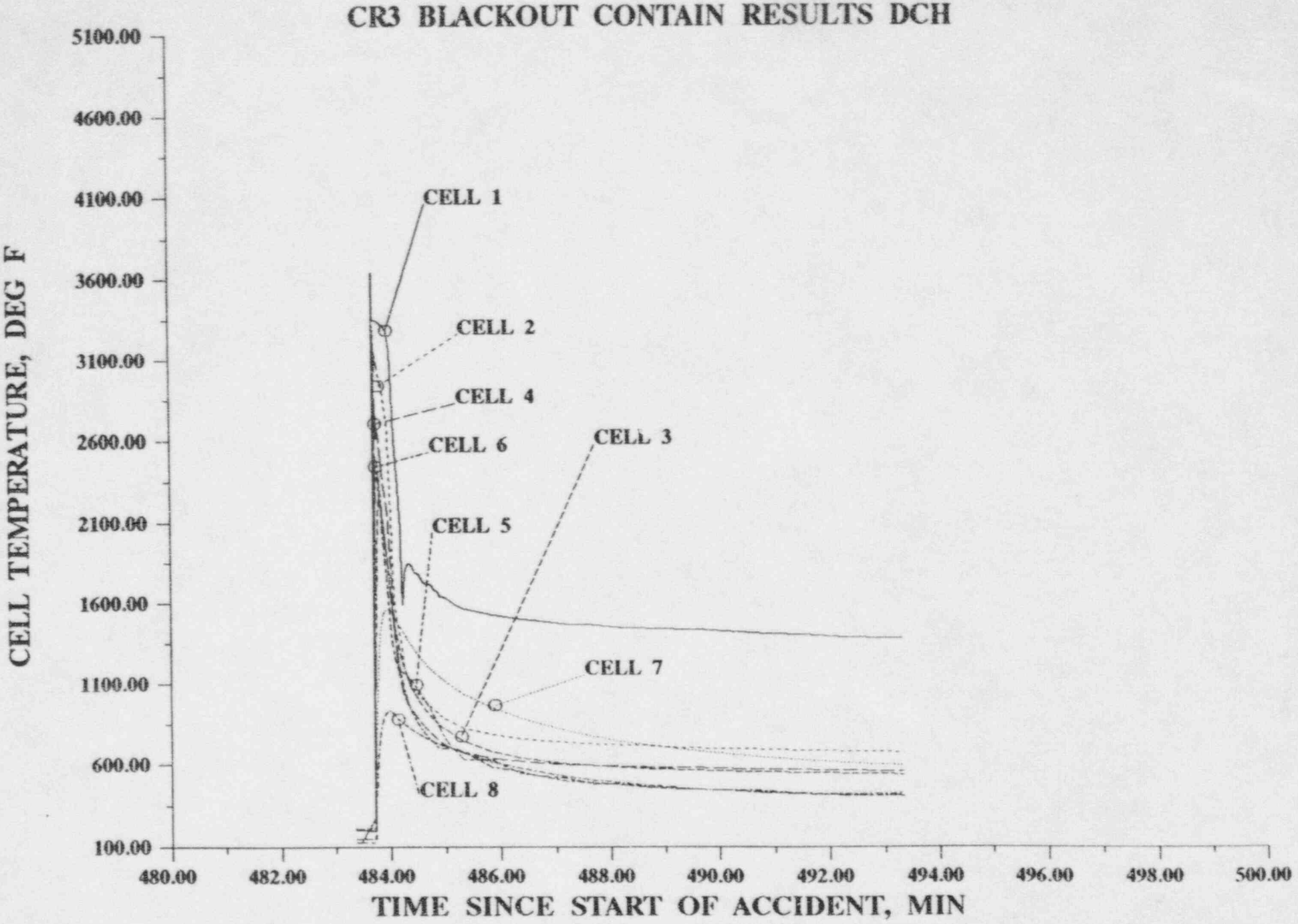

Figure B-1: CELL TEMPERATURE

10/16/91

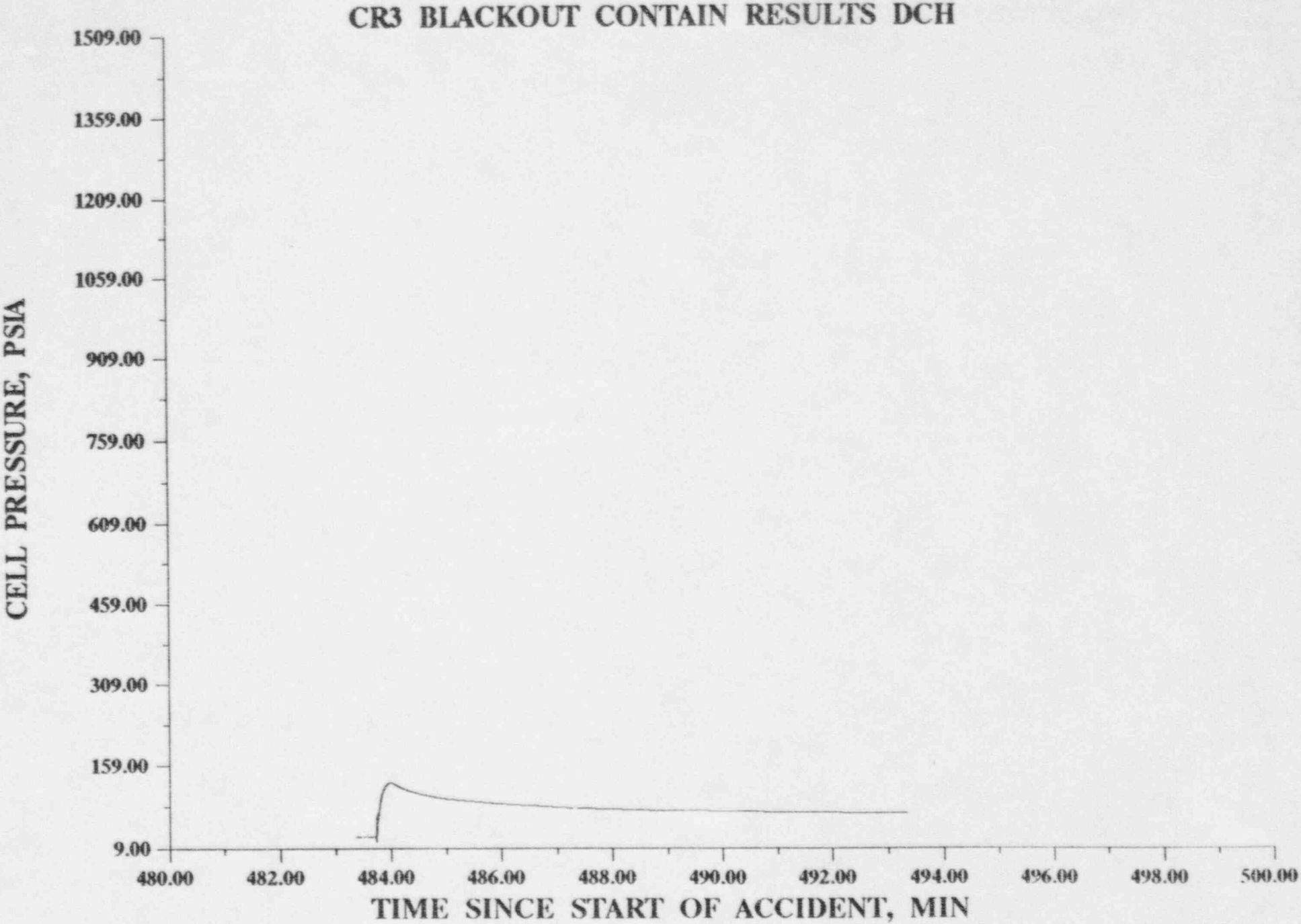

Figure B-4: CELL PRESSURE

10/16/91

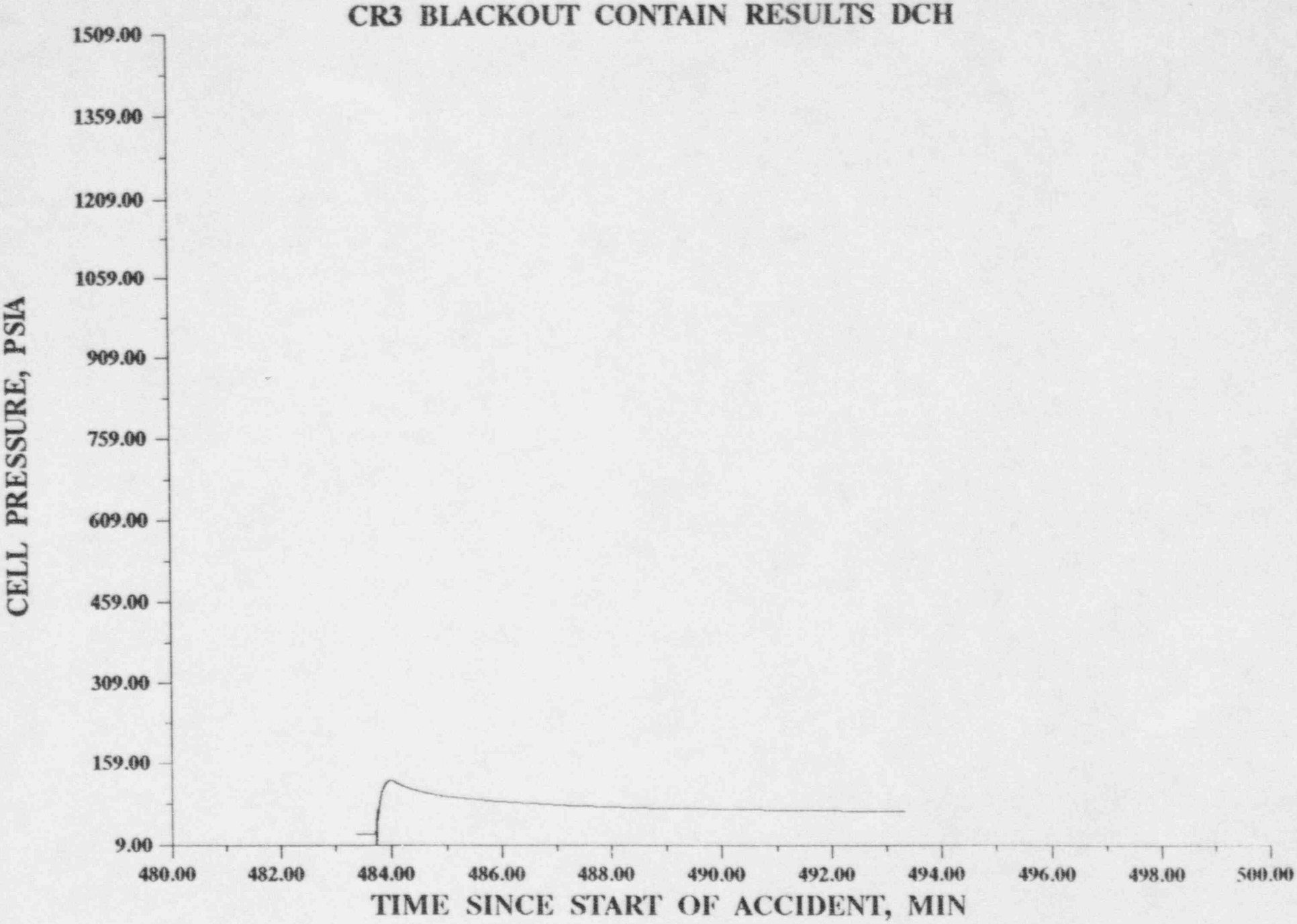

Figure B-5: CELL PRESSURE

10/16/91

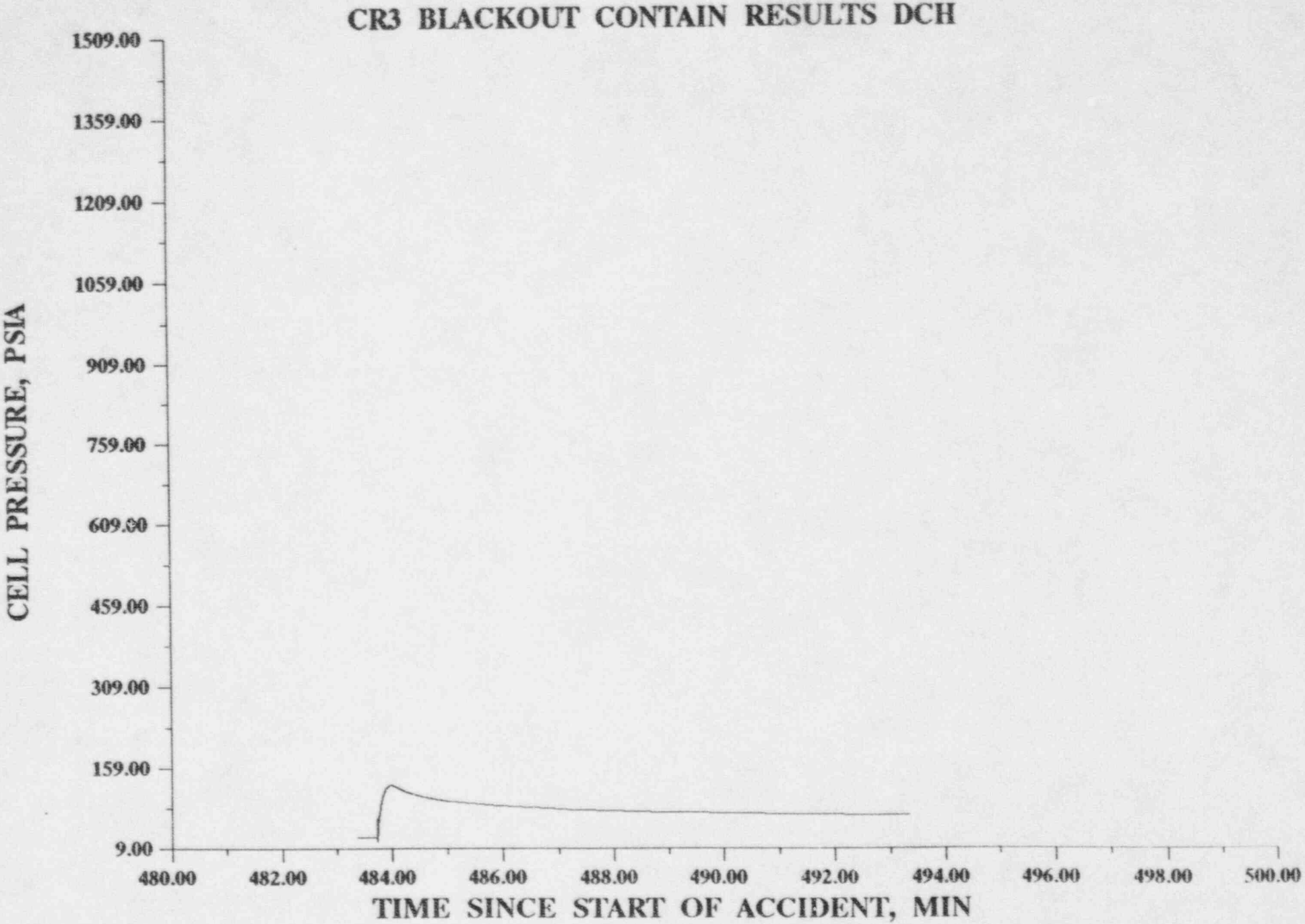

Figure B-6: CELL PRESSURE

10/16/91

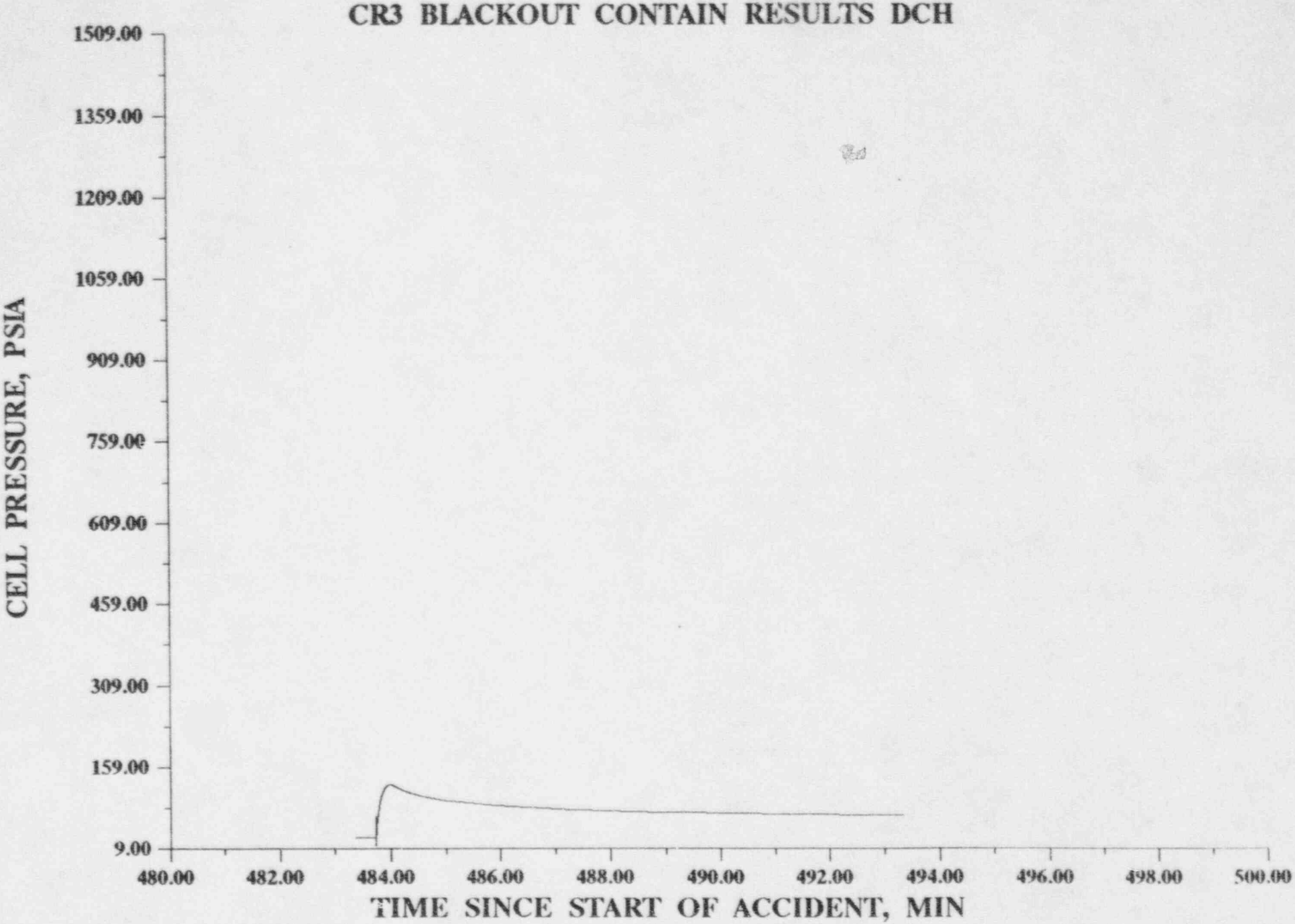

Figure B-7: CELL PRESSURE

10/16/91

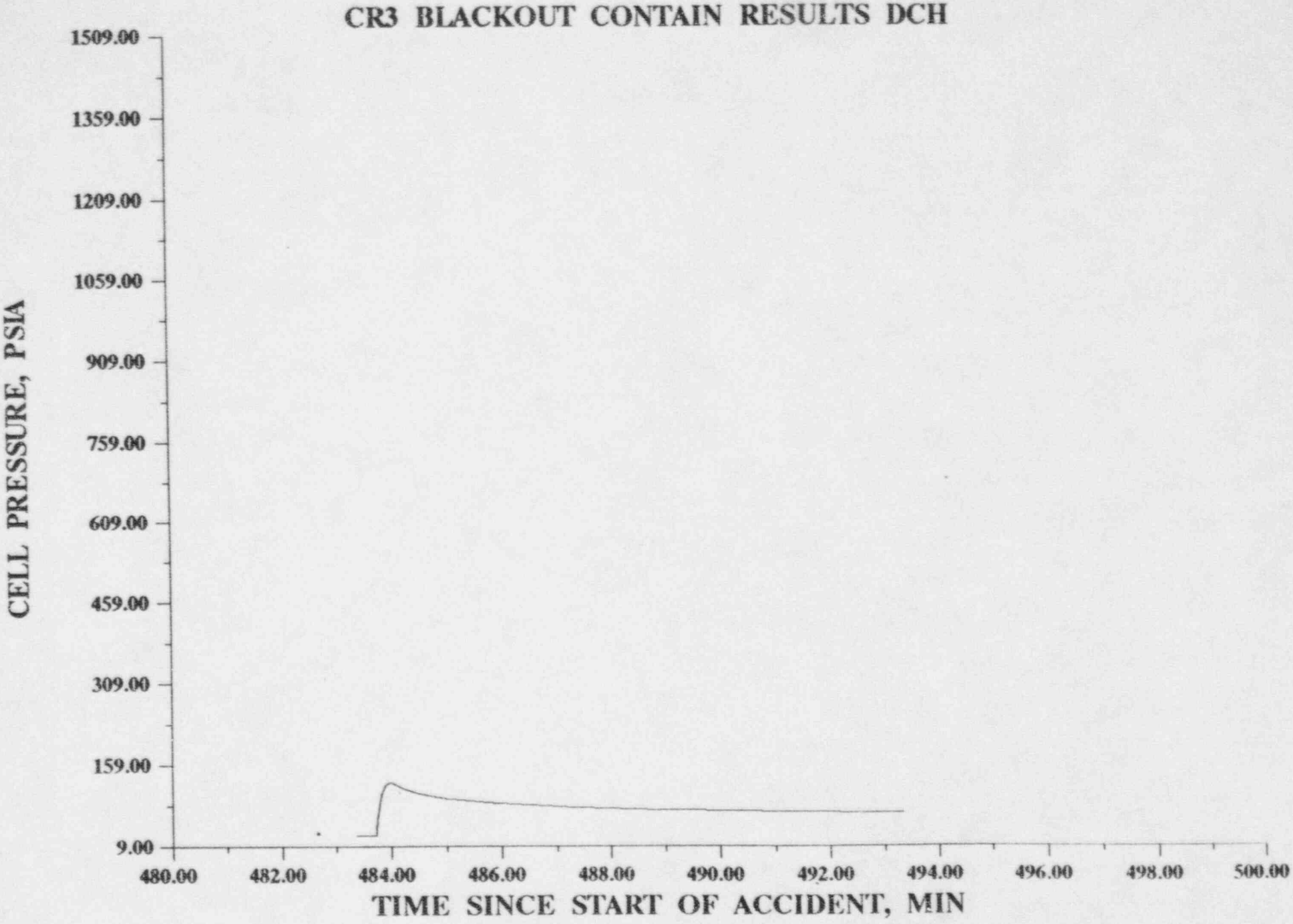

Figure B-8: CELL PRESSURE

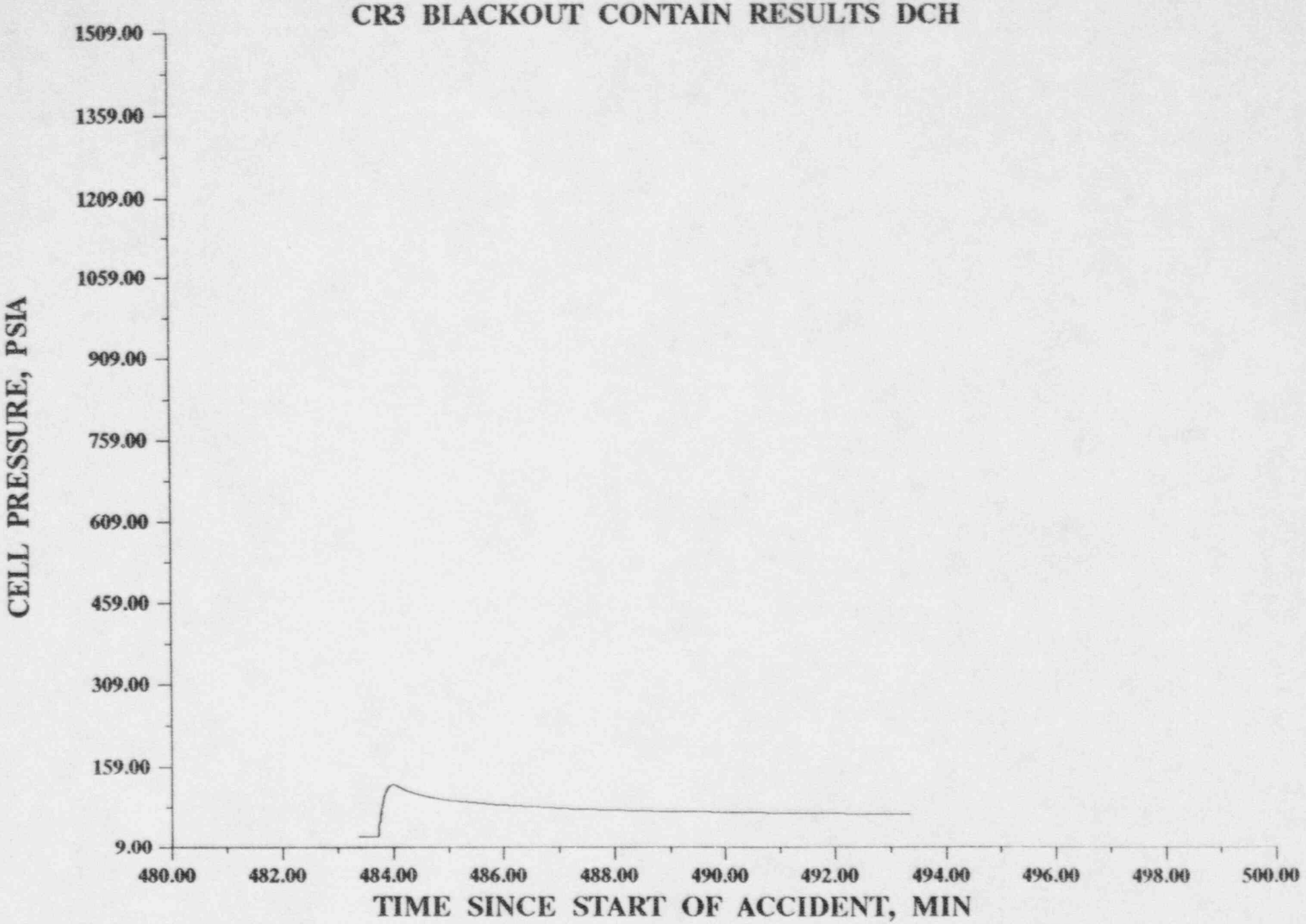

Figure B-9: CELL PRESSURE

10/16/91

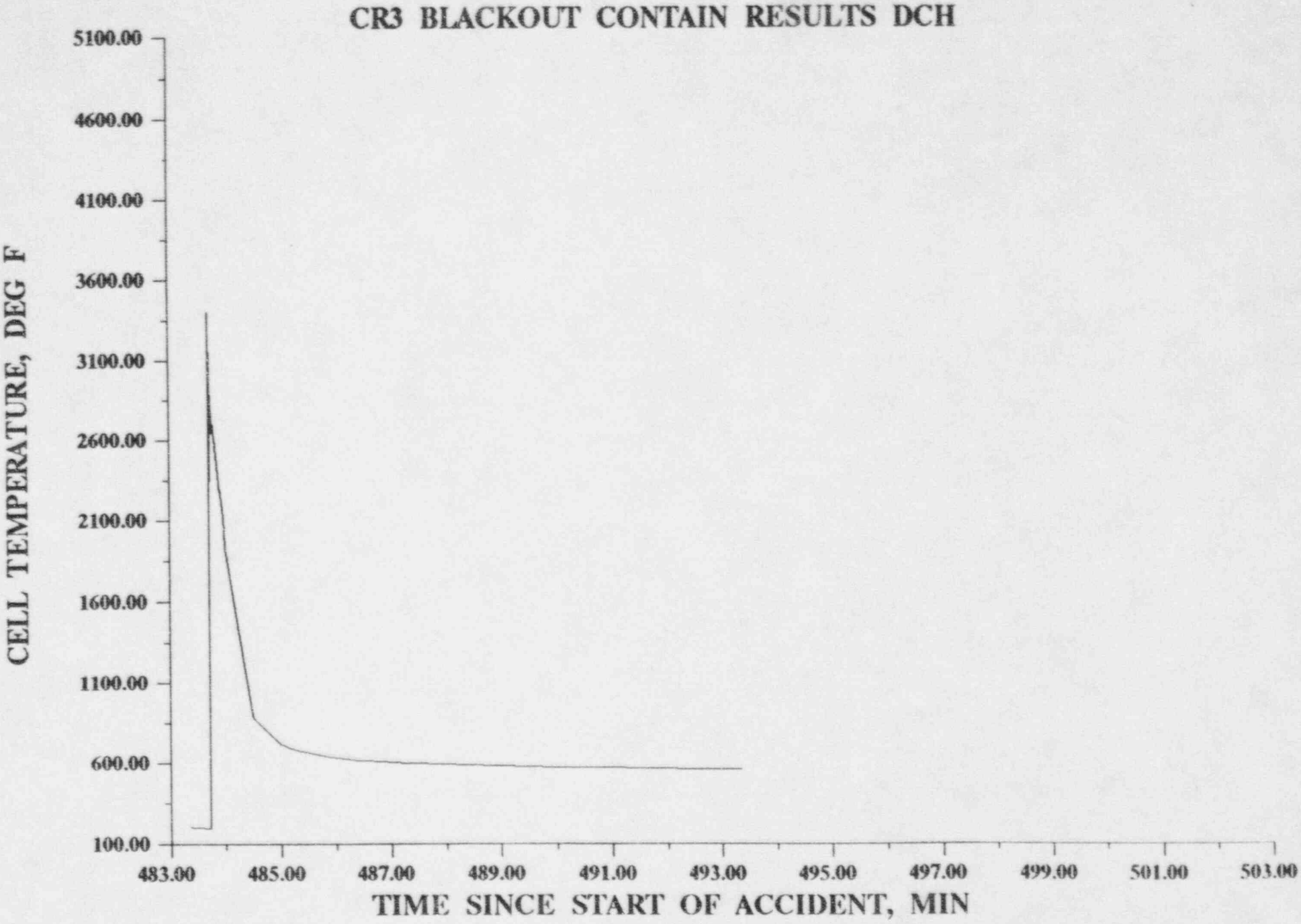

Figure B-10: CELL TEMPERATURE

10/17/91

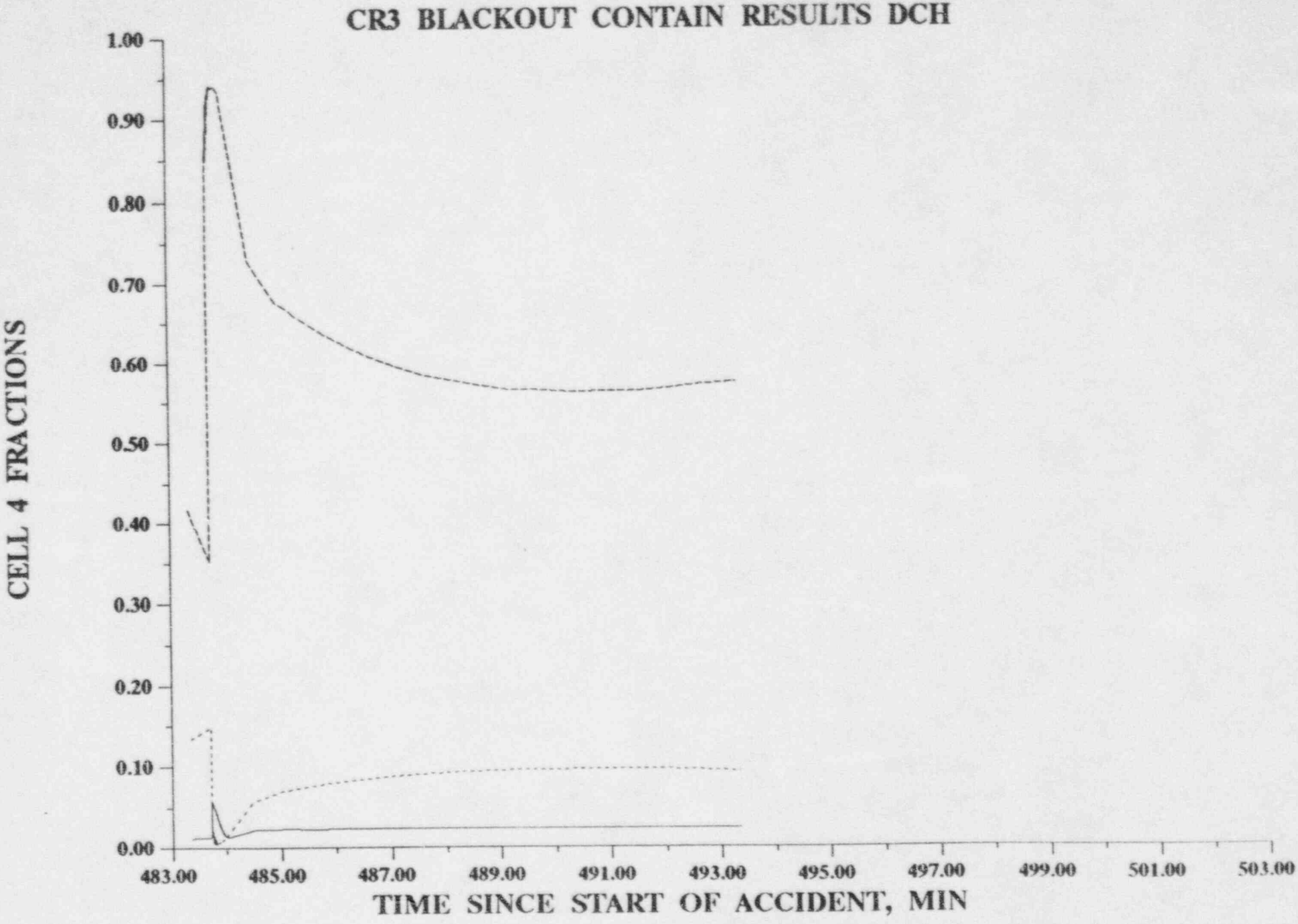

Figure B-11: CELL 4 FRACTIONS

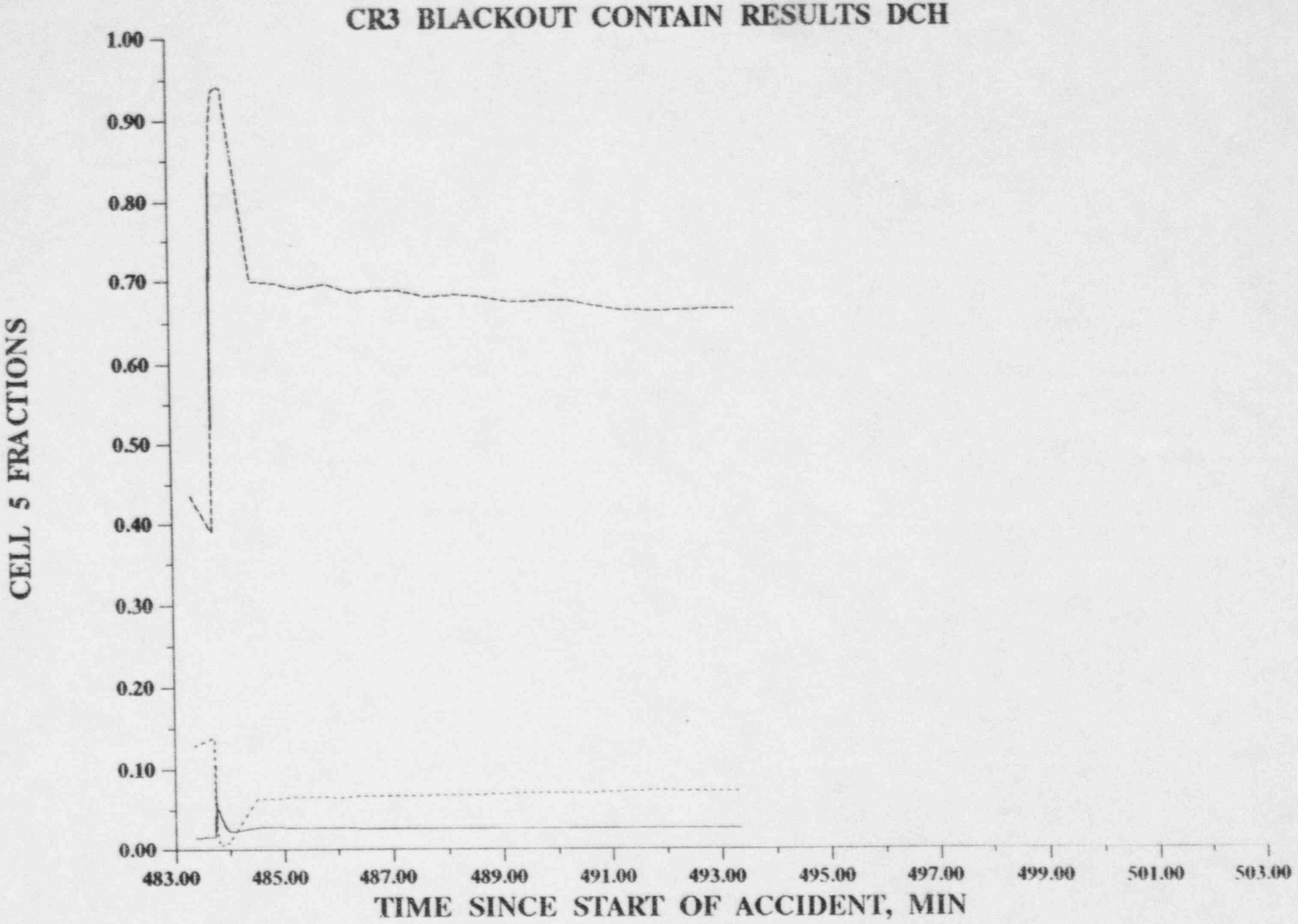

Figure B-12: CELL 5 FRACTIONS

10/17/91

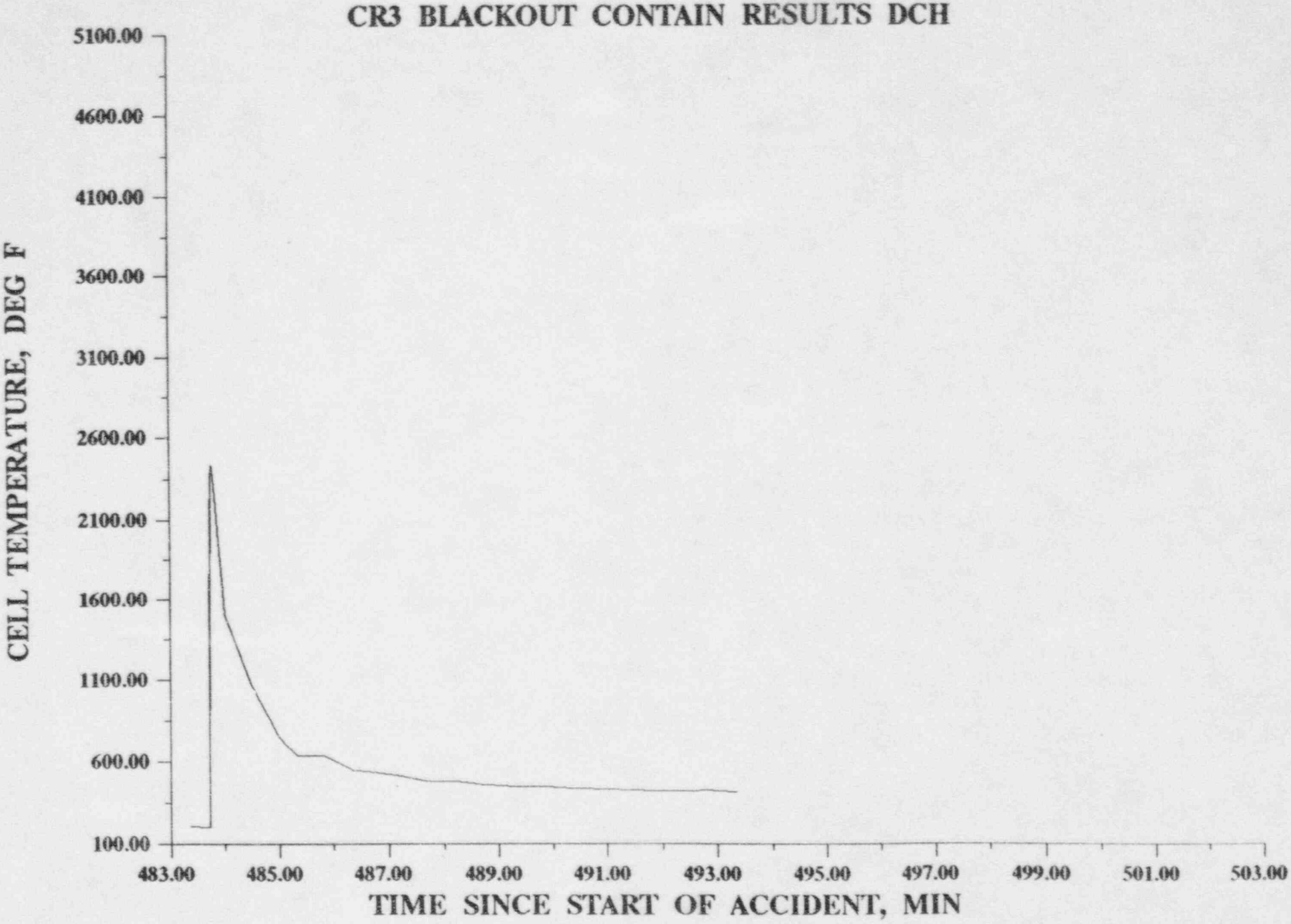

Figure B-13: CELL TEMPERATURE

10/17/91

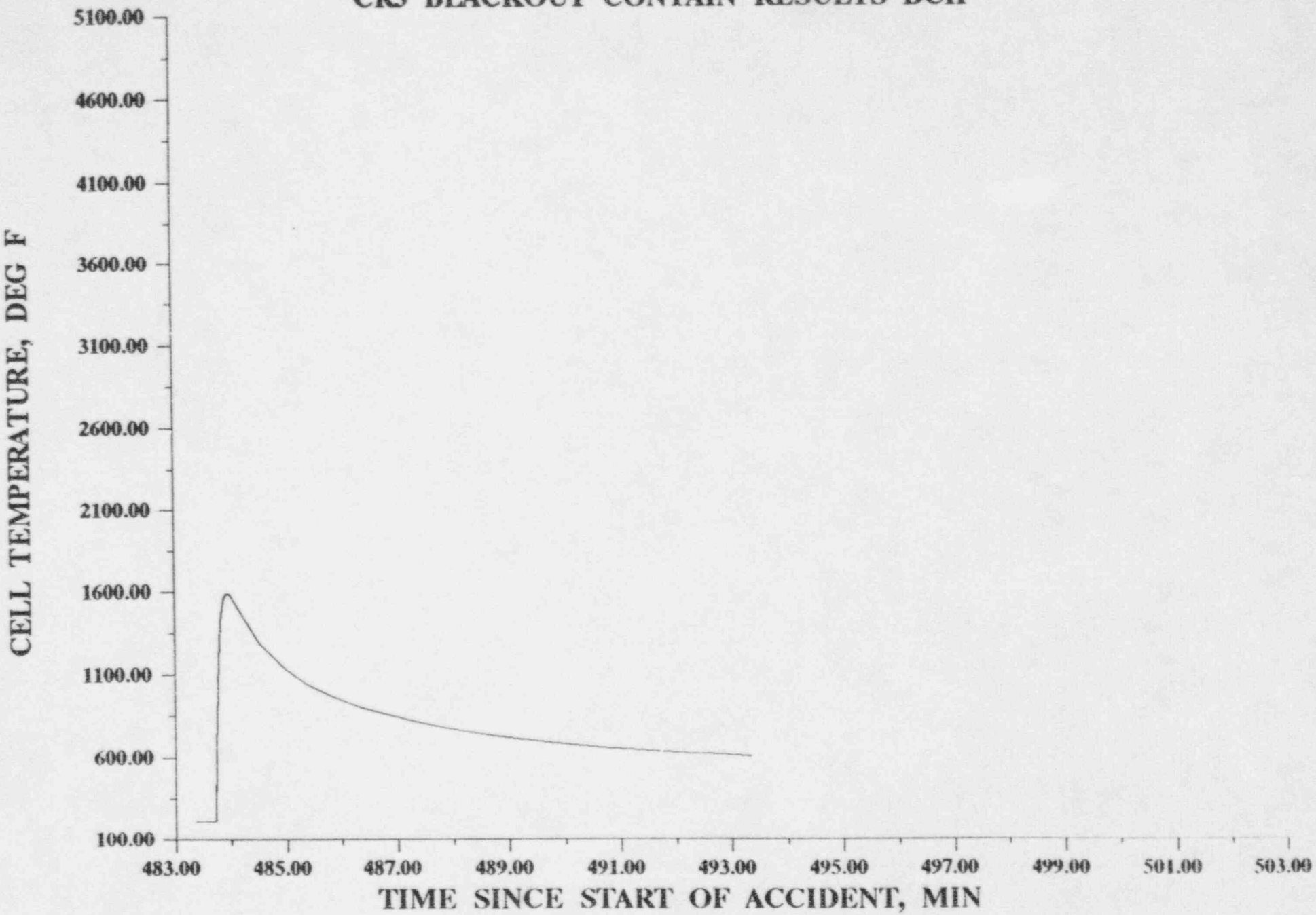

Figure B-14: CELL TEMPERATURE

10/17/91

APPENDIX C

CONTAINMENT RESPONSE TO COMBUSTION OF HYDROGEN

C.1 Introduction

The temperature and pressure response to a postulated hydrogen burn in the containment was analyzed for the CR-3 plant. The amount of hydrogen burned was treated as a parameter in the form of an effective fraction of zirconium reacted. The core contains 50,100 lb of zirconium and a 100% zirconium reaction would correspond to 1,100 lb-moles of hydrogen. Hydrogen generated from sources other than zirconium steam reactions can be converted to equivalent fractions of zirconium reacting and added in so that theoretically, more than 1,100 lb-moles of hydrogen could be available. However, in practice, due to the inability to react all of the zirconium in the core and because early in the accident sequence other hydrogen sources are generally small, a 100% zirconium reaction is considered to be a very conservative upper limit, at least for considerations of early containment failure.

The hydrogen combustion reaction consumes 0.5 lb-mole of oxygen for every 1.0 lb-mole of hydrogen and it liberates 104,000 BTU of exothermic energy for each lb-mole of hydrogen burned. Thus, the combustion of 1,100 lb-moles of hydrogen would consume 550 lb-moles of oxygen. The CR-3 containment volume is 2.04×10^6 cubic feet, and 550 lb-moles of oxygen corresponds to about 52% of all the oxygen in the containment at 100 °F. Thus, there is sufficient oxygen to react all the hydrogen potentially generated at early times.

The heat of reaction of 104,000 Btu/lb-mole is smaller than the value of 124,000 Btu/lb-mole frequently seen in the literature. The former is called the lower heat of combustion and considers the reaction product (H_2O) as a vapor; the latter value is called the upper heat of combustion. It considers the reaction product as liquid water and thus includes the heat of condensation. The reaction products immediately following a hydrogen burn will be in the vapor state and thus the correct heat balance to determine containment pressure is made with the lower heat of combustion. The combustion of 1,100 lb-moles of hydrogen would release 114 million BTU of energy which corresponds to 49 full core power seconds or the first 40 minutes of decay heat.

The effect of a hydrogen burn on the containment pressure and temperature is bounded by an adiabatic heatup of the containment gas mixture by the chemical energy of combustion. This is usually a reasonably good approximation, particularly for hydrogen concentrations of around 8% or more, because the burn completes in a few seconds and the energy loss to the containment structures over the duration of the burn is small. However, it is important to account for the incompleteness

of the burn (burn efficiency), and for the temperature-dependent specific heats of the constituent gases because of the high post-burn temperatures. For the subsequent calculations, temperature-dependent internal energies of the constituent gases are taken from Reference C-1.

C.2 Global Hydrogen Burning

It is known from experimental data (Reference C-2) that for combustion of lean mixtures in a quiescent atmosphere, the pressure rise is significantly lower than predicted by an adiabatic complete burn model. This is in large part due to the fact that lean flammable mixtures do not burn completely. For example, a 5.6% hydrogen concentration would only burn to about 50% completeness, an 8% concentration would burn about 85% complete, and an 11% concentration would burn about 95% complete (Reference C-2). In agitated or turbulent atmospheres, however, the data compiled in Reference C-2 indicate that significantly higher pressure rises can occur in the range of 4 to 8% hydrogen compared to quiescent atmospheres. In a large, dry containment with the debris heat source at the lowest elevation, it is expected that substantial mixing currents and convection will occur and that the containment atmosphere is agitated. As shown in Figure C-1 from Reference C-2, the data on burn pressure rise for agitated atmosphere tests are bounded by a pressure rise efficiency or burn efficiency which varies linearly from zero at 4% hydrogen to 100% at 8% hydrogen. This correlation has been incorporated into a constant volume, adiabatic burn model with temperature-dependent specific heats from Reference C-1, which was used to calculate the post-burn temperatures and pressures for different initial conditions. The results are shown in Figure C-2 in the form of a hydrogen burn nomogram for the CR-3 plant. Figure C-2 shows the results as a function of the pre-burn containment atmosphere temperature, ranging from 100 °F to 350 °F, and of the amounts of zirconium reacted, ranging from 0 to the equivalent of 150% of the core zirconium inventory. The results of Figure C-2 apply for a saturated containment atmosphere. In severe accidents, the containment atmosphere always has a significant steam content, typically in the range of 50% to 100% of saturated conditions at the containment temperature. Hydrogen burn calculations were also performed for 50% and 75% saturation conditions, and the results are very similar to Figure C-2. Figure C-3 shows the maximum post-burn pressure (i.e., the highest pressure in the shaded area of Figure C-2) as a function of the steam saturation fraction. It is seen that the maximum pressure is nearly independent of the saturation fraction between 50% and 100%. Therefore, Figure C-2 will be used together with the results from the CONTAIN analyses for hydrogen burns to estimate all hydrogen burn split fractions.

The lower portion of Figure C-2 shows the hydrogen concentration as a function of the fraction of zirconium reacted at the six different preburn temperatures. The concentration of hydrogen in the containment depends only slightly on the normal temperature of the air. More importantly, it depends on the amount of steam in the air at the time when the burn initiates. At 100 F, there are initially 5,000 lb-moles of air in the CR-3 containment. If, after primary system blowdown, saturated steam and air equilibrate at a typical value of 200 °F, about 3,370 lb-moles of steam are mixed with the air. Thus the steam concentration would be about 40 percent. At higher equilibrium temperatures, the amount of saturated steam increases further.

It can be seen in Figure C-2 that the global flammability limit of 8% cannot be reached with a 100% zirconium reaction fraction if the saturated steam atmosphere is at a temperature of 240 °F or higher. In dry air, an 8% hydrogen concentration would be reached when approximately 40% of the zirconium is reacted. The analysis assumes that the flammability limits are independent of the type of non-reacting diluent which is assumed to be nitrogen. However, steam is known to be a more effective diluent than nitrogen and, thus, there would be a slight increase in the flammability limits for increasing steam concentrations, which is neglected in the analysis.

The post-burn pressure is shown in the upper portion of Figure C-2. The area within the heavy lines indicates the area of interest for global burn conditions. This area is bounded by the lower flammability limit at 4% on the left, by the curve for which the steam concentration does inert the atmosphere on the upper left, which corresponds to a saturation temperature of approximately 240 °F, and by the curve at the top which corresponds to 100% of the core zirconium reacted. A steam-hydrogen-air mixture is steam inerted if the steam concentration is about 56% (Reference C-2) irrespective of the hydrogen and oxygen concentration. A saturated atmosphere is steam inerted at a temperature of about 240 °F. At 50% saturation, the atmosphere is inerted at a temperature of 300 °F. The shaded area in Figure C-2 indicates that the pressure in the CR-3 containment due to global hydrogen burning can not exceed 140 psia, even if hydrogen generation from as much as 100% of the core zirconium is considered. Figure C-3 shows that this maximum hydrogen burn pressure is nearly independent of the steam saturation fraction. At 75% zirconium oxidation, the maximum hydrogen burn pressure is seen to be 107 psia and at 50% zirconium oxidation the maximum pressure is only 72 psia.

Figure 4.4-2 in Section 4.4 shows the probability of containment failure as a function of pressure. It is noted that the probability of containment failure from hydrogen burning in the CR-3

containment could be as high as 0.53 from the limiting hydrogen burn in the shaded area of Figure C-2. The adiabatic burn model may be conservative by a few psi, but the conclusion remains that a hydrogen burn could challenge the CR-3 containment.

The nomogram can be read either for a "percent zirconium reacted" value on the lower left axis, or from a "hydrogen concentration" value on the bottom axis. The line with arrows gives an example for reading the nomogram at 80% zirconium reacted, and a preburn temperature of 200 °F. This nomogram is used extensively to quantify the hydrogen burn and containment failure split fractions on the containment event tree as explained in Section 4.7.

C.3 Continuous Discharge Burning of Hydrogen

Hydrogen does not necessarily have to accumulate in the containment until a globally flammable mixture is obtained. Hydrogen can also ignite at the point of release from the primary system or from an inerted region and burn continuously as a flame torch at the point of release. Discharge flames have not been studied as extensively in the past as global burns. For a fixed quantity of hydrogen burned, discharge burns can potentially yield higher pressures than global burns if the quantity of hydrogen burned corresponds to less than an 8% concentration in the containment. This is due to the reduction in burn efficiency for hydrogen quantities that would yield a global hydrogen concentration of less than 8%. The global burn efficiency limit does not necessarily apply to a discharge burn. In fact, a highly concentrated discharge flame can burn completely, whereas the same quantity of hydrogen when distributed in the containment, may only yield a concentration of less than 4% and not burn at all. Figure C-4 shows the hydrogen burn map for discharge burns. It differs from Figure C-3 in that it does not include a reduction in the burn completeness below 8% hydrogen concentrations. This figure should be used for any situation where all the hydrogen burns. This can occur either as a discharge burn with a flammable mixing zone or in a hypergolic recombination.

A discharge burn can occur either at the location of a break in the primary system, such as a small or large LOCA break, or at the PORV drain tank relief valve. It can also occur at the point of release into the main containment volume if the containment sub-volume at the release location is inerted. Alternatively, for small LOCAs and transients, a discharge burn can occur at vessel failure as a result of the rapid discharge of the RCS steam and hydrogen inventory out of the reactor cavity region into the main containment volume. In order to assess the flammability of a hydrogen-steam mixture discharging into an air-steam mixture, use is made of the air-steam-hydrogen flammability

diagram shown in Figure C-5 from Reference C-3. The containment atmosphere steam concentration is marked on the lower scale and the hydrogen concentration in the primary system steam is marked on the slanting scale. The two points are connected to obtain the mixing line, which indicates the possible compositions of mixed gases. If the mixing line crosses into the flammable domain, a discharge burn is possible if ignited. By drawing the tangent to the flammability curve from the containment atmosphere composition point, it is possible to determine the minimum concentration of hydrogen required in the discharge mixture for flammability. This is shown to be 70% in the example in Figure C-5.

References for Appendix C

C-1 Ashley, S. Campbell, Thermodynamic Analysis of Combustion Engines, John Wiley and Sons, New York, 1979.

C-2 Sherman, M. P., et al, "The Behavior of Hydrogen During Accidents in Light Water Reactors," USNRC Report NUREG/CR-1561 (SAND80-1495), Sandia National Laboratories, August 1980.

C-3 Pickard, Lowe and Garrick, Inc.,"Seabrook Station Probabilistic Safety Analysis," prepared for Public Service Company of New Hampshire and the Yankee Atomic Electric Company, PLG-0300, December 1983.

Figure C-1: Experimentally Determined Pressure Rise From Hydrogen Burns (Data from Reference C-2)

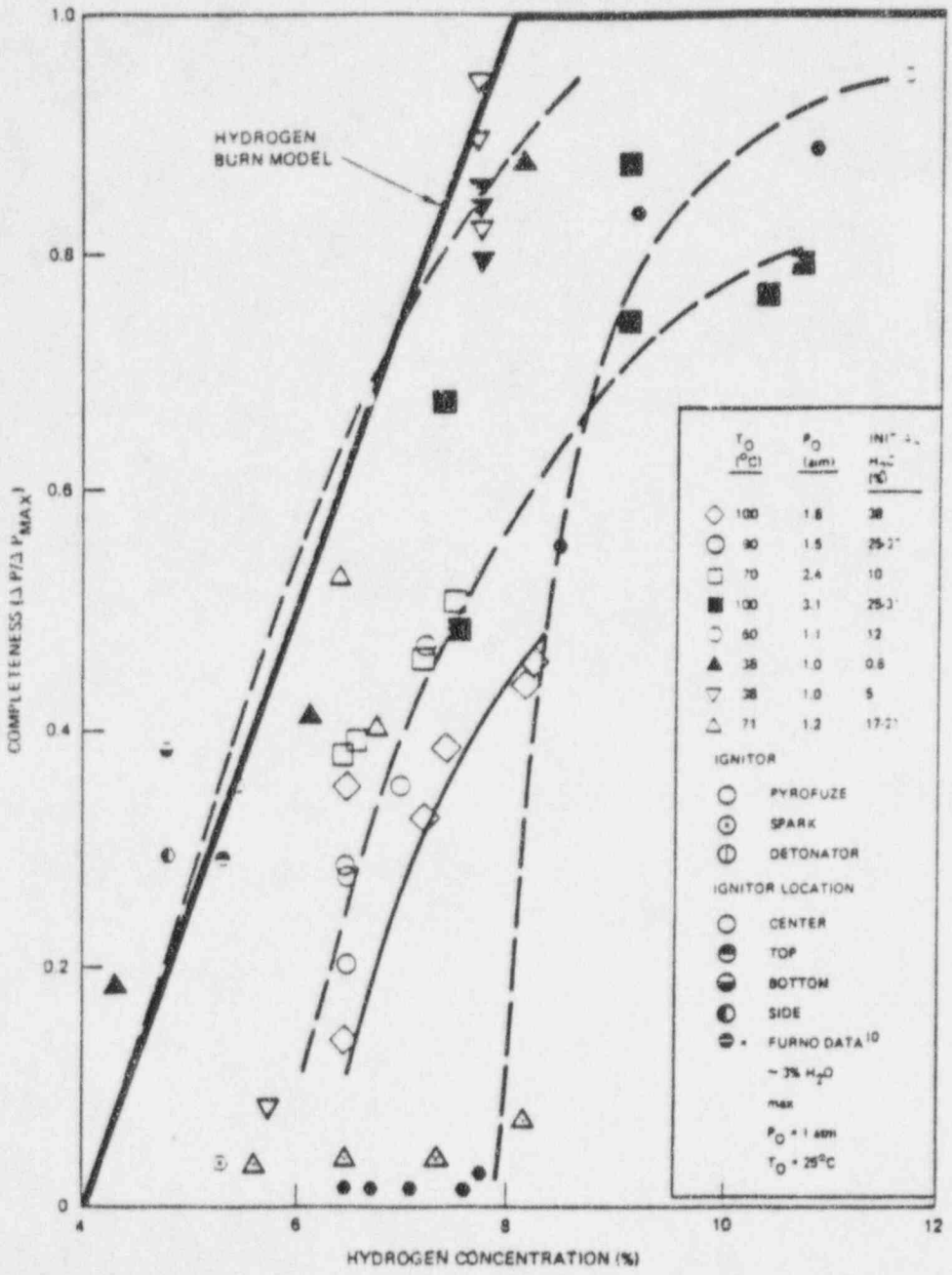

Figure C-2: Hydrogen Burn Map for Saturated Conditions – Global Burns

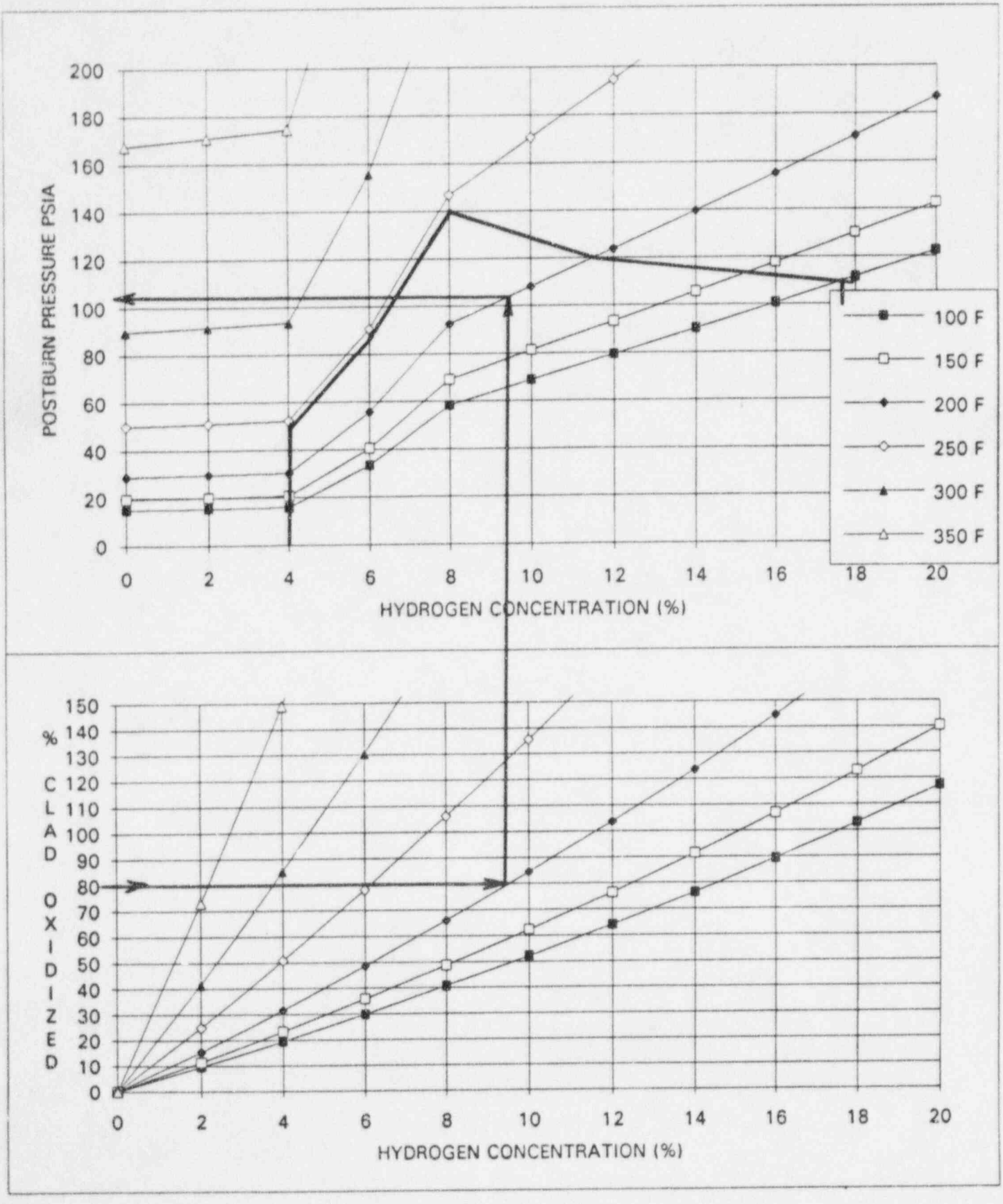

Figure C-4: Hydrogen Burn Map for Saturated Conditions — Local Burns

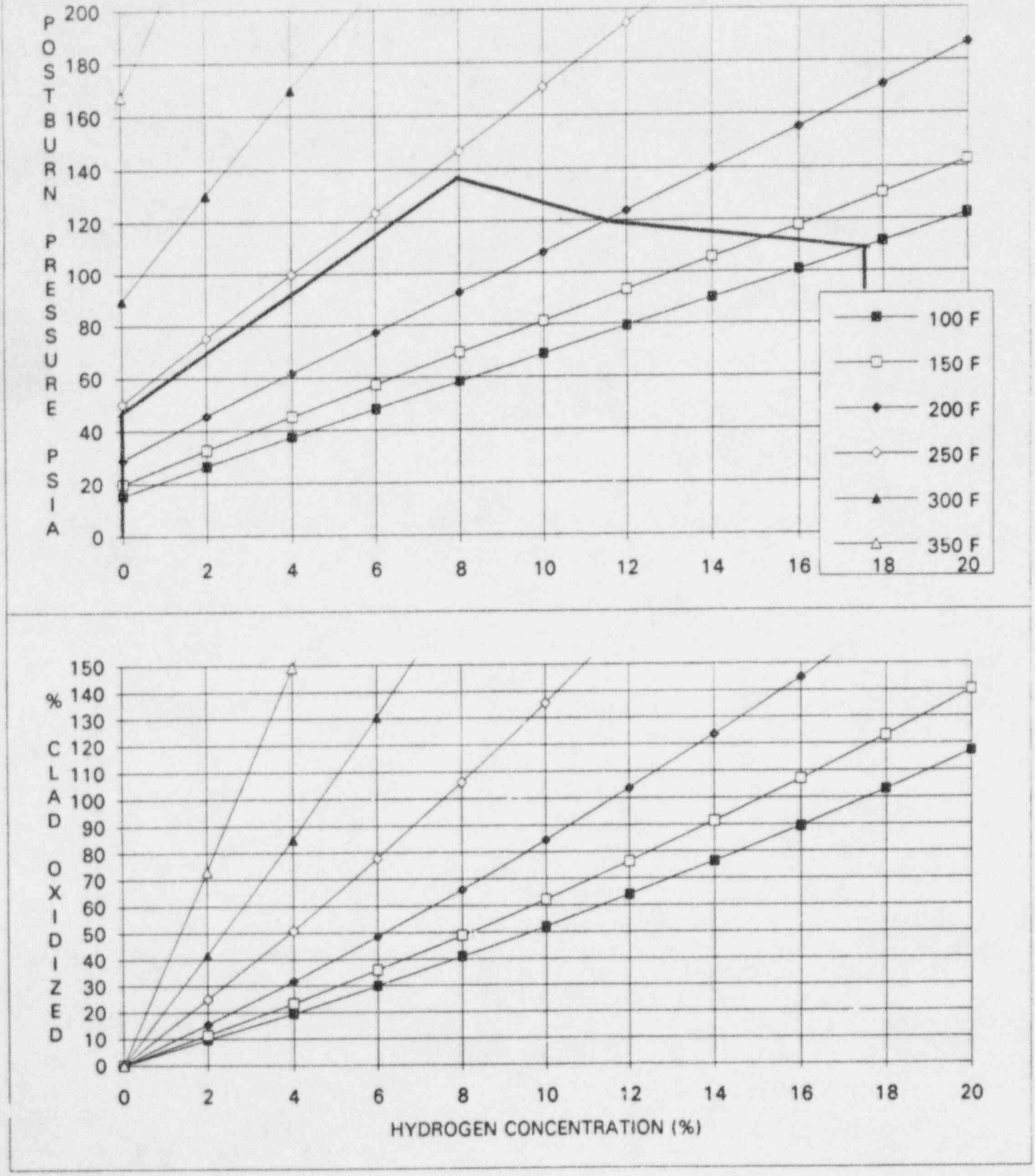

Figure C-5: Flammability of Hydrogen-Steam Discharges into Air-Steam Mixtures (From Reference C-3)

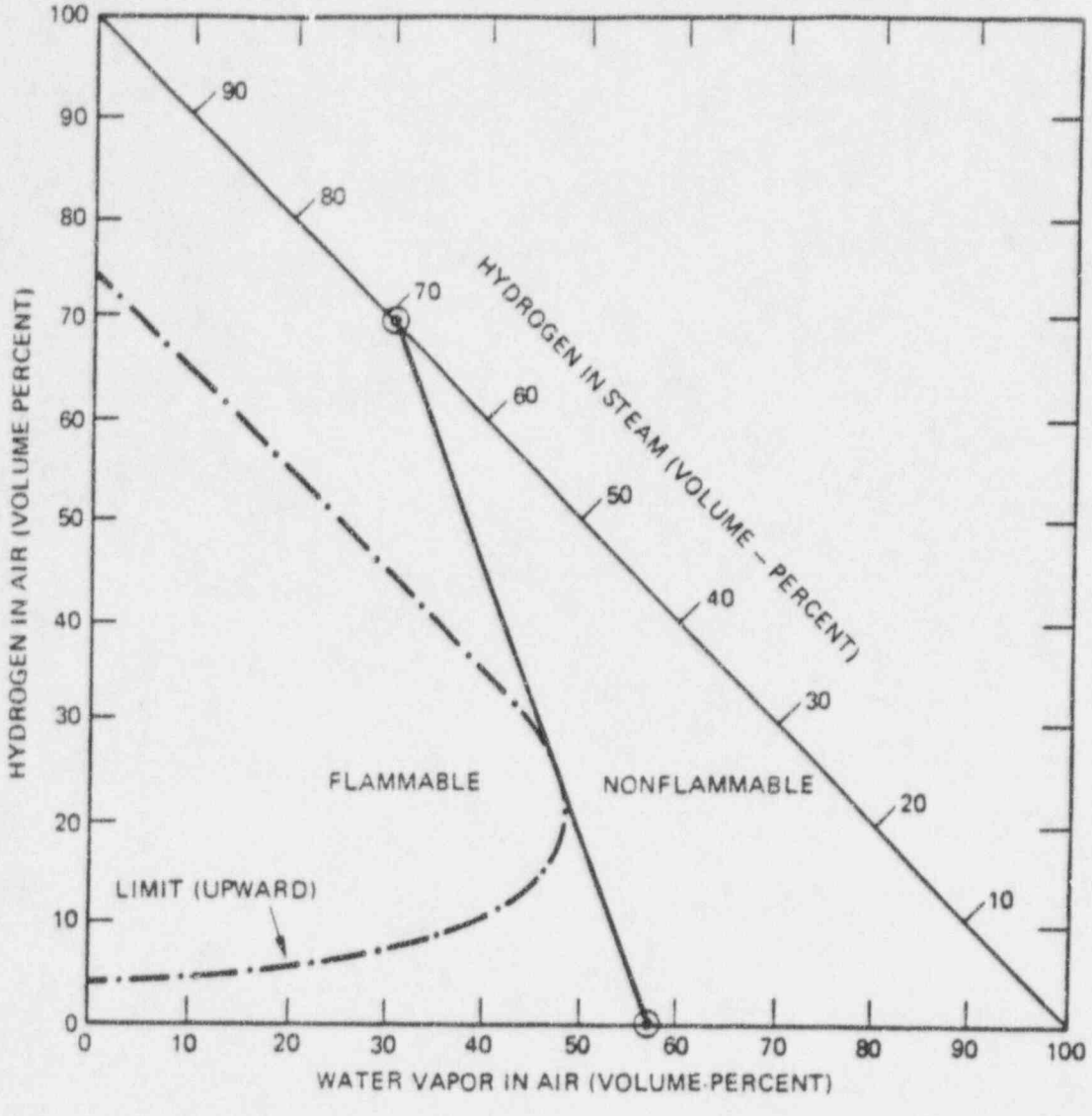

- STEAM CONCENTRATION IN CONTAINMENT: $X_{H_2O} = 0.57$
- MINIMUM FLAMMABLE HYDROGEN CONCENTRATION IN DISCHARGE: $X^{MIN}_{H_2,D} = 0.7$

APPENDIX D

RCS FAILURE MODES AT HIGH PRESSURE

D.1 Introduction

Accident sequences in which the RCS pressure remains high until vessel melt-through can lead to natural convection heat transport within the reactor vessel and RCS. High wall temperatures and high pressures can lead to creep deformations and possibly creep rupture of the pressure boundary. Therefore, it is necessary to address the vessel failure mode and the subsequent containment response to assess the risk associated with pressurized sequences.

Three basic RCS failure modes have been identified for high RCS pressure conditions. All are related to the combination of high pressure and high temperatures that may occur in the RCS after core uncovery starts. The three potential failure location and failure modes are:

1. Thermal creep failure of the RCS hot leg or pressurizer surge line.
2. Thermal creep failure of the steam generator tubes.
3. Vessel melt-through failure by molten debris attack of the in-core instrument penetrations.

Thermal creep failure of the RCS hot leg and/or pressurizer surge line are a concern only for high RCS pressure conditions. A high RCS pressure promotes natural circulation in the vessel, hot leg, and steam generator when the temperature begins to increase after core uncovery. The transient analyses in Section 4.6 predict that the hot leg can reach temperature levels of 1250 °F before vessel breach. It is to be determined whether creep rupture could occur at the calculated temperature in the time that the high temperature condition exists before vessel melt-through.

The CR-3 hot legs and surge line are made of carbon steel, which has a lower temperature threshold for creep rupture than either stainless steel or Inconel. Creep rupture of the hot leg or surge line will be controlled by hoop stresses that are expected to yield a failure area of a size that results in rapid RCS depressurization. If depressurization does not occur rapidly due to the size of the initial leak area, the flow of hot gases through the initial rupture would quickly cause local heating of the rupture area and further promote an increasing creep rupture area. Therefore, if hot leg or surge line creep rupture is predicted to occur first, the RCS will depressurize quickly, resulting in low RCS pressure at vessel melt-through.

Creep rupture of one or more steam generator tubes is also a possibility at high RCS pressure. Although less likely because the steam generator tubes are farther from the core, the tube geometry

is less conductive to natural circulation, and the tube materials have a higher resistance to creep rupture than the hot leg piping. Rupture of steam generator tubes would be an undesirable event because it would create a potential for a containment bypass release path if the RCS is not depressurized and if the faulted steam generator safety valve opened or if the atmospheric relief valve on the faulted steam generator is open.

The RCS vessel is assumed to eventually fail by bottom head vessel melt-through in all unmitigated core melt accidents. If this failure mode occurs at high pressure, there is a possibility of an early containment failure should the core debris be ejected from the vessel at high pressure, be finely fragmented, and cause direct heating of the containment atmosphere by the debris and exothermic chemical reactions. The driving force for debris dispersal and direct heating is reduced if one of the RCS failure modes discussed above occurs and depressurizes the RCS before the time of vessel melt-through. Similarly, if the operator depressurizes the RCS by opening the PORVs, the RCS pressure at vessel melt-through would be so low that the concern about a steam generator tube creep rupture could be eliminated and the concern about direct heating could be substantially reduced.

D.2 Creep Rupture Failure

Creep rupture of ductile materials is described by three parameters: time, temperature, and stress. For PWR hot legs and steam generator tubes, creep rupture data were compiled and published in the NUREG-1150 draft report (Reference D-1). Figure D-1 is reproduced from the NUREG-1150 draft document. It shows the creep rupture time for the carbon steel hot legs at Surry as a function of temperature and RCS pressure. The hot leg material at CR-3 is also carbon steel, and the thickness to diameter (t/D) ratio which governs the hoop stress is very similar. For the Surry hot legs, t/D = 0.086, whereas for CR-3, t/D = 0.080. Therefore, the Surry curves in Figure D-1 can be used to evaluate hotleg creep rupture at CR-3.

The steam generator tubes at CR-3 are made of an Inconel type Ni-Cr-Fe alloy. Figure D-2, also taken from Reference D-1, shows the creep rupture characteristics of Inconel, which can be used to evaluate creep rupture of the steam generator tubes at CR-3. It is seen from a comparison of Figures D-1 and D-2, that Inconel is considerably more resistant to creep rupture than carbon steel. In the CR-3 design, the steam generators form a cold well in the primary system loop, and therefore, the tubes will always be much colder than the hot legs. With lower temperatures and a higher creep rupture resistance, creep rupture of a steam generator tube in a B&W design will always be much

less likely than rupture of the hot leg or surge line. This conclusion was also reached in Reference D-2 for a Westinghouse design PWR, and it is even more strongly the case for a B&W PWR design.

Figures D-1 and D-2 will be used to evaluate creep rupture phenomena in Section 4.7.

D.3 Vessel Failure Mode with Depressurized RCS

Depressurization of the RCS leads to a significant reduction in heat transport from the reactor vessel to the hot legs and steam generator. Therefore, the probability of hot leg failure would be significantly reduced. Since hot leg failure would be a desirable RCS failure mode and since at low pressure it would be less likely than vessel melt-through, all sequences with the RCS depressurized are modeled to proceed to vessel melt-through.

References for Appendix D

D-1 "Reactor Risk Reference Document", NUREG-1150, Volume 3, Appendix J, February 1987.

D-2 "Risk Management Actions to Assure Containment Effectiveness at Seabrook Station", PLG-0550, July 1987.

Figure D-1: Average wall temperature versus rupture time for hot leg nozzle (A-508, Class 2 carbon steel) (From Reference D-1)

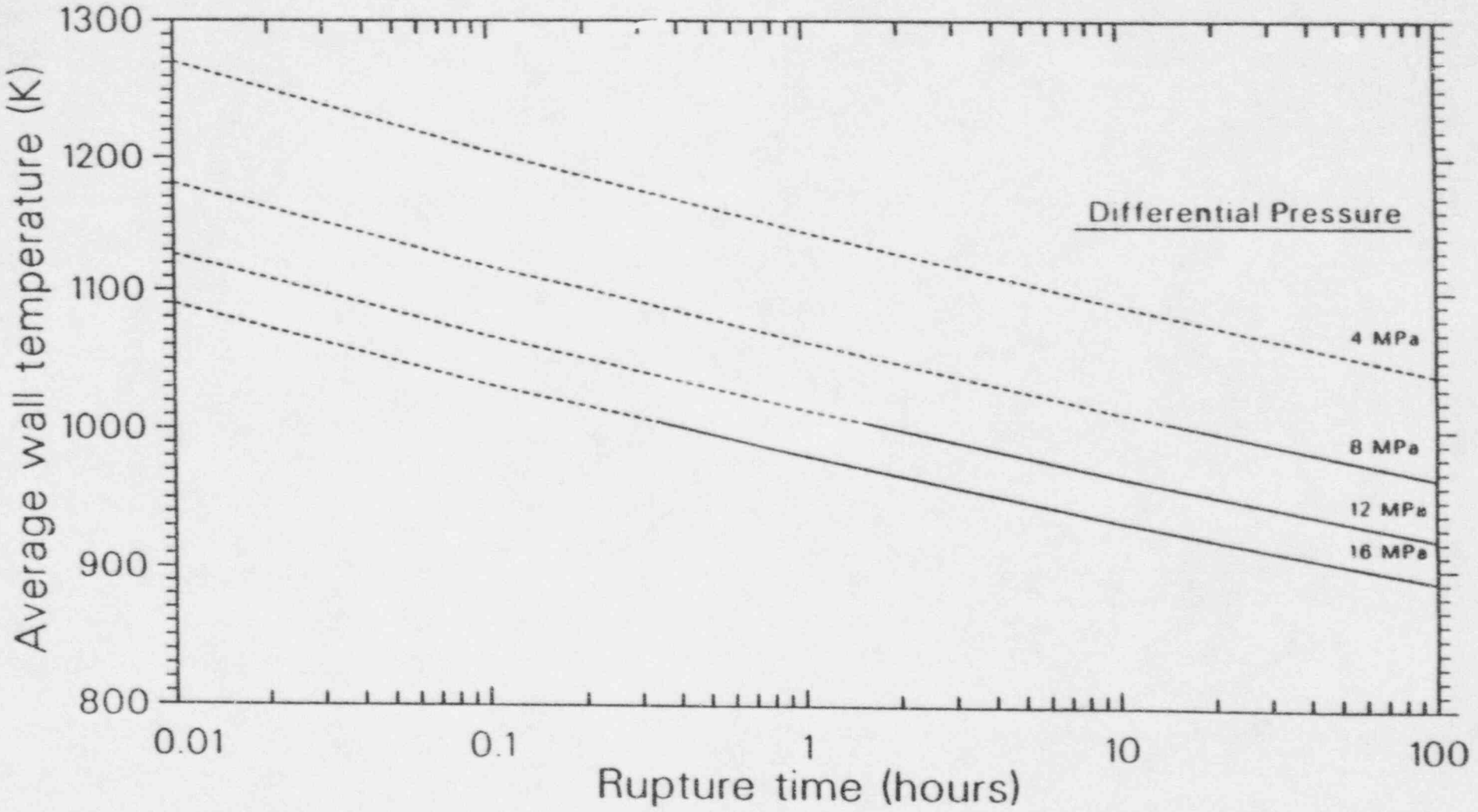

Note Phase change occurs at about 1005 K (1350 °F). Calculated rupture times above this temperature (indicated by dashed lines) may not be valid.

Figure D-2: Average wall temeprature versus rupture time for steam generator tube (Inconel 600) (From Reference D-1)

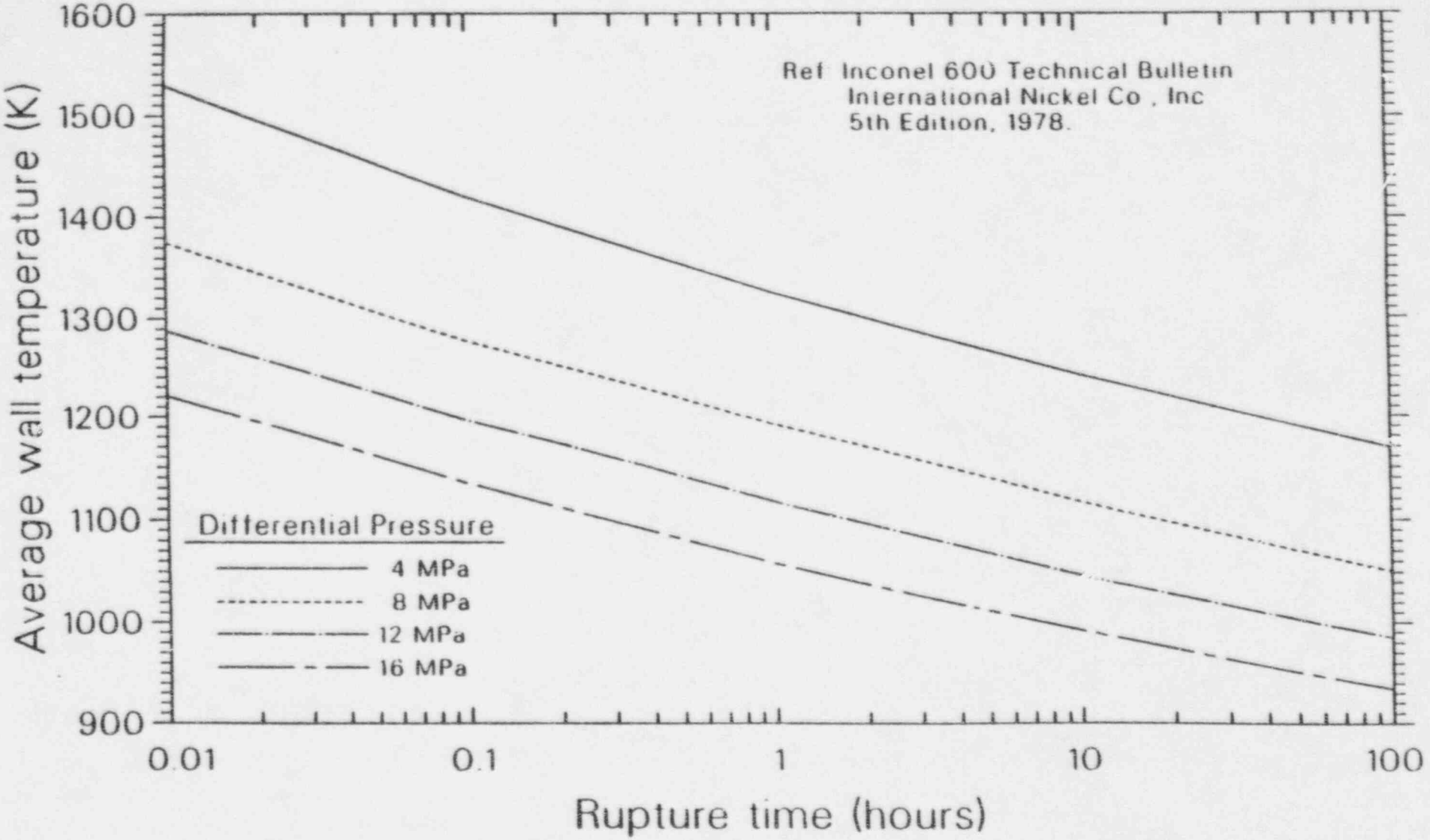

APPENDIX E

STRESS-STRENGTH INTERFERENCE ANALYSIS OF CONTAINMENT FAILURE PROBABILITY

Containment failure probabilities are calculated using a stress-strength interference method. This method is illustrated in this appendix, using fictitious split fraction FSX as an example. The uncertainty distribution for the containment pressure due to a direct containment heating event with the default hydrogen burn model from Appendix F is used to determine the split fraction value of FSX. The pressure load from a DCH event with the default hydrogen burn model (DEFHB) from Appendix F is used for the example. It is characterized by a median pressure of 82 psia and a 95 percentile pressure of 106 psia. This is interpreted as a lognormal distribution, which yields a lognormal standard deviation of 0.156. This distribution, which defines the containment load, is shown as the curve labelled "Load DEFHB" in Figure E-1.

The curve labelled "Capacity" in Figure E-1 is the composite (total) containment failure distribution curve in Figure 4.4-1. This curve defines the containment strength.

The probability of containment failure is defined as the probability that the containment load exceeds the containment strength. Since the uncertainty distribution for the containment load is independent of the distribution for the containment strength, the containment failure probability is defined by the stress-strength interference integral:

$$Pr\ (\text{Containment Failure}) = \int_0^{\infty} Pr\left(P_c = p\right) \left[\int_0^{p} Pr\left(P_f = p'\right) dp'\right] dp$$

where: P_c is the peak containment pressure (load), and

P_f is the containment failure pressure (capacity).

The expression inside the brackets is the cumulative composite probability distribution for total containment failure $CPr\ (P_f < p)$, which is shown in Figure 4.4-2.

Performing the integration for the two curves in Figure E-1 yields the probability of containment failure, FSX = 0.018, which is given in Appendix F.

Figure E-1: Stress-Strength Interference of Containment Load and Capacity

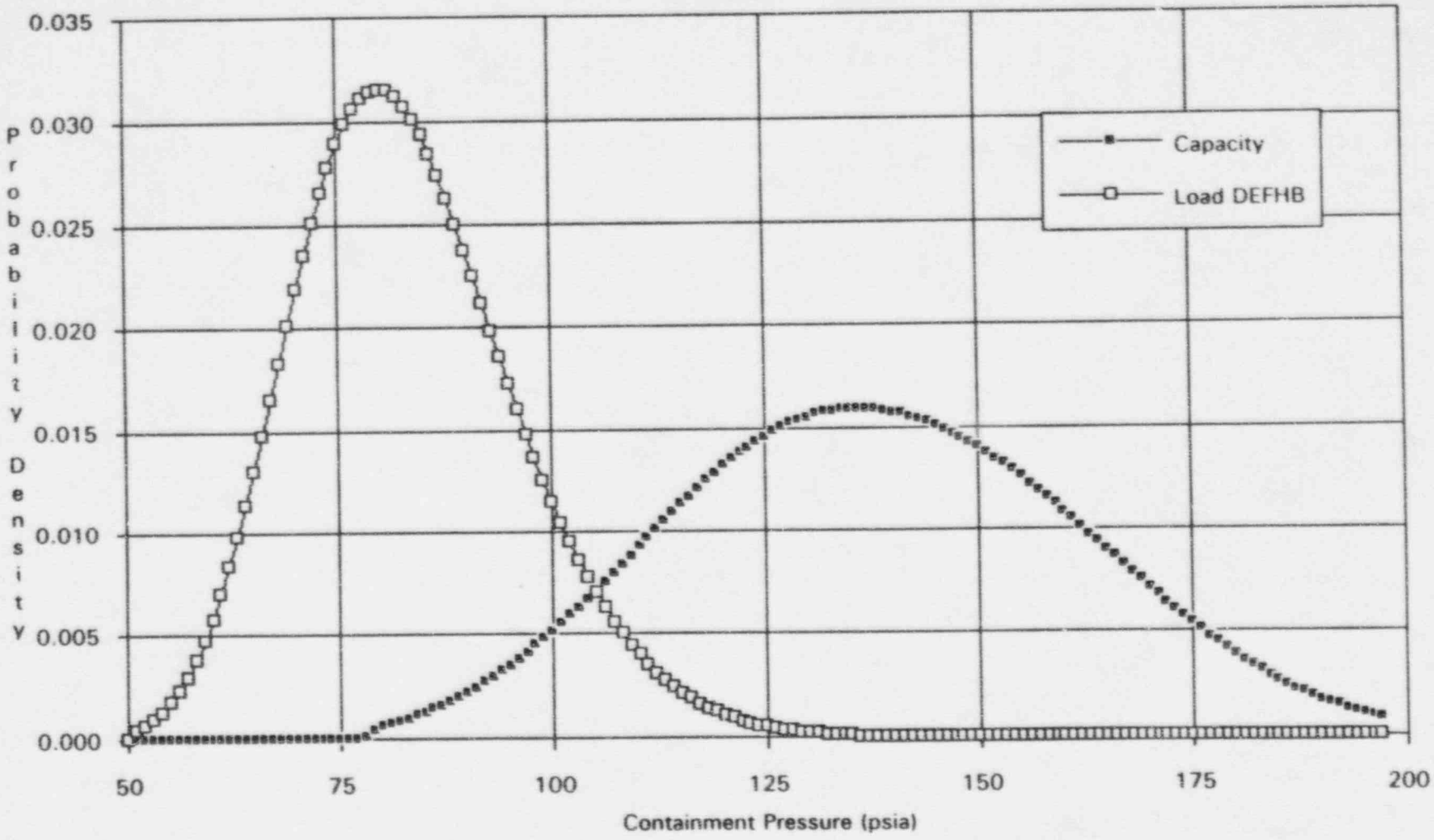

APPENDIX F

DIRECT CONTAINMENT HEATING AND

CONTAINMENT INTEGRITY AT RCS FAILURE

F.1 Background

High pressure accident sequences can involve a series of physical processes at the time of vessel breach that may affect the magnitude of the containment pressure rise. In a large dry PWR, the blowdown of the primary system gases at high pressure and temperature can cause the containment pressure to increase to about 60 to 80 psia, without the action of any other mechanisms that can increase containment pressure. This pressure level is not sufficient to challenge the integrity of the containment. However, the integrity of the containment at the time of vessel breach can be challenged by a number of other physical processes which may or may not occur simultaneously with the blowdown pressure rise and which may result in an incremental pressure increase whose magnitude can not be predicted with a high degree of certainty. Three physical processes have been identified that can increase the pressure rise at vessel breach. These are:

a) A hydrogen burn
b) Direct containment heating
c) Rapid steam generation from debris quenching

The effect of hydrogen burns on the containment pressure is discussed in Appendix C. The effect of debris quenching in the containment is an integral part of the accident progression analysis, and therefore does not need to be addressed separately.

Direct Containment Heating (DCH) postulates that the core debris is forcefully ejected from the reactor vessel due to the high RCS pressure and that the debris is finely fragmented allowing a significant portion of the sensible heat in the debris to be transferred directly to the containment atmosphere. It is further postulated that certain metals in the hot debris can be oxidized by the steam and oxygen in the air releasing additional exothermic reaction energy, generating additional hydrogen and rendering certain fission products, which are more volatile in the oxidized form, airborne. Furthermore, the hot debris particles can act as a distributed ignition source, causing the hydrogen in the containment atmosphere to recombine at any concentration.

Conclusive results for assessing the impact of direct containment heating, which would generically resolve the issue, have not been published to date. The Industry Degraded Core Rulemaking (IDCOR) program assessment of direct containment heating has concluded that there is no significant potential for direct transfer of debris sensible heat to the containment atmosphere. This is principally

because debris transport from the reactor cavity to the lower compartment is not believed to involve a fragmentation and entrainment mechanism which would yield small diameter particles.

The most recent information from the NRC-sponsored research on DCH is contained in References F-1 and F-2. A semi-mechanistic, dynamic model for direct heat transfer between the debris and the gas phase was incorporated into the CONTAIN code. This code is known as CONTAIN-DCH, Version 1.0. In this model, some of the less well-understood phenomena are treated parametrically. Reference F-1 includes some 50 separate sensitivity calculations, for a five node model of the Surry containment, which are documented in Tables 3.3 and 3.4 of Reference F-1. These results show a significant reduction in the maximum containment pressure compared to the early estimates, which were based on nonmechanistic equilibrium calculations. The maximum containment pressure calculated in Reference F-1 is 178 psia, whereas the base case yielded a containment pressure of 102 psia.

More recent calculations were performed in support of the revision to the NUREG-1150 analyses. These calculations also used the CONTAIN code, but with an 18-node containment model. These results were presented to the expert panels, and they are to be published as part of the NUREG/CR-4551 reports which evaluate severe accident risks on potential risk reductions at several representative plants. Extensive comparisons and additional insights are not available at this time, except that the more detailed containment models result in a further decrease in the peak containment pressure by typically 5 to 15 psi.

In a more recent report from the Brookhaven National Laboratory (Reference F-2), results of DCH calculations also using Version 1.0 of the CONTAIN-DCH code for the Zion PWR are presented. These analyses showed somewhat higher peak pressures compared to the results of Reference F-1. Both sets of results are analyzed in the following sections. In the absence of plant-specific DCH calculations for CR-3, the results of References F-1 and F-2 will be interpreted for CR-3 and applied.

F.2 DCH Analysis

The approach used to define the magnitude and uncertainties in the containment pressure at CR-3 after a high pressure vessel melt-through was to consider the most recent information publicly available from other sources and to interpret this information for the CR-3 containment

configuration. Equal weight (probability) was assigned to the calculations and to the adaptation of the results from the NRC-sponsored research in References F-1 and F-2.

The physical parameters which can be expected to have the most significant influence on the containment pressure after vessel breach are the free containment volume, the core mass and the RCS volume, whereby a large containment volume, a small core mass and a small RCS volume would be expected to reduce the DCH pressure peak. The Surry, Zion and CR-3 values for these parameters are listed below. It is seen that the values for CR-3 are intermediate to those for Surry and Zion. Therefore, at first glance, the DCH behavior at CR-3 could also be expected to be bracketed by the calculations for Surry and Zion.

Parameter	Surry	Zion	CR-3
Containment Free Volume (Mcft)	1.8	2.6	2.0
Core UO2 Mass (1000 kg)	80	100	93
Core Zr Mass (1000 kg)	16.5	21.6	19.1
RCS Volume (Kcft)	9.8	13.7	11.5

Both references consider cases where the CONTAIN default hydrogen burn model is used and cases where the unconditional hydrogen burn model is used. The default model requires that the ignition criteria with respect to the concentration of hydrogen, oxygen and inerting diluents like steam are satisfied before a hydrogen burn can occur. This hydrogen burn model is appropriate if the containment atmosphere temperature is below the auto-ignition temperature for hydrogen. Hypergolic recombination, i.e., spontaneous recombination without regard to the concentrations of hydrogen, oxygen, and steam, can occur at temperatures above about 1,000 °F at low steam concentrations. The auto-ignition temperature increases to about 2,000 °F at very high steam concentrations. Due to the direct heating of the containment atmosphere by the debris in a DCH event, the temperature threshold for auto-ignition is readily exceeded for at least a portion of the containment atmosphere. The unconditional hydrogen burn model assumes that there are no ignition limits, and that all the hydrogen is recombined, limited only by the availability of oxygen.

Table F-1 lists all the "full debris" cases with the unconditional hydrogen burn model from References F-1 and F-2. There are 19 such cases for Surry and 14 cases for Zion. These 33 cases were considered to establish a probability distribution for the peak containment pressure at CR-3 given a DCH event with an unconditional hydrogen burn. The columns from left to right identify the case number, the case identifier, the case probability weight, the calculated peak pressure in bar and psia, a case correction, the corrected peak pressure applied to CR-3 in psia, and the fraction of the core and other debris structures allowed to participate in the DCH event. The Surry cases from NUREG/CR-4896 (Reference F-1) are identified as Surry Tx.y #z, where x.y is the table number and z is the case number from Reference F-1. The discrete probabilities are distributed to all the cases such that all the Surry cases add up to 0.5. The case correction is based on information contained in the References. The results in NUREG/CR-4896 for Surry were adapted to CR-3 using the following corrections discussed in Reference F-1.

Cause	Change in Peak Pressure Rise
E - Error Fix	-0.2 bar
Modak Emissivities	-0.2 bar
5 Node to 18-Node CONTAIN Model (Surry)	-0.5 bar
7 Node to 18 Node CONTAIN Model (Zion, estimate)	-0.4 bar

The top two corrections were identified in Reference F-1. These corrections were applied to the appropriate cases in Tables 3.3 and 3.4 of Reference F-1. Care was taken not to double count corrected cases. The last correction has been applied to all cases. This resulted in the 19 corrected full debris cases with an unconditional hydrogen burn listed in the top portion of Table F-1. In these cases, the maximum amount of debris considered is ejected and participates in the DCH process. In the Surry calculations, this maximum amount of debris is 75% of a fully melted core and lower internals. The containment pressures calculated for these cases ranges from 119 psia to 174 psia. Based on Reference F-1, Case 4 was identified as the base case, and it was assigned twice the weight of all the other cases. The total probability of all the Surry cases in Table F-1 is 0.5.

Fourteen Zion cases with an unconditional hydrogen burn and with the maximum amount of debris is involved in the DCH process are documented in NUREG/CR-5282. These cases are listed in the second block in Table F-1 (cases 20 to 33). They are identified as Zion A-#, where the # designates the case number from Reference F-2. In all the Zion cases, 100% of the core and lower internals is assumed to participate in the DCH process. Only the last correction listed above was applied to the Zion cases, since the first two corrections had already been applied to all case calculations. The estimated correction for the limitations of a 7-Node CONTAIN model was based on the corresponding correction for Surry, because no Zion calculations with a detailed CONTAIN noding scheme were documented. The containment pressures for these Zion cases range from 136 psia to 207 psia. Based on Reference F-2, case 20 was identified as the base case and was assigned twice the weight of all the other cases. The total probability of all the Zion cases in Table F-1 is 0.5.

The amount of debris participation in the DCH process is one of the largest uncertainties regarding the effects of DCH. In each reference, some calculations were performed with only a fraction of the maximum debris amount participating in the DCH process. The results of these cases are shown in Figure F-1. The upper three curves represent unconditional hydrogen burn (UCHB) cases, and the lowest curve applies to default hydrogen burn (DEFHB) cases. Also marked are the only two Zion cases for default hydrogen burns at 100% debris involvement. It is seen that when plotted against the debris mass fraction participating in the DCH process, the differences between the Surry calculation and the Zion calculation for the UCHB cases are not large, and for the default hydrogen burn model, the Surry curve extrapolates to in-between the two Zion cases at 100% debris participation. On the basis of Figure F-1, the behavior for CR-3 is represented as the average between the Surry and the Zion results. This is indicated by the curves labelled CR-3 on Figure F-1. The CR-3 UCHB curve is incorporated into the first three lines in the top header of Table F-1. The base pressure in the first line is the pressure with zero debris involvement in DCH. The second line represents the points on the CR-3 UCHB curve at 25%, 50%, 75% and 100% debris DCH involvement, as indicated on the third line. The results on the left side of Table F-1 were scaled to these four discrete DCH debris involvement fractions in order to cover more realistically the range of debris involvement given a DCH event. A zero debris fraction is not included, because that would be the "No DCH" case which is treated separately. The scaling was performed on the basis of the CR-3 UCHB curve in Figure F-1, and the results are shown on the right side of Table F-1 as the peak DCH pressure in psia. The resulting probability distribution is shown in Figure F-2 as the curve labelled "Unconditional Burn".

The exact same procedure is applied to develop the peak DCH pressure for the default hydrogen burn condition. The cases and results are shown in Table F-2. The range of containment pressures calculated by CONTAIN for the default burn cases ranges from 87 psia to 138 psia for the Surry cases and from 107 psia to 113 psia for the two Zion cases. The scaling to the four discrete DCH debris involvement fractions is based on the curve labelled CR-3-DEFHB in Figure F-1. The resulting probability distribution for the peak DCH pressure is shown in Figure F-2 as the curve labelled "Default Burn". The "Default Burn" curve shows a significantly lower peak pressure than the "Unconditional Burn" curve, because at the time of vessel breach in a station blackout sequence, the containment is steam inerted, and no hydrogen burn occurs with the "Default Burn" model.

F.3 Containment Failure Due to DCH

The probability distribution for the containment pressure after vessel breach given a DCH event is defined by the two curves in Figure F-2. These curves define the probability that the actual containment pressure following a DCH event at vessel breach in a station blackout accident sequence would be less than indicated by the X-axis pressure value. These curves are approximated by a log-normal distribution with the following characteristics:

Case	Unconditional Hydrogen Burn	Default Hydrogen Burn
Median pressure	116 psia	82 psia
5th percentile	97 psia	72 psia
95th percentile	153 psia	106 psia
Range factor	1.26	1.21

The probability that containment failure occurs due to DCH at the time of vessel breach is determined by the probability that the containment failure pressure is lower than the containment pressure load as described in Appendix E. Convolution of the curves in Figure F-2, with the composite containment failure distributions shown in Figure 4.4-5, according to the stress-strength interference integral yields the probability of containment failure given DCH as follows:

Case	Failure Probability
Containment failure given DCH, default hydrogen burn	0.018
Containment failure given DCH, unconditional hydrogen burn	0.252

These split fractions apply to high pressure vessel melt-through conditions, i.e., station blackout sequences without depressurization. In the CET quantification, these split fraction values have been used at the appropriate branching points. These analyses indicate that for high pressure core melt sequences where neither RCS depressurization nor hot leg creep rupture occurs before vessel breach, the Direct Containment Heating phenomena, if it occurs, would cause the containment to fail with a 25% probability if the containment temperature is sufficiently hot to support autoignition, and with a probability of 1.8% otherwise.

References for Appendix F

F-1 Williams, D. C., et al.,"Containment Loads due to Direct Containment Heating and Associated Hydrogen Behavior: Analysis and Calculations with the CONTAIN Code," Sandia National Laboratory, NUREG/CR-4896, 1987.

F-2 Tutu, N. K., et. al., "Estimation of Containment Pressure Loading Due to Direct Containment Heating for the Zion Plant", Brookhaven National Laboratory, NUREG/CR-5282, March 1991.

Table F-1: Containment Pressure Due to Direct Containment Heating with Unconditional Hydrogen Burn

						Base Pressure, Po (Psia)	84	84	84	84
						P-CR3 Model (psi)	133	125.50	113	98.5
						Debris Fraction	1	0.75	0.5	0.25
						Probability	0.05	0.2	0.5	0.25
	Case	Discrete Probability	NUREG-4896 NUREG-5282 (Bar)	Surry Zion (Psia)	Case Correction (Bar)	Corrected Pressure (Bar)	Ejected Debris Fraction	Peak DCH Pressure (Psia)			
1	Surry T3.3 #8	0.025	9.8	142.1	0.9	8.9	0.75	137.19	129.05	115.48	99.74
2	Surry T3.3 #9	0.025	8.8	127.6	0.9	7.9	0.75	120.07	114.55	105.35	94.67
3	Surry T3.3 #10	0.025	8.4	121.8	0.9	7.5	0.75	113.22	108.75	101.30	92.65
4	Surry T3.3 #11	0.050	9.1	131.95	0.7	8.4	0.75	128.63	121.80	110.41	97.21
5	Surry T3.3 #12	0.025	9.3	134.85	0.9	8.4	0.75	128.63	121.80	110.41	97.21
6	Surry T3.3 #13	0.025	9.6	139.2	0.9	8.7	0.75	133.77	126.15	113.45	98.73
7	Surry T3.3 #15	0.025	9	130.5	0.9	8.1	0.75	123.50	117.45	107.37	95.69
8	Surry T3.3 #17	0.025	12.3	178.35	0.9	11.4	0.75	179.99	165.30	140.81	112.41
9	Surry T3.3 #19	0.025	11.6	168.2	0.9	10.7	0.75	168.01	155.15	133.72	108.86
10	Surry T3.3 #24	0.025	9.5	137.75	0.9	8.6	0.75	132.06	124.70	112.44	98.22
11	Surry T3.3 #25	0.025	9.1	131.95	0.9	8.2	0.75	125.21	118.90	108.39	96.19
12	Surry T3.4 #11	0.025	11.1	160.95	0.5	10.6	0.75	166.30	153.70	132.71	108.35
13	Surry T3.4 #12	0.025	8.9	129.05	0.5	8.4	0.75	128.63	121.80	110.41	97.21
14	Surry T3.4 #13	0.025	9.9	143.55	0.5	9.4	0.75	145.75	136.30	120.55	102.27
15	Surry T3.4 #14	0.025	10.5	152.25	0.5	10	0.75	156.02	145.00	126.63	105.31
16	Surry T3.4 #15	0.025	8.2	118.9	0.5	7.7	0.75	116.65	111.65	103.32	93.66
17	Surry T3.4 #16	0.025	8.7	126.15	0.5	8.2	0.75	125.21	118.90	108.39	96.19
18	Surry T3.4 #17	0.025	10.9	158.05	0.5	10.4	0.75	162.87	150.80	130.68	107.34
19	Surry T3.4 #18	0.025	9.1	131.95	0.5	8.6	0.75	132.06	124.70	112.44	98.22
20	Zion A-1	0.067	9.9	143.55	0.4	9.5	1	137.75	129.52	115.81	99.91
21	Zion A-2	0.033	11.3	163.85	0.4	10.9	1	158.05	146.72	127.83	105.91
22	Zion A-3	0.033	10.4	150.8	0.4	10	1	145.00	135.66	120.10	102.05
23	Zion A-6	0.033	9.7	140.65	0.4	9.3	1	134.85	127.07	114.09	99.05
24	Zion A-7	0.033	9.6	139.2	0.4	9.2	1	133.40	125.84	113.24	98.62
25	Zion A-8	0.033	10.1	146.45	0.4	9.7	1	140.65	131.98	117.53	100.76
26	Zion A-11	0.033	10.1	146.45	0.4	9.7	1	140.65	131.98	117.53	100.76
27	Zion A-13	0.033	14.3	207.35	0.4	13.9	1	201.55	183.56	153.57	118.79
28	Zion A-13a	0.033	10.8	156.6	0.4	10.4	1	150.80	140.58	123.53	103.77
29	Zion A-13b	0.033	10.8	156.6	0.4	10.4	1	150.80	140.58	123.53	103.77
30	Zion A-14	0.033	13.7	198.65	0.4	13.3	1	192.85	176.19	148.42	116.21
31	Zion A-16	0.033	9.4	136.3	0.4	9	1	130.50	123.38	111.52	97.76
32	Zion A-20	0.033	12.9	187.05	0.4	12.5	1	181.25	166.36	141.56	112.78
33	Zion A-21	0.033	10.7	155.15	0.4	10.3	1	149.35	139.35	122.68	103.34

Table F-2: Containment Pressure Due to Direct Containment Heating with Default Hydrogen Burn Model

						Base Pressure, Po (Psia)	64.4	64.4	64.4	64.4
						P-CR3 Model (psi)	101.8	91.50	81.4	72.7
						Debris Fraction	1	0.75	0.5	0.25
						Probability	0.05	0.2	0.5	0.25
	Case	Discrete Probability	NUREG-4896 NUREG-5282 (Bar)	Surry Zion (Psia)	Case Correction (Bar)	Corrected Pressure (Bar)	Ejected Debris Fraction	Peak DCH Pressure (Psia)			
34	Surry T3.3 #2	0.025	7.9	114.55	0.9	7	0.75	115.60	101.50	87.67	75.76
35	Surry T3.3 #3	0.025	6.7	97.15	0.9	5.8	0.75	91.59	84.10	76.76	70.43
36	Surry T3.3 #4	0.025	6.4	92.8	0.9	5.5	0.75	85.58	79.75	74.03	69.10
37	Surry T3.3 #5	0.025	7.1	102.95	0.9	6.2	0.75	99.59	89.90	80.40	72.21
38	Surry T3.3 #6	0.050	7	101.5	0.7	6.3	0.75	101.59	91.35	81.31	72.65
39	Surry T3.3 #14	0.025	6.9	100.05	0.9	6	0.75	95.59	87.00	78.58	71.32
40	Surry T3.3 #16	0.025	9.5	137.75	0.9	8.6	0.75	147.62	124.70	102.23	82.87
41	Surry T3.3 #18	0.025	8.8	127.6	0.9	7.9	0.75	133.61	114.55	95.86	79.76
42	Surry T3.3 #20	0.025	7.2	104.4	0.9	6.3	0.75	101.59	91.35	81.31	72.65
43	Surry T3.3 #21	0.025	7.9	114.55	0.9	7	0.75	115.60	101.50	87.67	75.76
44	Surry T3.3 #22	0.025	7	101.5	0.9	6.1	0.75	97.59	88.45	79.49	71.77
45	Surry T3.3 #23	0.025	7.4	107.3	0.9	6.5	0.75	105.60	94.25	83.13	73.54
46	Surry T3.4 #3	0.025	7.2	104.4	0.5	6.7	0.75	109.60	97.15	84.94	74.43
47	Surry T3.4 #4	0.025	7.8	113.1	0.5	7.3	0.75	121.60	105.85	90.40	77.10
48	Surry T3.4 #5	0.025	6	87	0.5	5.5	0.75	85.58	79.75	74.03	69.10
49	Surry T3.4 #6	0.025	7.3	105.85	0.5	6.8	0.75	111.60	98.60	85.85	74.87
50	Surry T3.4 #7	0.025	8.4	121.8	0.5	7.9	0.75	133.61	114.55	95.86	79.76
51	Surry T3.4 #8	0.025	7.5	108.75	0.5	7	0.75	115.60	101.50	87.67	75.76
52	Surry T3.4 #9	0.025	8.4	121.8	0.5	7.9	0.75	133.61	114.55	95.86	79.76
53	Zion A-4	0.333	7.8	113.1	0.4	7.4	1	107.30	95.49	83.90	73.92
54	Zion A-5	0.167	7.4	107.3	0.4	7	1	101.50	91.28	81.26	72.63

Figure F-1: Containment Pressure as a function of Participating Debris Mass

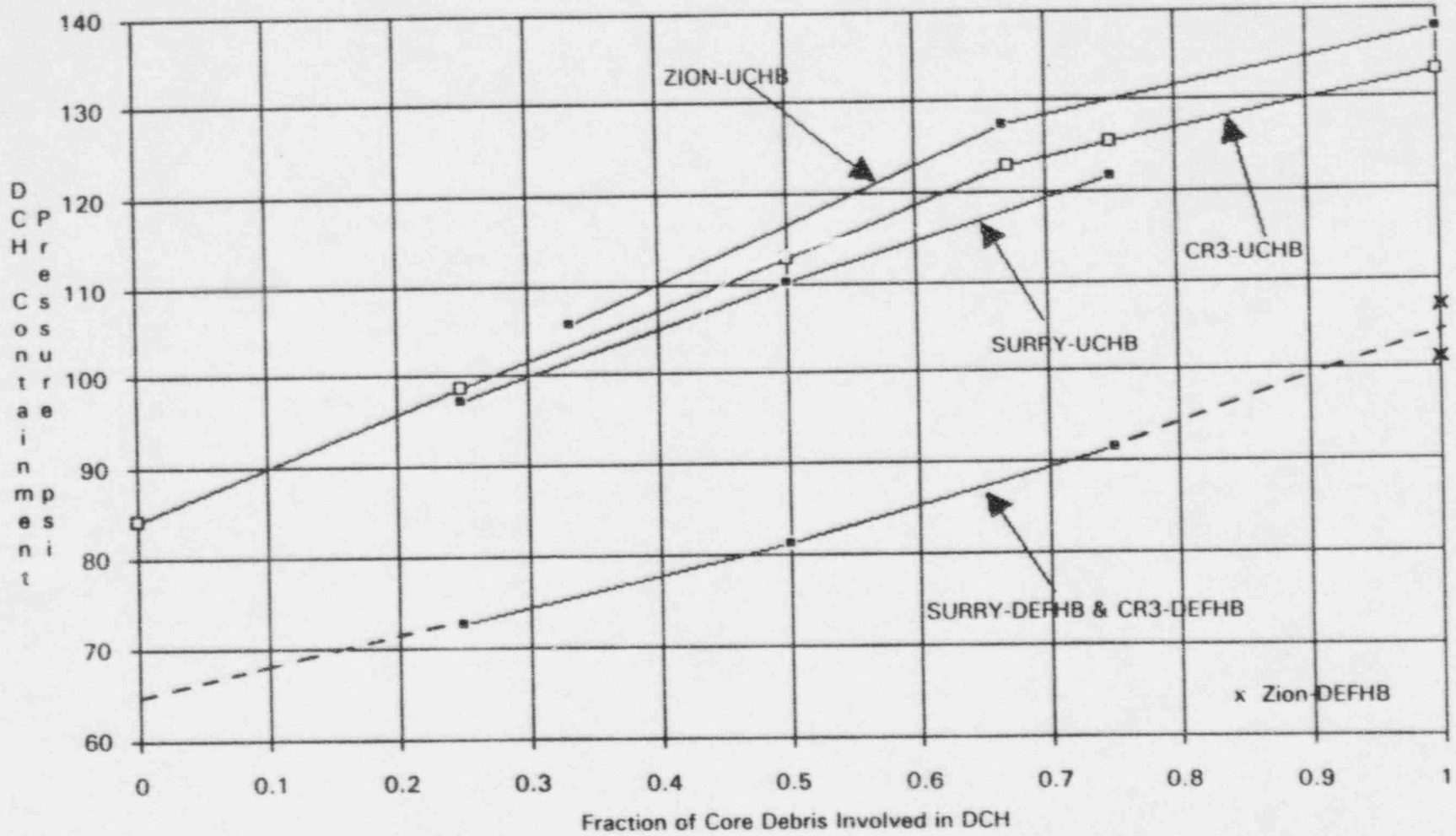

Figure F-2: Probability Distribution for Containment Pressure Due to DCH

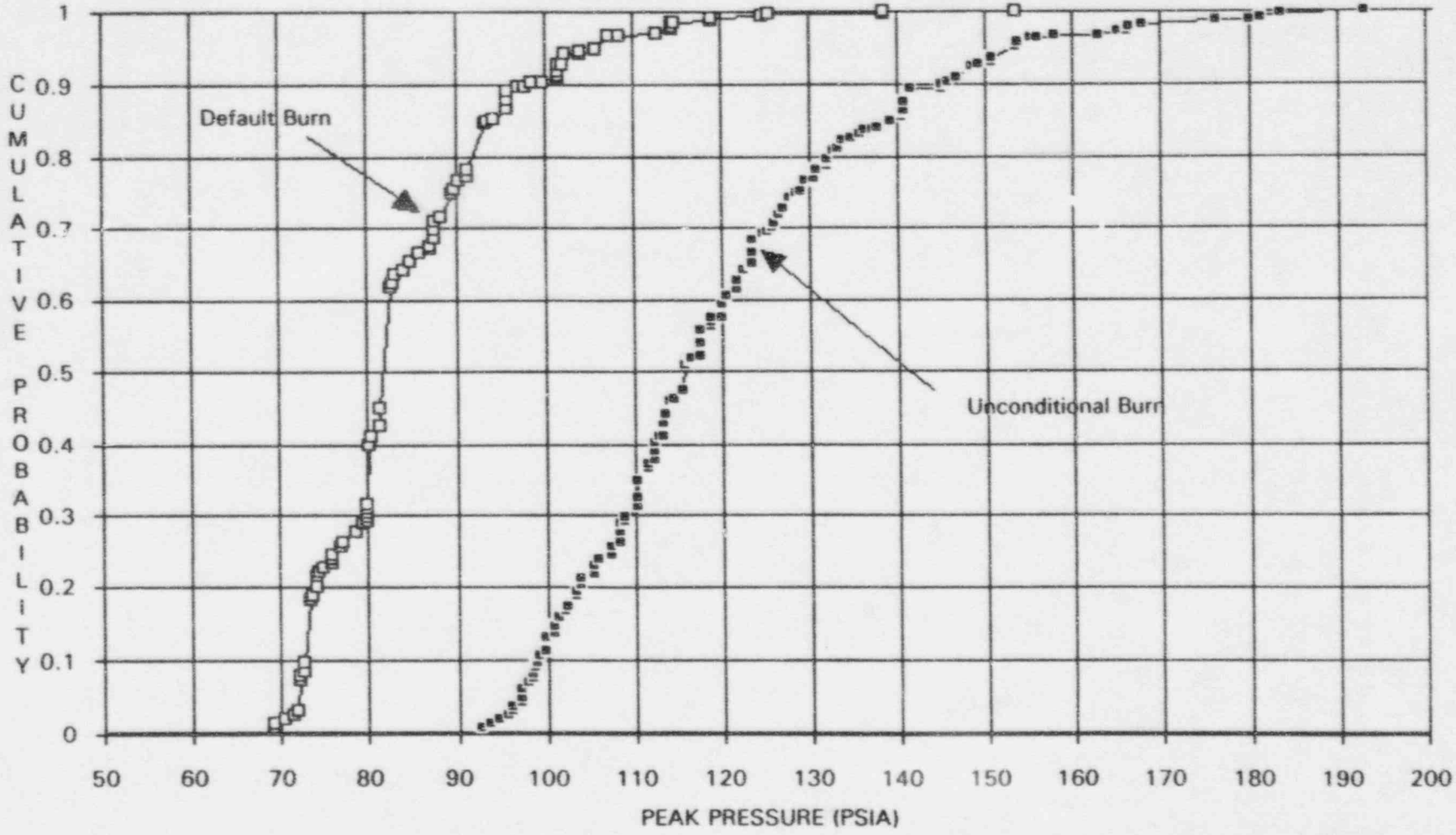

APPENDIX G

CONTAINMENT FAILURE DUE TO LATE HYDROGEN BURNING

This appendix documents the methodology for calculating the probability of containment failure due to late hydrogen burning. In the CPET, this is addressed in top event HD for late hydrogen burning and in top event FD for late containment failure. After vessel breach, the concentration of flammable gases increases due to the ex-vessel generation of hydrogen from the reaction of metallic elements in the debris and from the decomposition of calcium carbonate in the concrete which releases carbon monoxide (CO). According to the accident sequence analyses for accident sequences with continued basemat penetration, the concentration of carbon monoxide in the containment atmosphere steadily increases to levels comparable to the hydrogen concentration. Hydrogen and CO are very similar with respect to combustion effects. The molar heat of combustion of CO is about 15% lower, and the ignition limits and the inerting behavior is similar for the two gases. Therefore, to evaluate the effects of a late global burn, CO will be treated as hydrogen on a molar basis, and consequently, hydrogen and CO are of comparable importance for late combustion events.

The assessment of late containment failure due to hydrogen burns is based on the notion that the calculations of long term concentrations of hydrogen and CO, and to a lesser degree the steam concentrations, are subject to significant uncertainties. High concentrations of hydrogen are possible. For example, the concentration from the reaction of 100% zirconium in a saturated steam containment atmosphere is 15% at 150 °F, 12% at 200 °F, and 7.8% at 250 °F. At a temperature of 250 °F, a saturated containment atmosphere contains 57.5% steam, and therefore at higher temperatures, the containment would be steam inerted.

Table G-1 illustrates the method for calculating the split fractions for late containment failure due to a late hydrogen burn. In the first column, the range of combined hydrogen and CO concentrations in the containment is discretized for the specific accident condition, in this case represented by split fraction HDA. This condition applies to station blackout sequences where there has been no prior hydrogen burn. These sequences are without containment heat removal and the debris is not cooled. The second column lists the equivalent fraction of zirconium reacted, estimated from the total number of moles of H_2 and CO in the containment atmosphere, at the point in the accident sequence under consideration. This fraction can be greater than one due to the generation of CO. The third column lists the estimated probability based on the CONTAIN calculations that the long term hydrogen concentration would reach the indicated range in the absence of a hydrogen burn. For any given final concentration level, combustion can occur at the final level or at any of the preceding (lower) levels since the concentration has to build up through these levels to reach the final level. The fourth column lists the probability that the containment atmosphere is not steam inerted. The

fifth column indicates the probability that combustion does occur at any concentration and the next five columns distribute the total burn probability to the lower concentration ranges. The difference between the total burn probability and the sum of the burn probabilities at lower concentrations is then the probability of a burn at the final concentration level. The probability of a hydrogen burn in a given concentration range is shown in the next column. It is calculated as the sum of all contributions to burns at this concentration level, including those which otherwise would proceed to a higher concentration. The containment temperature, before the burn which is appropriate to the accident condition, is indicated in the column labelled "T-Before". The post-burn pressure is determined from Figure 4.7-1 or Figure D-2 and is listed in the column labelled "P-After". From Figures 4.4-2, 4.4-4 or 4.4-6, the probability of containment failure, given that a burn occurs, is listed in the next column. The figure which most closely corresponds to the preburn containment temperature listed in the column labelled "T-Before" is used. The second-to-last column lists the conditional probability of containment failure due to a hydrogen burn. It is the product of the burn probability and the containment failure probability given that a burn occurs. The last column finally gives the unconditional probability of a containment failure due to a hydrogen burn.

The different hydrogen concentration ranges are combined to determine the integral probabilities listed at the bottom of the table. The first of the three rows at the bottom correspond to the split fraction value HDx that a late hydrogen burn occurs. The middle row gives the unconditional probability of a late containment failure due to a burn, and the last row gives the conditional probability of a containment failure as a result of a late burn, given that a burn occurs. In Section 4.7, this methodology is applied for all split fractions for top event HD and for the corresponding split fractions in top event FD.

Table G-1: Methodology for Computing Containment Failure Due to a Late Burn

SPLIT FRACTION:		HDA			KPDS: K7D					No prior burn, debris not cooled				
X(H2 + CO) Conc (%)	Equival. % Zr-Oxidation	Prob of X(H2 + CO)	Prob not inerted	Total	PROBABILITY OF IGNITION <4%	4-6%	6-8%	8-10%	10-12%	Probability of Burn	T-Before (F)	P-After (PSIA)	Containment Failure CF|Burn	C FAIL
<4	<52	0	0.3	0						0.132	546	75	0	0
4-6	52-77	0	0.3	0.4	0.5					0.02895	546	90	0.020	5.8E-04
6-8	77-103	0.1	0.3	0.7	0.5	0.25				0.03195	546	135	0.523	1.7E-02
8-10	103-129	0.2	0.3	0.8	0.5	0.15	0.15			0.03585	546	174	0.953	3.4E-02
10-12	129-155	0.5	0.3	0.9	0.5	0.1	0.1	0.15		0.02625	546	197	0.996	2.6E-02
>12	>155	0.2	0.3	1	0.5	0.05	0.1	0.1	0.1	0.009	546	220	1	9.0E-03
		PROBABILITY OF LATE BURN =								0.2640	= HDA			
		PROBABILITY OF CONTAINMENT FAILURE =								0.0866				
		PROBABILITY OF CONTAINMENT FAILURE | LATE BURN =								0.3280				

APPENDIX H

CONTAINMENT PHENOMENOLOGICAL EVENT

TREE QUANTIFICATION

This appendix contains the details of the conditional CPET quantification in the form of a fully expanded CPET where the frequency at each branching point and at the end of each sequence is given. The CPETs are listed in the following order:

Figure H-1: CPET Quantification for KPDS K7D
Figure H-2: CPET Quantification for KPDS K7JH
Figure H-3: CPET Quantification for KPDS K6BA
Figure H-4: CPET Quantification for KPDS K4K
Figure H-5: CPET Quantification for KPDS K3BA

The numbers listed on these figures are the cumulative conditional frequency of the sequence from the initiating event (KPDS) up to the point in the sequence where the frequency is given. The frequency of each entire sequence is listed in the column for top event BM. The quantification of each CPET is conditional, i.e., with a KPDS frequency of 1.0. In order to obtain the absolute frequency of each sequence, the conditional frequency for the sequence given in the column "BM" must be multiplied by the frequency of the KPDS.

Figure H-1: CR3 Containment Event Tree (CPET) for KPDS K7D

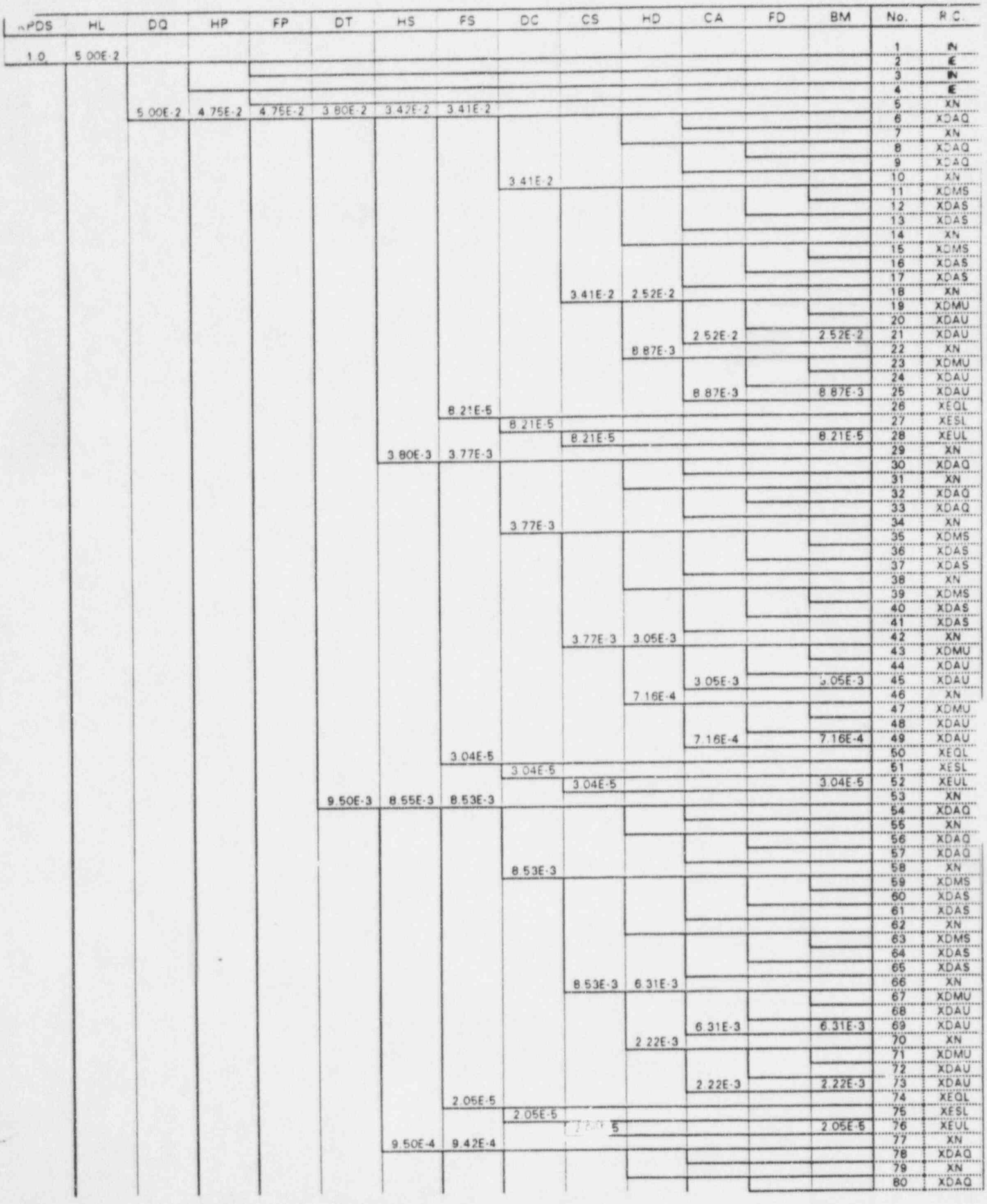

Figure H-1: CR3 Containment Event Tree (CPET) for KPDS K7D

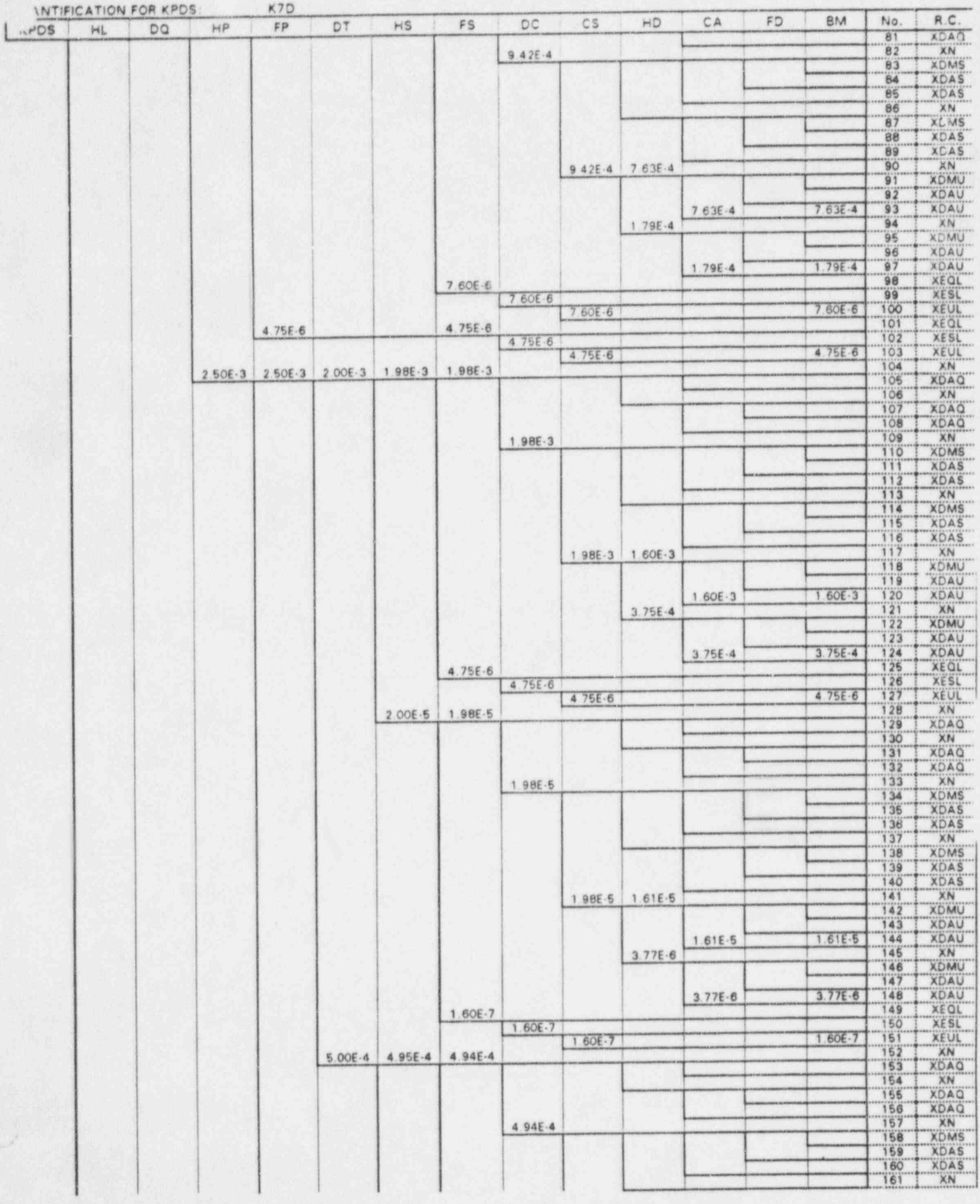

Figure H-1: CR3 Containment Event Tree (CPET) for KPDS K7D

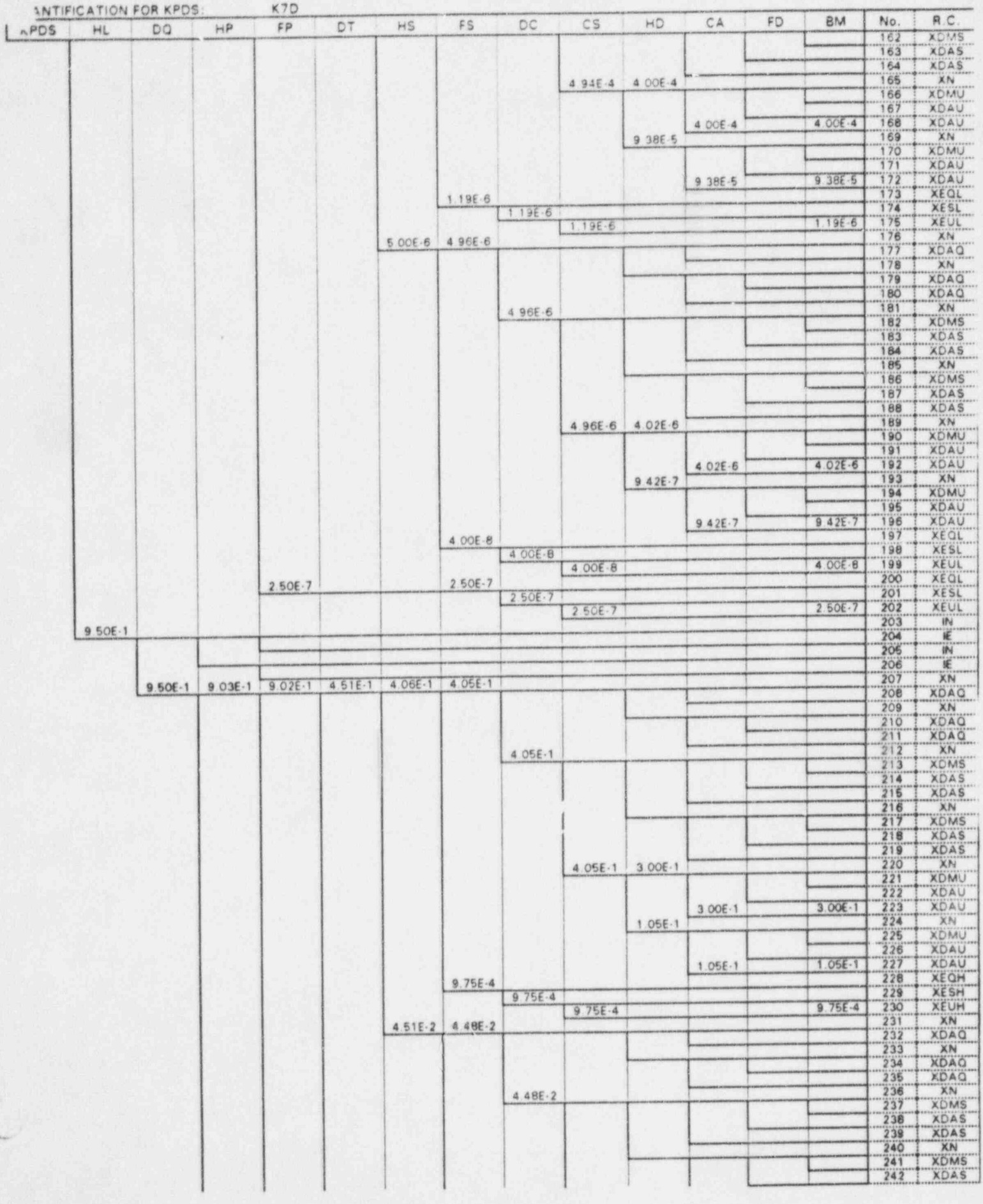

Figure H-1: CR3 Containment Event Tree (CPET) for KPDS K7D

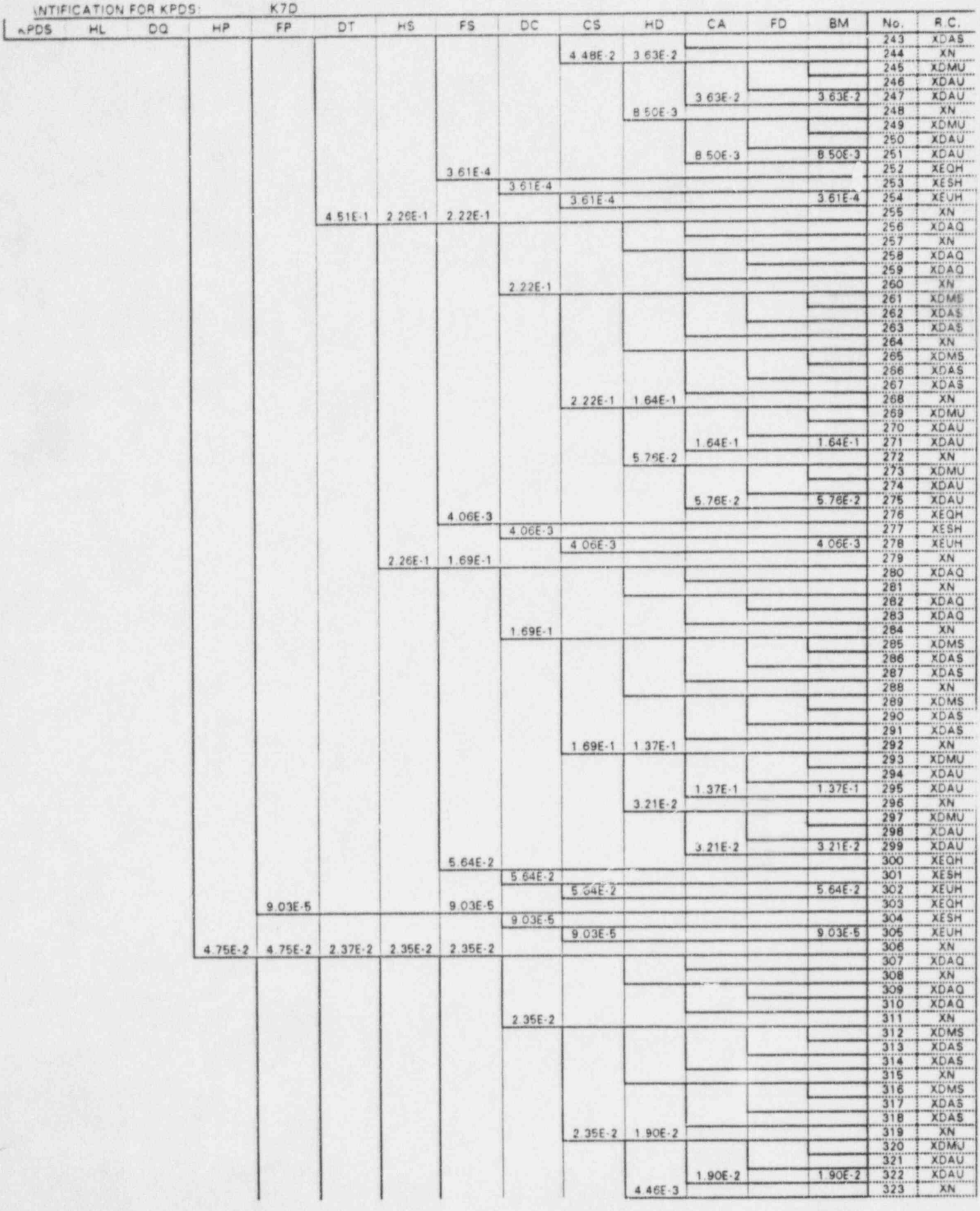

Figure H-1: CR3 Containment Event Tree (CPET) for KPDS K7D

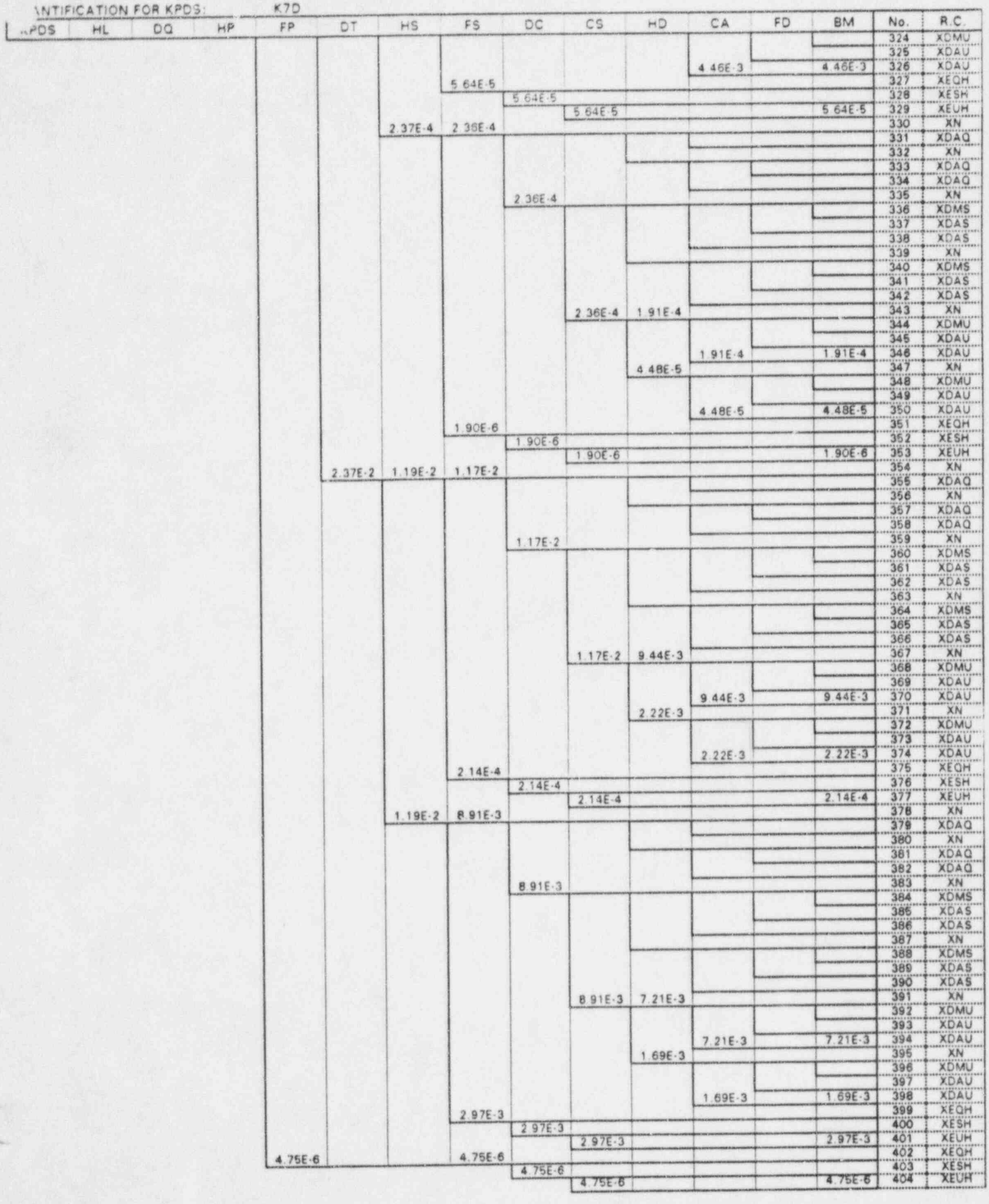

Figure H-2: CR3 Containment Event Tree (CPET) for KPDS K7JH

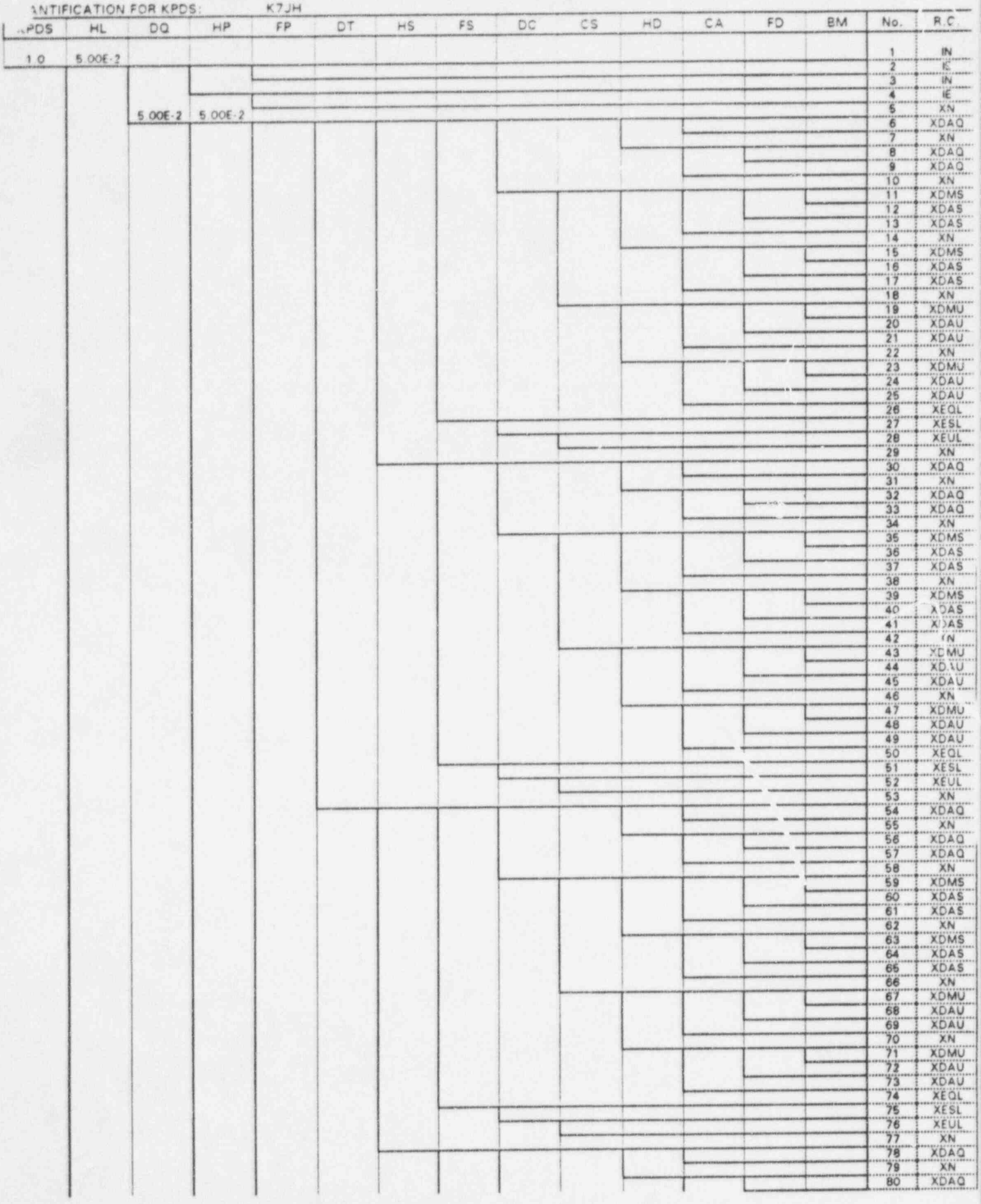

Figure H-2: CR3 Containment Event Tree (CPET) for KPDS K7JH

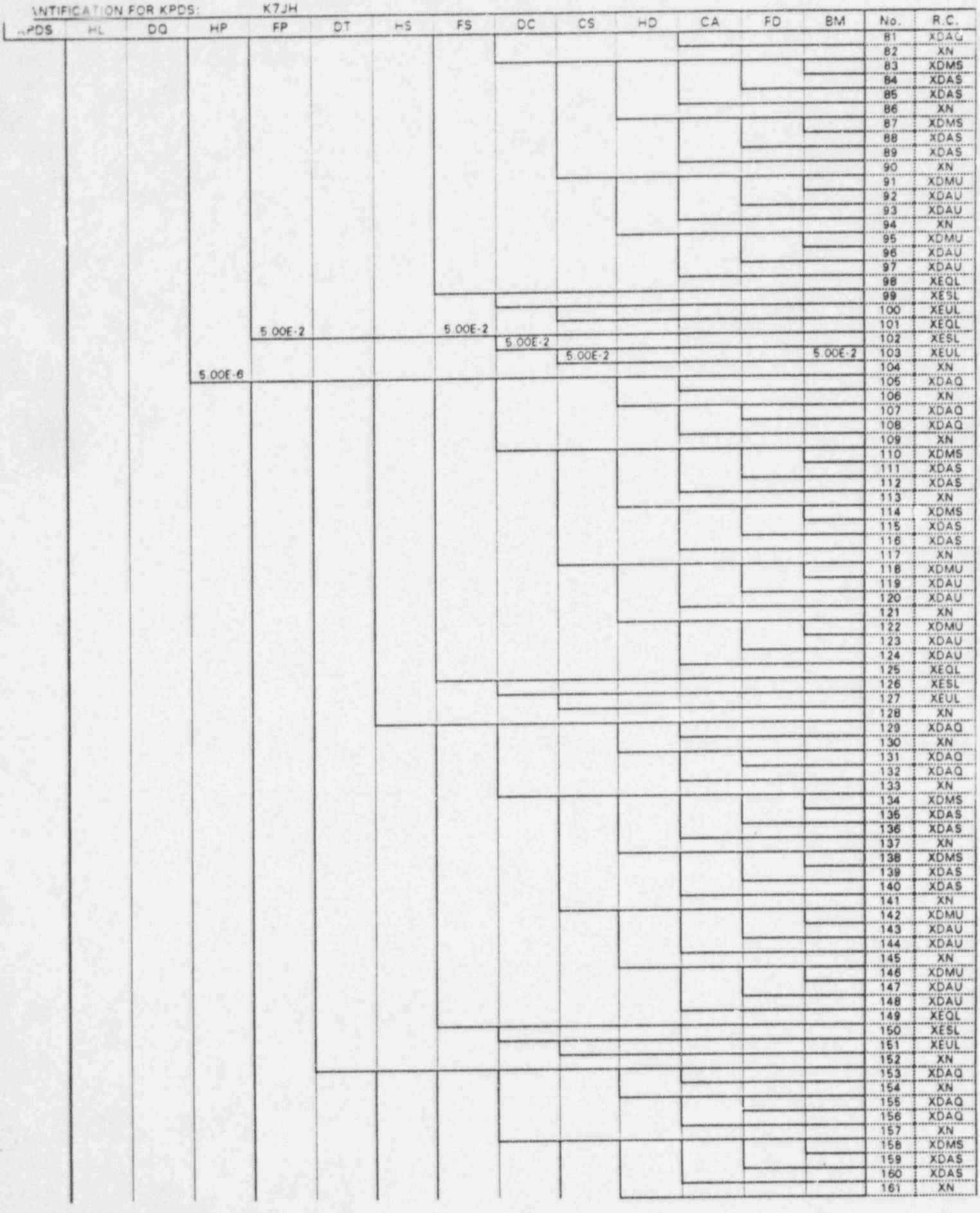

Figure H-2: CR3 Containment Event Tree (CPET) for KPDS K7JH

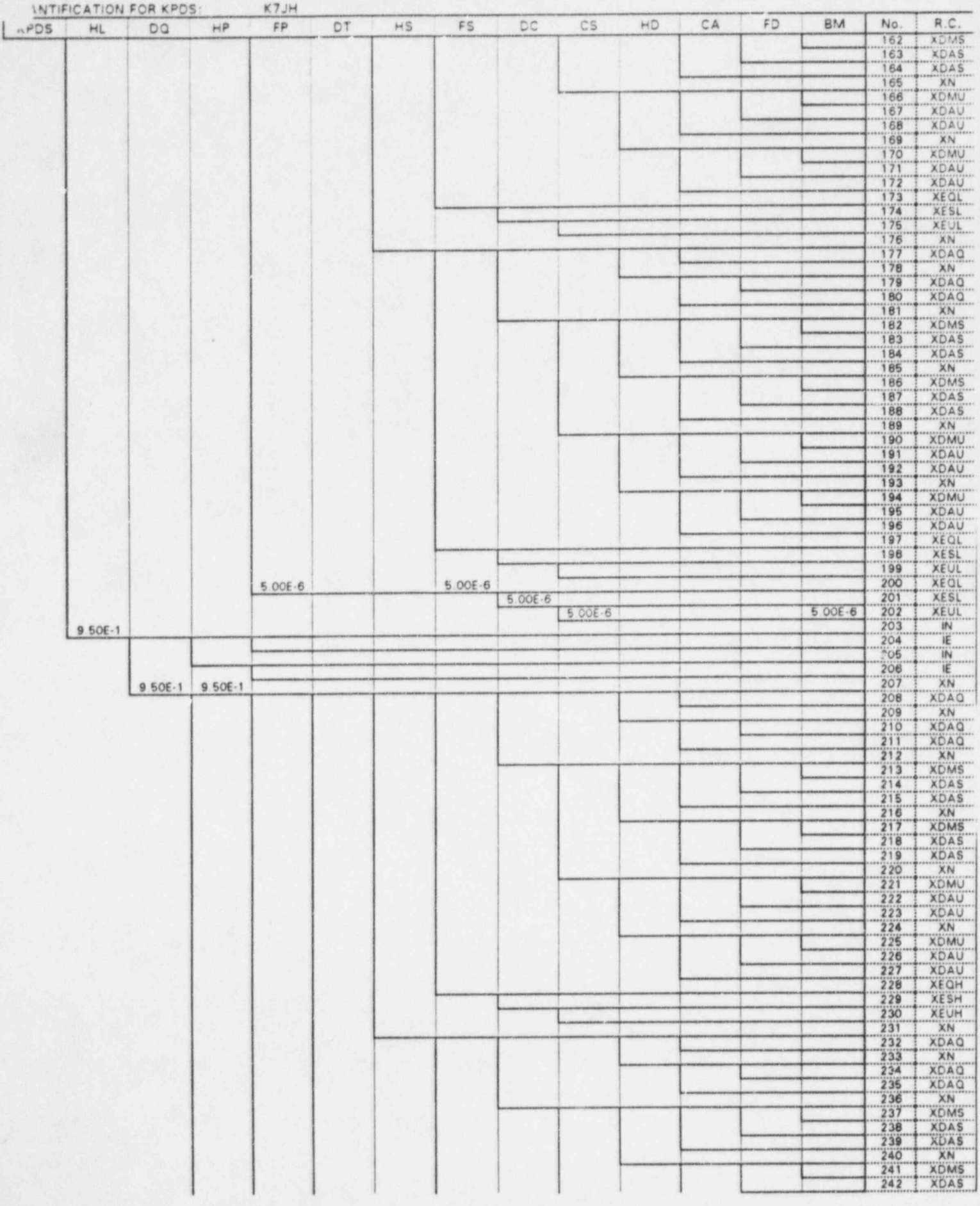

Figure H-2: CR3 Containment Event Tree (CPET) for KPDS K7JH

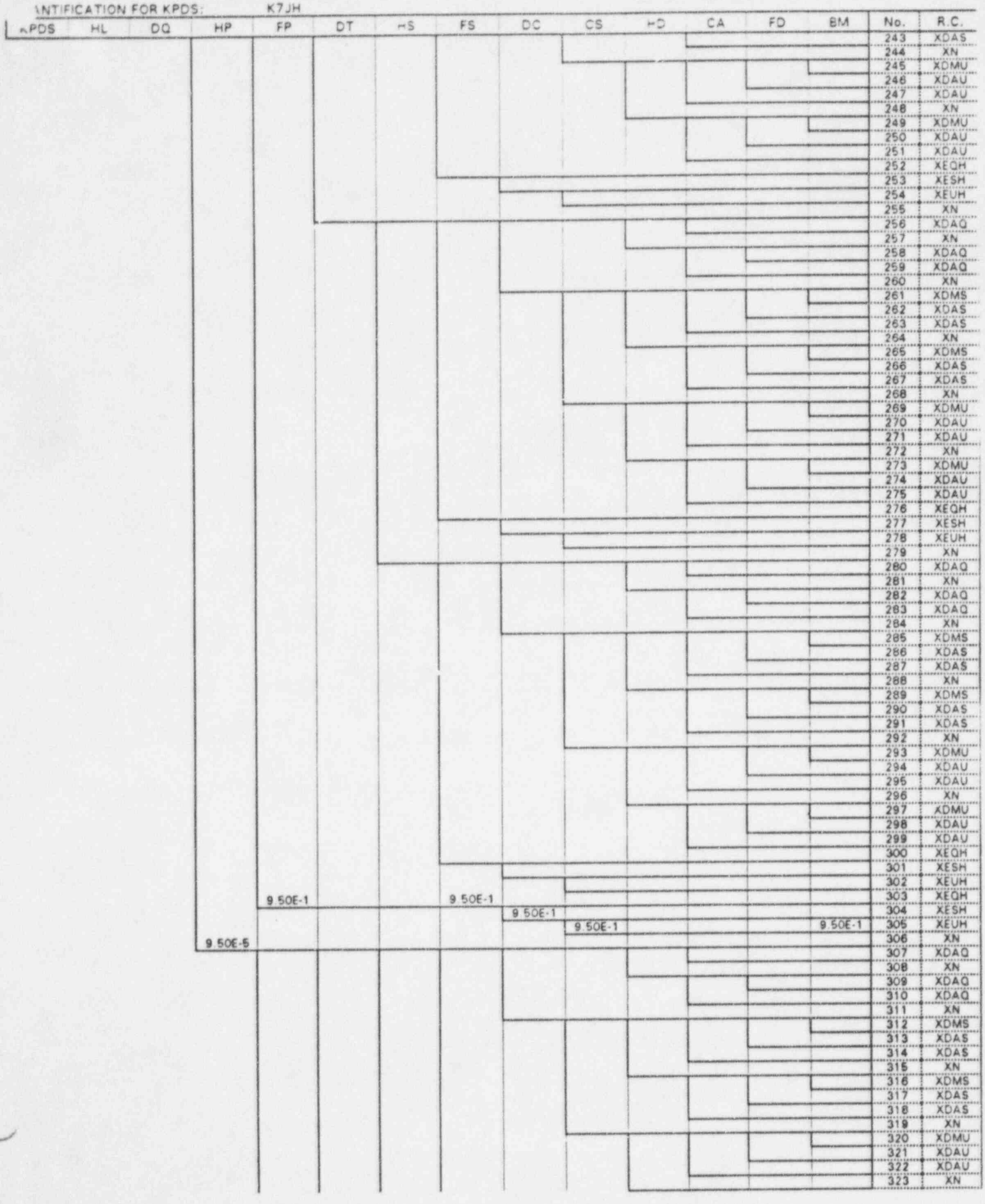

Figure H-2: CR3 Containment Event Tree (CPET) for KPDS K7JH

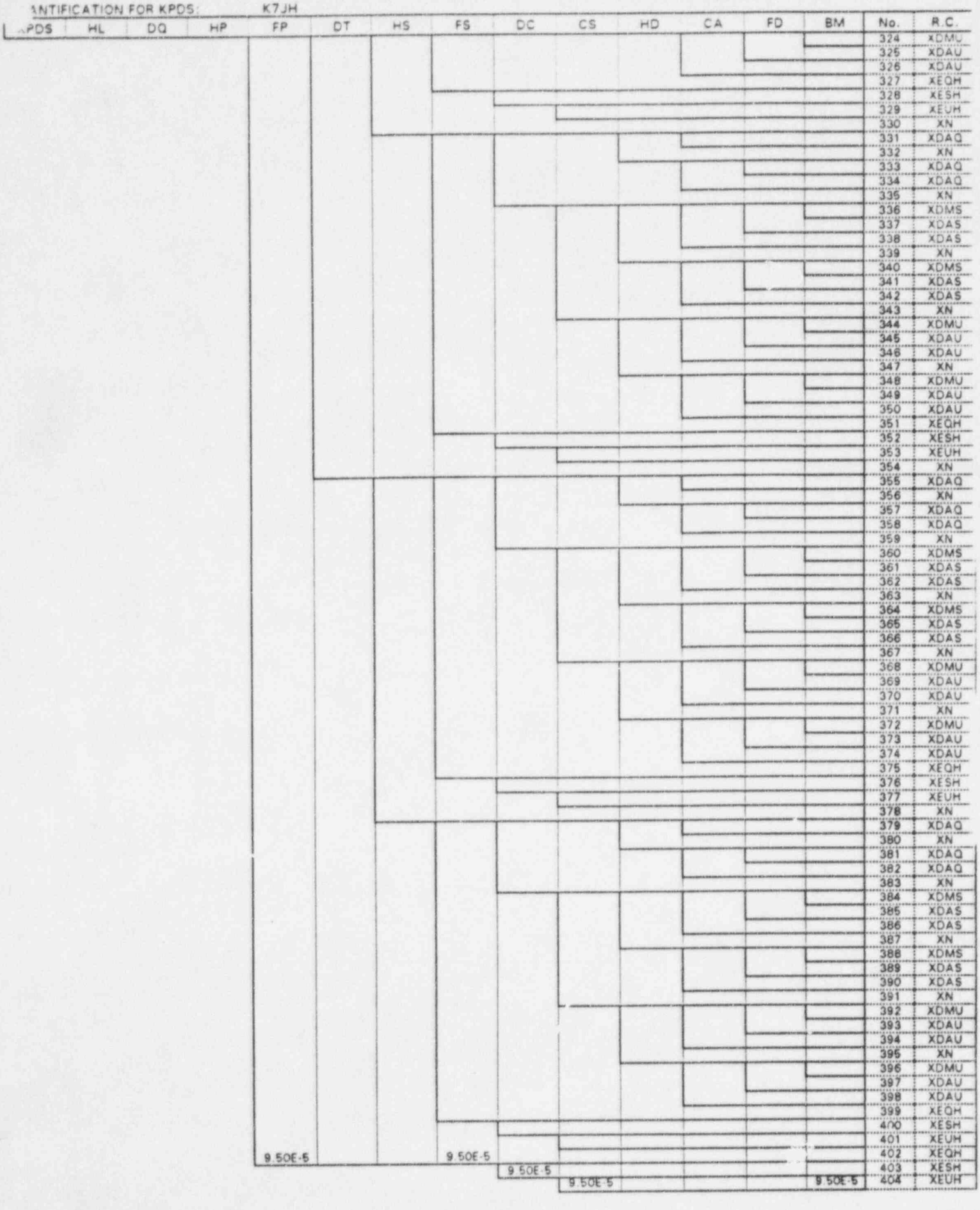

Figure H-3: CR3 Containment Event Tree (CPET) for KPDS K6BA

IDENTIFICATION FOR KPDS: K6BA

KPDS	HL	DQ	HP	FP	DT	HS	FS	DC	CS	HD	CA	FD	BM	No.	R.C.
1.0	1.50E-1													1	IN
														2	IE
														3	IN
														4	IE
		1.50E-1	9.75E-2	9.75E-2	9.75E-3	2.44E-3	2.44E-3	1.22E-3	1.22E-3	2.44E-5	2.44E-5		2.44E-5	5	XN
														6	XDAQ
										1.19E-3	1.07E-3	1.03E-3	1.03E-3	7	XN
												4.19E-5	4.19E-5	8	XDAQ
											1.19E-4		1.19E-4	9	XDAQ
								1.22E-3	1.10E-3					10	XN
														11	XDMS
														12	XDAS
														13	XDAS
										1.10E-3	9.87E-4	9.40E-4	4.70E-4	14	XN
													4.70E-4	15	XDMS
												4.74E-5	4.74E-5	16	XDAS
											1.10E-4		1.10E-4	17	XDAS
									1.22E-4					18	XN
														19	XDMU
														20	XDAU
														21	XDAU
										1.22E-4	1.10E-4	1.04E-4	5.22E-5	22	XN
													5.22E-5	23	XDMU
												5.26E-6	5.26E-6	24	XDAU
											1.22E-5		1.22E-5	25	XDAU
							2.44E-7	1.22E-7					1.22E-7	26	XEQL
								1.22E-7	1.10E-7				1.10E-7	27	XESL
									1.22E-8				1.22E-8	28	XEUL
						7.31E-3	7.20E-3	3.60E-3	3.60E-3	6.12E-4	5.51E-4		5.51E-4	29	XN
											6.12E-5		6.12E-5	30	XDAQ
										2.99E-3	2.69E-3	2.67E-3	2.67E-3	31	XN
												2.42E-5	2.42E-5	32	XDAQ
											2.99E-4		2.99E-4	33	XDAQ
								3.60E-3	3.24E-3	7.13E-4	6.42E-4	6.42E-4	3.21E-4	34	XN
													3.21E-4	35	XDMS
												6.42E-8	6.42E-8	36	XDAS
											7.13E-5		7.13E-5	37	XDAS
										2.53E-3	2.28E-3	2.26E-3	1.13E-3	38	XN
													1.13E-3	39	XDMS
												1.59E-5	1.59E-5	40	XDAS
											2.53E-4		2.53E-4	41	XDAS
									3.60E-4	7.92E-5	7.13E-5	7.13E-5	3.56E-5	42	XN
													3.56E-5	43	XDMU
												7.13E-9	7.13E-9	44	XDAU
											7.92E-6		7.92E-6	45	XDAU
										2.81E-4	2.53E-4	2.51E-4	1.26E-4	46	XN
													1.26E-4	47	XDMU
												1.77E-6	1.77E-6	48	XDAU
											2.81E-5		2.81E-5	49	XDAU
							1.10E-4	5.48E-5					5.48E-5	50	XEQL
								5.48E-5	4.94E-5				4.94E-5	51	XESL
									5.48E-6				5.48E-6	52	XEUL
					8.77E-2	2.19E-2	2.19E-2	2.19E-3	2.19E-3	4.39E-5	4.39E-5		4.39E-5	53	XN
														54	XDAQ
										2.15E-3	1.93E-3	1.86E-3	1.86E-3	55	XN
												7.54E-5	7.54E-5	56	XDAQ
											2.15E-4		2.15E-4	57	XDAQ
								1.97E-2	3.95E-3					58	XN
														59	XDMS
														60	XDAS
														61	XDAS
										3.95E-3	3.55E-3	3.38E-3	3.38E-4	62	XN
													3.04E-3	63	XDMS
												1.71E-4	1.71E-4	64	XDAS
											3.95E-4		3.95E-4	65	XDAS
									1.58E-2					66	XN
														67	XDMU
														68	XDAU
														69	XDAU
										1.58E-2	1.42E-2	1.35E-2	1.35E-3	70	XN
													1.22E-2	71	XDMU
												6.82E-4	6.82E-4	72	XDAU
											1.58E-3		1.58E-3	73	XDAU
							2.19E-6	2.19E-7					2.19E-7	74	XEQL
								1.97E-6	3.95E-7				3.95E-7	75	XESL
									1.58E-6				1.58E-6	76	XEUL
						6.58E-2	6.48E-2	6.48E-3	6.48E-3	1.10E-3	9.92E-4		9.92E-4	77	XN
											1.10E-4		1.10E-4	78	XDAQ
										5.38E-3	4.84E-3	4.80E-3	4.80E-3	79	XN
												4.36E-5	4.36E-5	80	XDAQ

Figure H-3: CR3 Containment Event Tree (CPET) for KPDS K6BA

IDENTIFICATION FOR KPDS: K6BA

KPDS	HL	DQ	HP	FP	DT	HS	FS	DC	CS	HD	CA	FD	BM	No.	R.C.
											5.38E-4		5.38E-4	81	XDAQ
								5.83E-2	1.17E-2	2.57E-3	2.31E-3	2.29E-3	2.29E-4	82	XN
													2.06E-3	83	XDMS
												2.31E-5	2.31E-5	84	XDAS
											2.57E-4		2.57E-4	85	XDAS
										9.10E-3	8.19E-3	8.13E-3	8.13E-4	86	XN
													7.32E-3	87	XDMS
												5.73E-5	5.73E-5	88	XDAS
											9.10E-4		9.10E-4	89	XDAS
									4.67E-2	1.03E-2	9.24E-3	9.15E-3	9.15E-4	90	XN
													8.23E-3	91	XDMU
												9.24E-5	9.24E-5	92	XDAU
											1.03E-3		1.03E-3	93	XDAU
										3.64E-2	3.28E-2	3.25E-2	3.25E-3	94	XN
													2.93E-2	95	XDMU
												2.29E-4	2.29E-4	96	XDAU
											3.64E-3		3.64E-3	97	XDAU
							9.87E-4	9.87E-5					9.87E-5	98	XEQL
								8.88E-4	1.78E-4				1.78E-4	99	XESL
									7.11E-4				7.11E-4	100	XEUL
				9.75E-6			9.75E-6	4.88E-6					4.88E-6	101	XEQL
								4.88E-6	4.39E-6				4.39E-6	102	XESL
									4.88E-7				4.88E-7	103	XEUL
			5.25E-2	5.21E-2	5.21E-3	3.26E-3	3.25E-3	1.63E-3	1.63E-3	2.77E-4	2.49E-4		2.49E-4	104	XN
											2.77E-5		2.77E-5	105	XDAQ
										1.35E-3	1.22E-3	1.20E-3	1.20E-3	106	XN
												1.09E-5	1.09E-5	107	XDAQ
											1.35E-4		1.35E-4	108	XDAQ
								1.63E-3	1.46E-3	3.22E-4	2.90E-4	2.90E-4	1.45E-4	109	XN
													1.45E-4	110	XDMS
												2.90E-8	2.90E-8	111	XDAS
											3.22E-5		3.22E-5	112	XDAS
										1.14E-3	1.03E-3	1.02E-3	5.10E-4	113	XN
													5.10E-4	114	XDMS
												7.20E-6	7.20E-6	115	XDAS
											1.14E-4		1.14E-4	116	XDAS
									1.63E-4	3.58E-5	3.22E-5	3.22E-5	1.61E-5	117	XN
													1.61E-5	118	XDMU
												3.22E-9	3.22E-9	119	XDAU
											3.58E-6		3.58E-6	120	XDAU
										1.27E-4	1.14E-4	1.13E-4	5.67E-5	121	XN
													5.67E-5	122	XDMU
												8.00E-7	8.00E-7	123	XDAU
											1.27E-5		1.27E-5	124	XDAU
							3.26E-7	1.63E-7					1.63E-7	125	XEQL
								1.63E-7	1.46E-7				1.46E-7	126	XESL
									1.63E-8				1.63E-8	127	XEUL
						1.95E-3	1.92E-3	9.62E-4	9.62E-4	1.64E-4	1.47E-4		1.47E-4	128	XN
											1.64E-5		1.64E-5	129	XDAQ
										7.98E-4	7.19E-4	7.12E-4	7.12E-4	130	XN
												6.47E-6	6.47E-6	131	XDAQ
											7.98E-5		7.98E-5	132	XDAQ
								9.62E-4	8.66E-4	1.90E-4	1.71E-4	1.71E-4	8.57E-5	133	XN
													8.57E-5	134	XDMS
												1.71E-8	1.71E-8	135	XDAS
											1.90E-5		1.90E-5	136	XDAS
										6.75E-4	6.08E-4	6.03E-4	3.02E-4	137	XN
													3.02E-4	138	XDMS
												4.25E-6	4.25E-6	139	XDAS
											6.75E-5		6.75E-5	140	XDAS
									9.62E-5	2.12E-5	1.90E-5	1.90E-5	9.52E-6	141	XN
													9.52E-6	142	XDMU
												1.90E-9	1.90E-9	143	XDAU
											2.12E-6		2.12E-6	144	XDAU
										7.50E-5	6.75E-5	6.70E-5	3.35E-5	145	XN
													3.35E-5	146	XDMU
												4.73E-7	4.73E-7	147	XDAU
											7.50E-6		7.50E-6	148	XDAU
							2.93E-5	1.46E-5					1.46E-5	149	XEQL
								1.46E-5	1.32E-5				1.32E-5	150	XESL
									1.46E-6				1.46E-6	151	XEUL
					4.69E-2	2.93E-2	2.93E-2	2.93E-3	2.93E-3	4.98E-4	4.48E-4		4.48E-4	152	XN
											4.98E-5		4.98E-5	153	XDAQ
										2.43E-3	2.19E-3	2.17E-3	2.17E-3	154	XN
												1.97E-5	1.97E-5	155	XDAQ
											2.43E-4		2.43E-4	156	XDAQ
								2.64E-2	5.27E-3	1.16E-3	1.04E-3	1.03E-3	1.03E-4	157	XN
													9.30E-4	158	XDMS
												1.04E-5	1.04E-5	159	XDAS
											1.16E-4		1.16E-4	160	XDAS
										4.11E-3	3.70E-3	3.68E-3	3.68E-4	161	XN

Figure H-3: CR3 Containment Event Tree (CPET) for KPDS K6BA

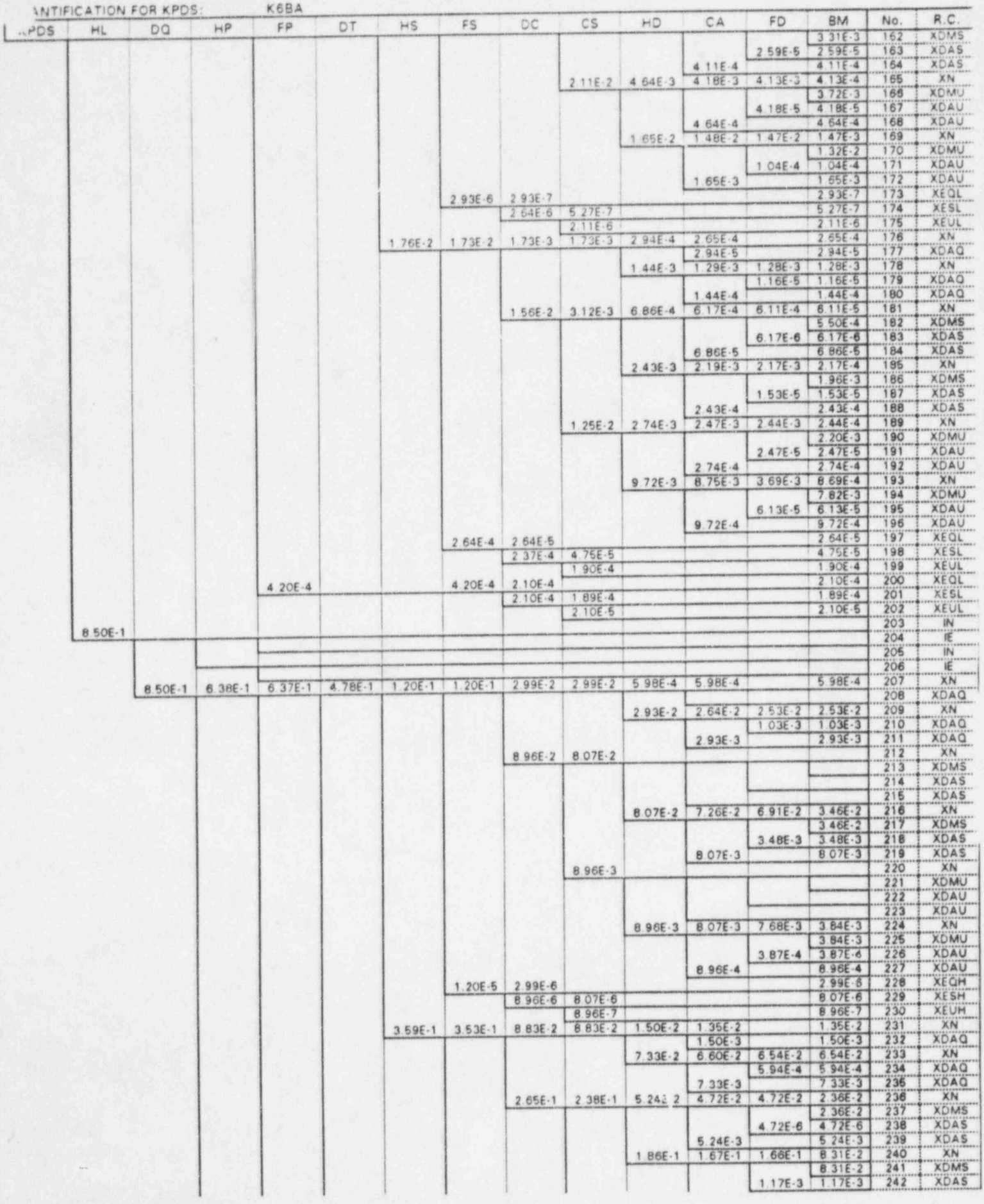

Figure H-3: CR3 Containment Event Tree (CPET) for KPDS K6BA

IDENTIFICATION FOR KPDS: K6BA

KPDS	HL	DG	HP	FP	DT	HS	FS	DC	CS	HD	CA	FD	BM	No.	R.C.
											1.86E-2		1.86E-2	243	XDAS
									2.65E-2	5.83E-3	5.24E-3	5.24E-3	2.62E-3	244	XN
													2.62E-3	245	XDMU
												5.24E-7	5.24E-7	246	XDAU
											5.83E-4		5.83E-4	247	XDAU
										2.07E-2	1.86E-2	1.85E-2	9.23E-3	248	XN
													9.23E-3	249	XDMU
												1.30E-4	1.30E-4	250	XDAU
											2.07E-3		2.07E-3	251	XDAU
							5.38E-3	1.34E-3					1.34E-3	252	XEQH
								4.03E-3	3.63E-3				3.63E-3	253	XESH
									4.03E-4				4.03E-4	254	XEUH
					1.59E-1	7.97E-2	7.95E-2	3.98E-2	3.98E-2	7.95E-4	3.98E-4		3.98E-4	255	XN
											3.98E-4		3.98E-4	256	XDAQ
										3.90E-2	1.95E-2	1.87E-2	1.87E-2	257	XN
												7.60E-4	7.60E-4	258	XDAQ
											1.95E-2		1.95E-2	259	XDAQ
								3.98E-2	3.58E-2					260	XN
														261	XDMS
														262	XDAS
														263	XDAS
										3.58E-2	1.79E-2	1.70E-2	8.52E-3	264	XN
													8.52E-3	265	XDMS
												8.59E-4	8.59E-4	266	XDAS
											1.79E-2		1.79E-2	267	XDAS
									3.98E-3					268	XN
														269	XDMU
														270	XDAU
														271	XDAU
										3.98E-3	1.99E-3	1.99E-3	9.46E-4	272	XN
													9.46E-4	273	XDMU
												9.54E-5	9.54E-5	274	XDAU
											1.99E-3		1.99E-3	275	XDAU
							1.59E-4	7.97E-5					7.97E-5	276	XEQH
								7.97E-5	7.17E-5				7.17E-5	277	XESH
									7.97E-6				7.97E-6	278	XEUH
						7.97E-2	7.17E-2	3.59E-2	3.59E-2	6.10E-3	3.05E-3		3.05E-3	279	XN
											3.05E-3		3.05E-3	280	XDAC
										2.98E-2	1.49E-2	1.47E-2	1.47E-2	281	XN
												1.34E-4	1.34E-4	282	XDAQ
											1.49E-2		1.49E-2	283	XDAQ
								3.59E-2	3.23E-2	7.10E-3	3.55E-3	3.55E-3	1.77E-3	284	XN
													1.77E-3	285	XDMS
												3.55E-7	3.55E-7	286	XDAS
											3.55E-3		3.55E-3	287	XDAS
										2.52E-2	1.26E-2	1.25E-2	6.25E-3	288	XN
													6.25E-3	289	XDMS
												8.81E-5	8.81E-5	290	XDAS
											1.26E-2		1.26E-2	291	XDAS
									3.59E-3	7.89E-4	3.94E-4	3.94E-4	1.97E-4	292	XN
													1.97E-4	293	XDMU
												3.94E-8	3.94E-8	294	XDAU
											3.94E-4		3.94E-4	295	XDAU
										2.80E-3	1.40E-3	1.39E-3	6.94E-4	296	XN
													6.94E-4	297	XDMU
												9.79E-6	9.79E-6	298	XDAU
											1.40E-3		1.40E-3	299	XDAU
							7.97E-3	3.98E-3					3.98E-3	300	XEQH
								3.98E-3	3.59E-3				3.59E-3	301	XESH
									3.98E-4				3.98E-4	302	XEUH
				6.38E-5			6.38E-5	1.59E-5					1.59E-5	303	XEQH
								4.78E-5	4.30E-5				4.30E-5	304	XESH
								4.78E-6					4.78E-6	305	XEUH
			2.13E-1	2.11E-1	1.58E-1	9.88E-2	9.88E-2	2.47E-2	2.47E-2	4.20E-3	3.78E-3		3.78E-3	306	XN
											4.20E-4		4.20E-4	307	XDAQ
										2.05E-2	1.85E-2	1.83E-2	1.83E-2	308	XN
												1.66E-4	1.66E-4	309	XDAQ
											2.05E-3		2.05E-3	310	XDAQ
								7.41E-2	6.67E-2	1.47E-2	1.32E-2	1.32E-2	6.60E-3	311	XN
													6.60E-3	312	XDMS
												1.32E-6	1.32E-6	313	XDAS
											1.47E-3		1.47E-3	314	XDAS
										5.20E-2	4.68E-2	4.65E-2	2.32E-2	315	XN
													2.32E-2	316	XDMS
												3.28E-4	3.28E-4	317	XDAS
											5.20E-3		5.20E-3	318	XDAS
									7.41E-3	1.63E-3	1.47E-3	1.47E-3	7.34E-4	319	XN
													7.34E-4	320	XDMU
												1.47E-7	1.47E-7	321	XDAU
											1.63E-4		1.63E-4	322	XDAU
										5.78E-3	5.20E-3	5.17E-3	2.58E-3	323	XN

Figure H-3: CR3 Containment Event Tree (CPET) for KPDS K6BA

IDENTIFICATION FOR KPDS: K6BA

KPDS	HL	DQ	HP	FP	DT	HS	FS	DC	CS	HD	CA	FD	BM	No.	R.C.
													2.58E-3	324	XDMU
												3.64E-5	3.64E-5	325	XDAU
											5.78E-4		5.78E-4	326	XDAU
							9.88E-6	2.47E-6					2.47E-6	327	XEQH
								7.41E-6	6.67E-6				6.67E-6	328	XESH
									7.41E-7				7.41E-7	329	XEUH
						5.93E-2	5.84E-2	1.46E-2	1.46E-2	2.48E-3	2.23E-3		2.23E-3	330	XN
											2.48E-4		2.48E-4	331	XDAQ
										1.21E-2	1.09E-2	1.08E-2	1.08E-2	332	XN
												9.82E-5	9.82E-5	333	XDAQ
											1.21E-3		1.21E-3	334	XDAQ
								4.38E-2	3.94E-2	8.67E-3	7.80E-3	7.80E-3	3.90E-3	335	XN
													3.90E-3	336	XDMS
												7.80E-7	7.80E-7	337	XDAS
											8.67E-4		8.67E-4	338	XDAS
										3.07E-2	2.77E-2	2.75E-2	1.37E-2	339	XN
													1.37E-2	340	XDMS
												1.94E-4	1.94E-4	341	XDAS
											3.07E-3		3.07E-3	342	XDAS
									4.38E-3	9.64E-4	8.67E-4	8.67E-4	4.34E-4	343	XN
													4.34E-4	344	XDMU
												8.67E-8	8.67E-8	345	XDAU
											9.64E-5		9.64E-5	346	XDAU
										3.42E-3	3.07E-3	3.05E-3	1.53E-3	347	XN
													1.53E-3	348	XDMU
												2.15E-5	2.15E-5	349	XDAU
											3.42E-4		3.42E-4	350	XDAU
							8.89E-4	2.22E-4					2.22E-4	351	XEQH
								6.67E-4	6.00E-4				6.00E-4	352	XESH
									6.67E-5				6.67E-5	353	XEUH
					5.27E-2	2.64E-2	2.63E-2	1.31E-2	1.31E-2	2.24E-3	1.12E-3		1.12E-3	354	XN
											1.12E-3		1.12E-3	355	XDAQ
										1.09E-2	5.46E-3	5.41E-3	5.41E-3	356	XN
												4.91E-5	4.91E-5	357	XDAQ
											5.46E-3		5.46E-3	358	XDAQ
								1.31E-2	1.18E-2	2.60E-3	1.30E-3	1.30E-3	6.51E-4	359	XN
													6.51E-4	360	XDMS
												1.30E-7	1.30E-7	361	XDAS
											1.30E-3		1.30E-3	362	XDAS
										9.23E-3	4.62E-3	4.58E-3	2.29E-3	363	XN
													2.29E-3	364	XDMS
												3.23E-5	3.23E-5	365	XDAS
											4.62E-3		4.62E-3	366	XDAS
									1.31E-3	2.89E-4	1.45E-4	1.45E-4	7.23E-5	367	XN
													7.23E-5	368	XDMU
												1.45E-8	1.45E-8	369	XDAU
											1.45E-4		1.45E-4	370	XDAU
										1.03E-3	5.13E-4	5.09E-4	2.55E-4	371	XN
													2.55E-4	372	XDMU
												3.59E-6	3.59E-6	373	XDAU
											5.13E-4		5.13E-4	374	XDAU
							5.27E-5	2.64E-5					2.64E-5	375	XEQH
								2.64E-5	2.37E-5				2.37E-5	376	XESH
									2.64E-6				2.64E-6	377	XEUH
						2.64E-2	2.37E-2	1.19E-2	1.19E-2	2.02E-3	1.01E-3		1.01E-3	378	XN
											1.01E-3		1.01E-3	379	XDAQ
										9.84E-3	4.92E-3	4.88E-3	4.88E-3	380	XN
												4.43E-5	4.43E-5	381	XDAQ
											4.92E-3		4.92E-3	382	XDAQ
								1.19E-2	1.07E-2	2.35E-3	1.17E-3	1.17E-3	5.87E-4	383	XN
													5.87E-4	384	XDMS
												1.17E-7	1.17E-7	385	XDAS
											1.17E-3		1.17E-3	386	XDAS
										8.32E-3	4.16E-3	4.13E-3	2.07E-3	387	XN
													2.07E-3	388	XDMS
												2.91E-5	2.91E-5	389	XDAS
											4.16E-3		4.16E-3	390	XDAS
									1.19E-3	2.61E-4	1.30E-4	1.30E-4	6.52E-5	391	XN
													6.52E-5	392	XDMU
												1.30E-8	1.30E-8	393	XDAU
											1.30E-4		1.30E-4	394	XDAU
										9.25E-4	4.62E-4	4.59E-4	2.30E-4	395	XN
													2.30E-4	396	XDMU
												3.24E-6	3.24E-6	397	XDAU
											4.62E-4		4.62E-4	398	XDAU
							2.64E-3	1.32E-3					1.32E-3	399	XEQH
								1.32E-3	1.19E-3				1.19E-3	400	XESH
									1.32E-4				1.32E-4	401	XEUH
				1.70E-3			1.70E-3	4.25E-4					4.25E-4	402	XEQH
								1.28E-3	1.15E-3				1.15E-3	403	XESH
									1.28E-4				1.28E-4	404	XEUH

Figure H-4: CR3 Containment Event Tree (CPET) for KPDS K4K

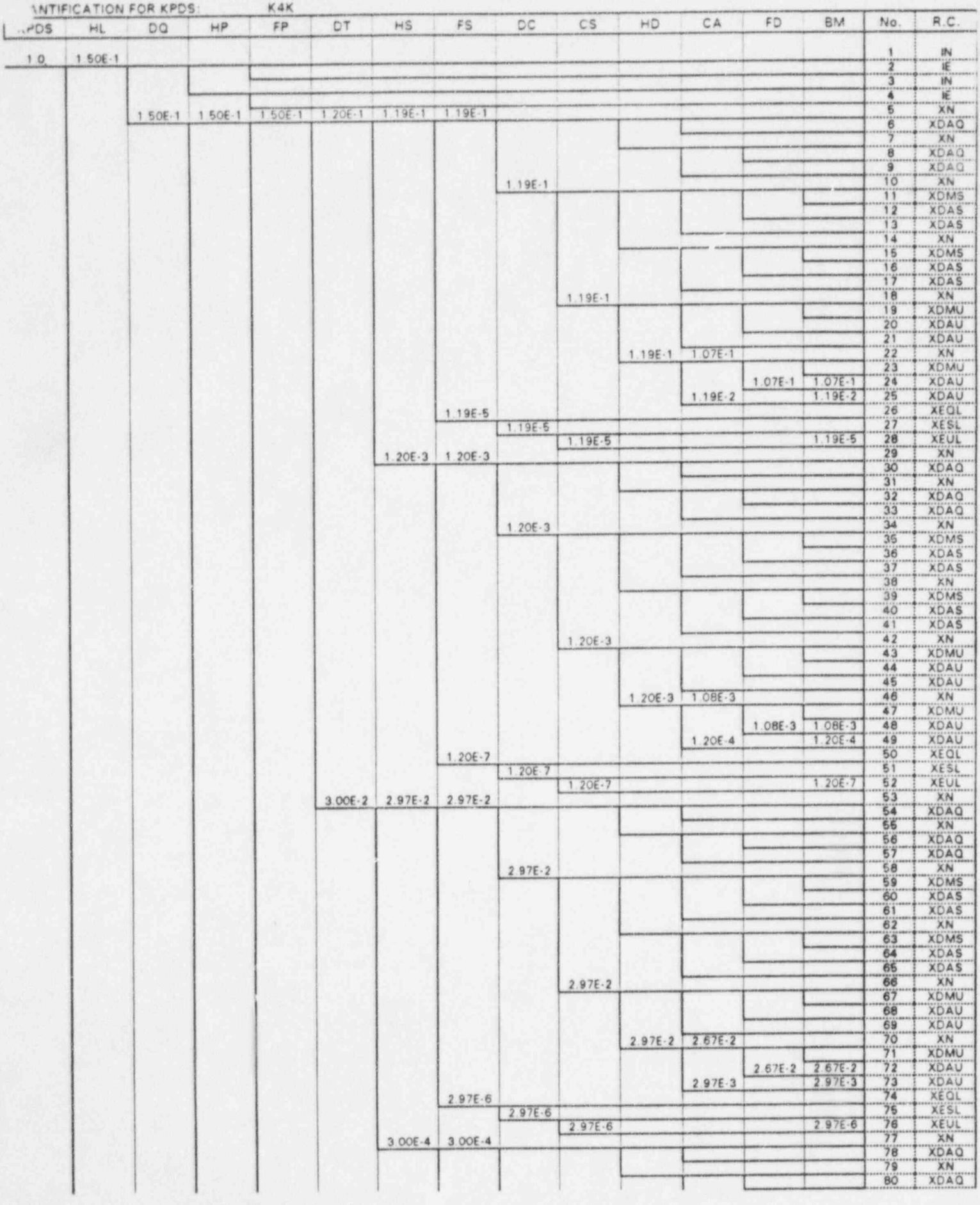

Figure H-4: CR3 Containment Event Tree (CPET) for KPDS K4K

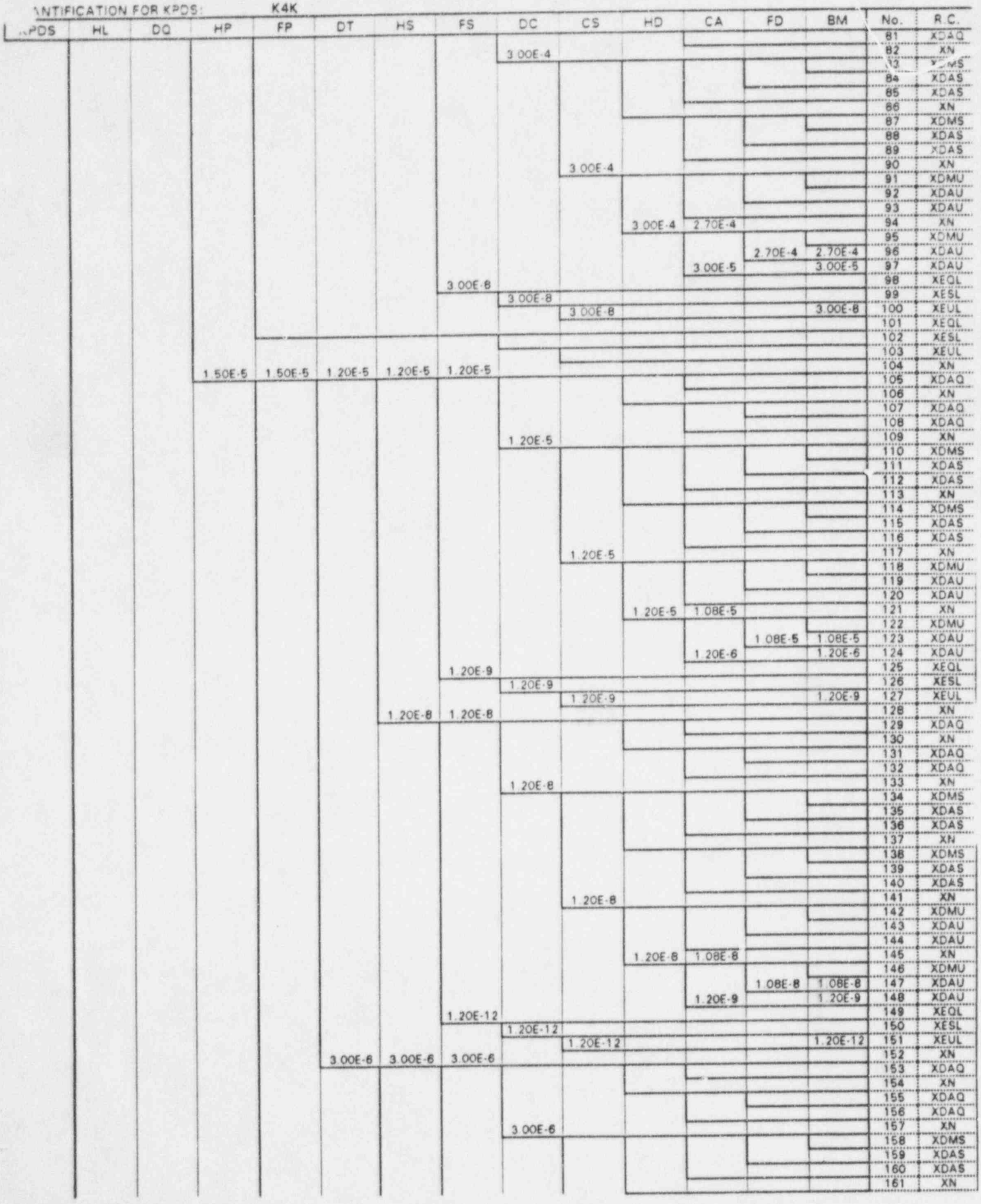

Figure H-4: CR3 Containment Event Tree (CPET) for KPDS K4K

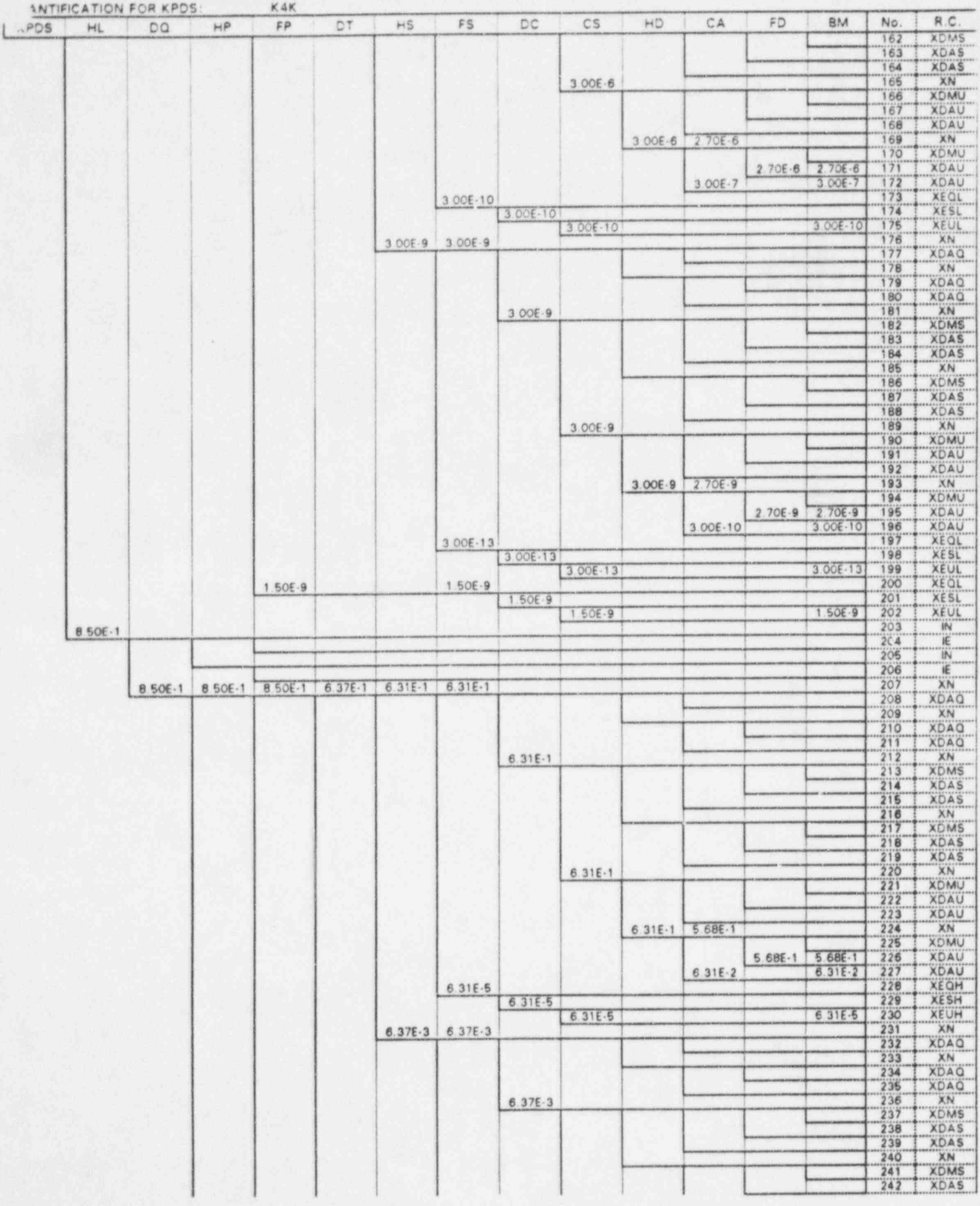

Figure H-4: CR3 Containment Event Tree (CPET) for KPDS K4K

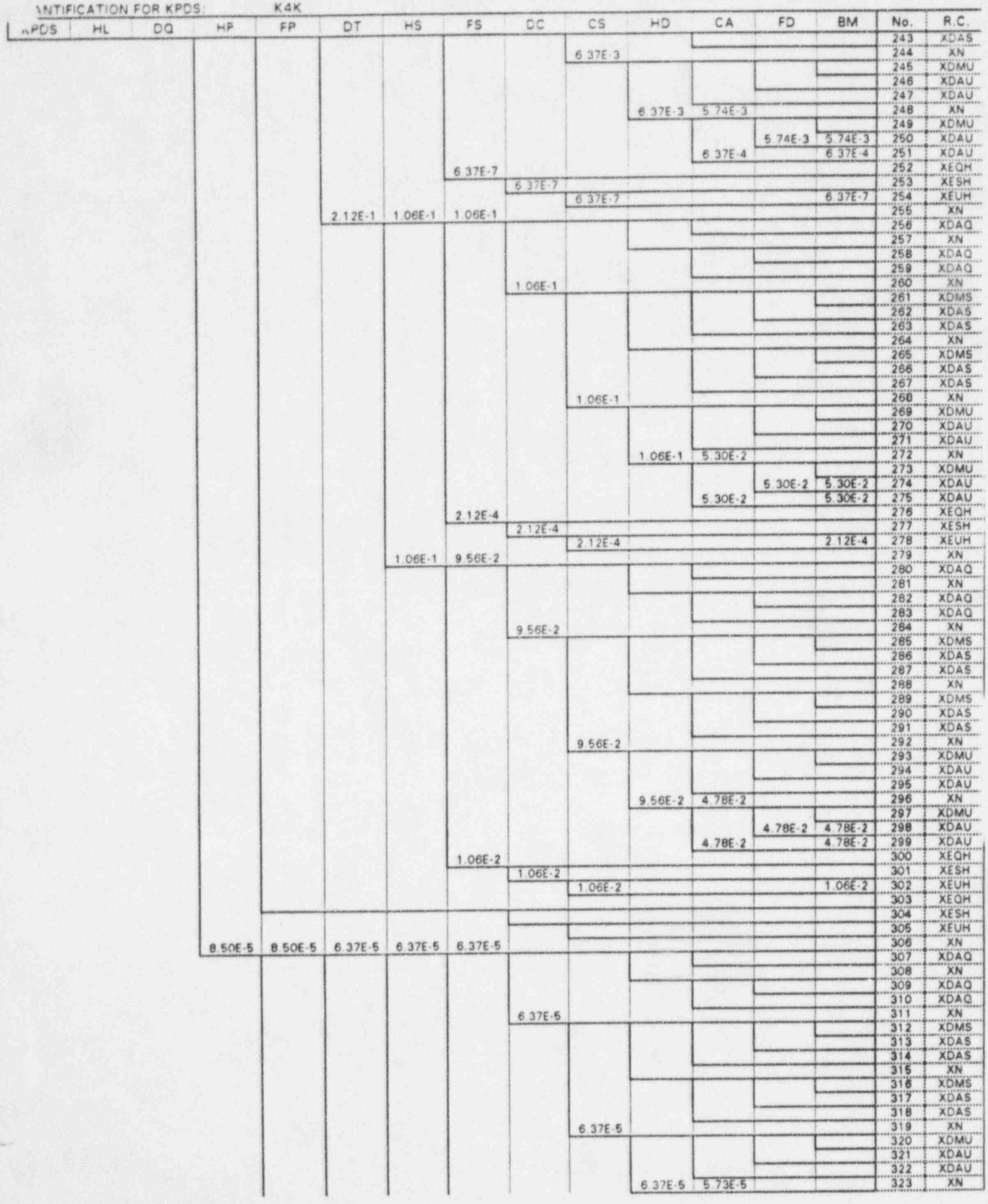

Figure H-4: CR3 Containment Event Tree (CPET) for KPDS K4K

IDENTIFICATION FOR KPDS: K4K

KPDS	HL	DQ	HP	FP	DT	HS	FS	DC	CS	HD	CA	FD	BM	No.	R.C.
														324	XDMU
												5.73E-5	5.73E-5	325	XDAU
											6.37E-6		6.37E-6	326	XDAU
							6.37E-9							327	XEQH
								6.37E-9						328	XESH
									6.37E-9				6.37E-9	329	XEUH
						6.37E-8	6.37E-8							330	XN
														331	XDAQ
														332	XN
														333	XDAQ
														334	XDAQ
								6.37E-8						335	XN
														336	XDMS
														337	XDAS
														338	XDAS
														339	XN
														340	XDMS
														341	XDAS
														342	XDAS
									6.37E-8					343	XN
														344	XDMU
														345	XDAU
														346	XDAU
										6.37E-8	5.74E-8			347	XN
														348	XDMU
												5.74E-8	5.74E-8	349	XDAU
											6.37E-9		6.37E-9	350	XDAU
							6.37E-12							351	XEQH
								6.37E-12						352	XESH
									6.37E-12				6.37E-12	353	XEUH
					2.12E-5	1.06E-5	1.06E-5							354	XN
														355	XDAQ
														356	XN
														357	XDAQ
														358	XDAQ
								1.06E-5						359	XN
														360	XDMS
														361	XDAS
														362	XDAS
														363	XN
														364	XDMS
														365	XDAS
														366	XDAS
									1.06E-5					367	XN
														368	XDMU
														369	XDAU
														370	XDAU
										1.06E-5	5.30E-6			371	XN
														372	XDMU
												5.30E-6	5.30E-6	373	XDAU
											5.30E-6		5.30E-6	374	XDAU
							2.12E-8							375	XEQH
								2.12E-8						376	XESH
									2.12E-8				2.12E-8	377	XEUH
						1.06E-5	9.56E-6							378	XN
														379	XDAQ
														380	XN
														381	XDAQ
														382	XDAQ
								9.56E-6						383	XN
														384	XDMS
														385	XDAS
														386	XDAS
														387	XN
														388	XDMS
														389	XDAS
														390	XDAS
									9.56E-6					391	XN
														392	XDMU
														393	XDAU
														394	XDAU
										9.56E-6	4.78E-6			395	XN
														396	XDMU
												4.78E-6	4.78E-6	397	XDAU
											4.78E-6		4.78E-6	398	XDAU
							1.06E-6							399	XEQH
								1.06E-6						400	XESH
									1.06E-6				1.06E-6	401	XEUH
				8.50E-9			8.50E-9							402	XEQH
								8.50E-9						403	XESH
									8.50E-9				8.50E-9	404	XEUH

Figure H-5: CR3 Containment Event Tree (CPET) for KPDS K3BA

IDENTIFICATION FOR KPDS: K3BA

KPDS	HL	DQ	HP	FP	DT	HS	FS	DC	CS	HD	CA	FD	BM	No.	R.C.
														1	IN
1.0	1.00E+0													2	IE
														3	IN
														4	IE
		1.00E+0	5.00E-1	5.00E-1	5.00E-2	1.25E-2	1.25E-2	6.25E-3	6.25E-3	1.69E-3	1.69E-3		1.69E-3	5	XN
														6	XDAQ
										4.56E-3	4.11E-3	4.08E-3	4.08E-3	7	XN
												2.87E-5	2.87E-5	8	XDAQ
											4.56E-4		4.56E-4	9	XDAQ
								6.25E-3	5.62E-3	5.62E-5	5.06E-5	5.06E-5	2.53E-5	10	XN
													2.53E-5	11	XDMS
												5.06E-9	5.06E-9	12	XDAS
											5.62E-6		5.62E-6	13	XDAS
										5.57E-3	5.01E-3	4.78E-3	2.39E-3	14	XN
													2.39E-3	15	XDMS
												2.31E-4	2.31E-4	16	XDAS
											5.57E-4		5.57E-4	17	XDAS
									6.25E-4	6.25E-6	5.62E-6	5.62E-6	2.81E-6	18	XN
													2.81E-6	19	XDMU
												5.62E-10	5.62E-10	20	XDAU
											6.25E-7		6.25E-7	21	XDAU
										6.19E-4	5.57E-4	5.31E-4	2.66E-4	22	XN
													2.66E-4	23	XDMU
												2.56E-5	2.56E-5	24	XDAU
											6.19E-5		6.19E-5	25	XDAU
							1.25E-6	6.25E-7					6.25E-7	26	XEQL
								6.25E-7	5.62E-7				5.62E-7	27	XESL
									6.25E-8				6.25E-8	28	XEUL
						3.75E-2	3.67E-2	1.84E-2	1.84E-2	8.64E-3	7.77E-3		7.77E-3	29	XN
											8.64E-4		8.64E-4	30	XDAQ
										9.74E-3	8.76E-3	8.74E-3	8.74E-3	31	XN
												2.63E-5	2.63E-5	32	XDAQ
											9.74E-4		9.74E-4	33	XDAQ
								1.84E-2	1.65E-2	9.92E-4	8.93E-4	8.93E-4	4.46E-4	34	XN
													4.46E-4	35	XDMS
												8.93E-8	8.93E-8	36	XDAS
											9.92E-5		9.92E-5	37	XDAS
										1.55E-2	1.40E-2	1.36E-2	6.77E-3	38	XN
													6.77E-3	39	XDMS
												4.48E-4	4.48E-4	40	XDAS
											1.55E-3		1.55E-3	41	XDAS
									1.84E-3	1.10E-4	9.92E-5	9.92E-5	4.96E-5	42	XN
													4.96E-5	43	XDMU
												9.92E-9	9.92E-9	44	XDAU
											1.10E-5		1.10E-5	45	XDAU
										1.73E-3	1.55E-3	1.50E-3	7.52E-4	46	XN
													7.52E-4	47	XDMU
												4.97E-5	4.97E-5	48	XDAU
											1.73E-4		1.73E-4	49	XDAU
							7.50E-4	3.75E-4					3.75E-4	50	XEQL
								3.75E-4	3.37E-4				3.37E-4	51	XESL
									3.75E-5				3.75E-5	52	XEUL
					4.50E-1	1.12E-1	1.12E-1	1.12E-2	1.12E-2	3.04E-3	3.04E-3		3.04E-3	53	XN
														54	XDAQ
										8.21E-3	7.39E-3	7.34E-3	7.34E-3	55	XN
												5.17E-5	5.17E-5	56	XDAQ
											8.21E-4		8.21E-4	57	XDAQ
								1.01E-1	2.02E-2	2.02E-4	1.82E-4	1.80E-4	1.80E-5	58	XN
													1.62E-4	59	XDMS
												1.82E-6	1.82E-6	60	XDAS
											2.02E-5		2.02E-5	61	XDAS
										2.00E-2	1.80E-2	1.72E-2	1.72E-3	62	XN
													1.55E-2	63	XDMS
												8.30E-4	8.30E-4	64	XDAS
											2.00E-3		2.00E-3	65	XDAS
									8.10E-2	8.10E-4	7.29E-4	7.22E-4	7.22E-5	66	XN
													6.49E-4	67	XDMU
												7.29E-6	7.29E-6	68	XDAU
											8.10E-5		8.10E-5	69	XDAU
										8.02E-2	7.22E-2	6.88E-2	6.88E-3	70	XN
													6.20E-2	71	XDMU
												3.32E-3	3.32E-3	72	XDAU
											8.02E-3		8.02E-3	73	XDAU
							1.12E-5	1.12E-6					1.12E-6	74	XEQL
								1.01E-5	2.02E-6				2.02E-6	75	XESL
									8.10E-6				8.10E-6	76	XEUL
						3.37E-1	3.31E-1	3.31E-2	3.31E-2	1.55E-2	1.40E-2		1.40E-2	77	XN
											1.55E-3		1.55E-3	78	XDAQ
										1.75E-2	1.58E-2	1.57E-2	1.57E-2	79	XN
												4.73E-5	4.73E-5	80	XDAQ

Figure H-5: CR3 Containment Event Tree (CPET) for KPDS K3BA

IDENTIFICATION FOR KPDS: K3BA

KPDS	HL	DQ	HP	FP	DT	HS	FS	DC	CS	HD	CA	FD	BM	No.	R.C.
											1.75E-3		1.75E-3	81	XDAQ
								2.98E-1	5.95E-2	3.57E-3	3.21E-3	3.18E-3	3.18E-4	82	XN
													2.86E-3	83	XDMS
												3.21E-5	3.21E-5	84	XDAS
											3.57E-4		3.57E-4	85	XDAS
										5.60E-2	5.04E-2	4.88E-2	4.88E-3	86	XN
													4.39E-2	87	XDMS
												1.61E-3	1.61E-3	88	XDAS
											5.60E-3		5.60E-3	89	XDAS
									2.38E-1	1.43E-2	1.29E-2	1.27E-2	1.27E-3	90	XN
													1.15E-2	91	XDMU
												1.29E-4	1.29E-4	92	XDAU
											1.43E-3		1.43E-3	93	XDAU
										2.24E-1	2.01E-1	1.95E-1	1.95E-2	94	XN
													1.76E-1	95	XDMU
												6.45E-3	6.45E-3	96	XDAU
											2.24E-2		2.24E-2	97	XDAU
							6.75E-3	6.75E-4					6.75E-4	98	XEQL
								6.07E-3	1.21E-3				1.21E-3	99	XESL
									4.86E-3				4.86E-3	100	XEUL
				5.00E-5			5.00E-5	2.50E-5					2.50E-5	101	XEQL
								2.50E-5	2.25E-5				2.25E-5	102	XESL
									2.50E-6				2.50E-6	103	XEUL
			5.00E-1	4.97E-1	4.97E-2	3.11E-2	3.11E-2	1.55E-2	1.55E-2	7.30E-3	6.57E-3		6.57E-3	104	XN
											7.30E-4		7.30E-4	105	XDAQ
										8.23E-3	7.41E-3	7.39E-3	7.39E-3	106	XN
												2.22E-5	2.22E-5	107	XDAQ
											8.23E-4		8.23E-4	108	XDAQ
								1.55E-2	1.40E-2	8.39E-4	7.55E-4	7.55E-4	3.77E-4	109	XN
													3.77E-4	110	XDMS
												7.55E-8	7.55E-8	111	XDAS
											8.39E-5		8.39E-5	112	XDAS
										1.31E-2	1.18E-2	1.14E-2	5.72E-3	113	XN
													5.72E-3	114	XDMS
												3.78E-4	3.78E-4	115	XDAS
											1.31E-3		1.31E-3	116	XDAS
									1.55E-3	9.32E-5	8.39E-5	8.39E-5	4.19E-5	117	XN
													4.19E-5	118	XDMU
												8.39E-9	8.39E-9	119	XDAU
											9.32E-6		9.32E-6	120	XDAU
										1.46E-3	1.31E-3	1.27E-3	6.36E-4	121	XN
													6.36E-4	122	XDMU
												4.20E-5	4.20E-5	123	XDAU
											1.46E-4		1.46E-4	124	XDAU
							3.11E-6	1.55E-6					1.55E-6	125	XEQL
								1.55E-6	1.40E-6				1.40E-6	126	XESL
									1.55E-7				1.55E-7	127	XEUL
						1.86E-2	1.83E-2	9.13E-3	9.13E-3	4.29E-3	3.86E-3		3.86E-3	128	XN
											4.29E-4		4.29E-4	129	XDAQ
										4.84E-3	4.36E-3	4.34E-3	4.34E-3	130	XN
												1.31E-5	1.31E-5	131	XDAQ
											4.84E-4		4.84E-4	132	XDAQ
								9.13E-3	8.22E-3	4.93E-4	4.44E-4	4.44E-4	2.22E-4	133	XN
													2.22E-4	134	XDMS
												4.44E-8	4.44E-8	135	XDAS
											4.93E-5		4.93E-5	136	XDAS
										7.73E-3	6.95E-3	6.73E-3	3.37E-3	137	XN
													3.37E-3	138	XDMS
												2.23E-4	2.23E-4	139	XDAS
											7.73E-4		7.73E-4	140	XDAS
										9.13E-4	5.48E-5	4.93E-5	2.47E-5	141	XN
													2.47E-5	142	XDMU
												4.93E-9	4.93E-9	143	XDAU
											5.48E-6		5.48E-6	144	XDAU
										8.58E-4	7.73E-4	7.48E-4	3.74E-4	145	XN
													3.74E-4	146	XDMU
												2.47E-5	2.47E-5	147	XDAU
											8.58E-5		8.58E-5	148	XDAU
							3.73E-4	1.86E-4					1.86E-4	149	XEQL
								1.86E-4	1.68E-4				1.68E-4	150	XESL
									1.86E-5				1.86E-5	151	XEUL
					4.47E-1	2.80E-1	2.80E-1	2.80E-2	2.80E-2	1.31E-2	1.18E-2		1.18E-2	152	XN
											1.31E-3		1.31E-3	153	XDAQ
										1.48E-2	1.33E-2	1.33E-2	1.33E-2	154	XN
												4.00E-5	4.00E-5	155	XDAQ
											1.48E-3		1.48E-3	156	XDAQ
								2.52E-1	5.03E-2	3.02E-3	2.72E-3	2.69E-3	2.69E-4	157	XN
													2.42E-3	158	XDMS
												2.72E-5	2.72E-5	159	XDAS
											3.02E-4		3.02E-4	160	XDAS
										4.73E-2	4.26E-2	4.12E-2	4.12E-3	161	XN

Figure H-5: CR3 Containment Event Tree (CPET) for KPDS K3BA

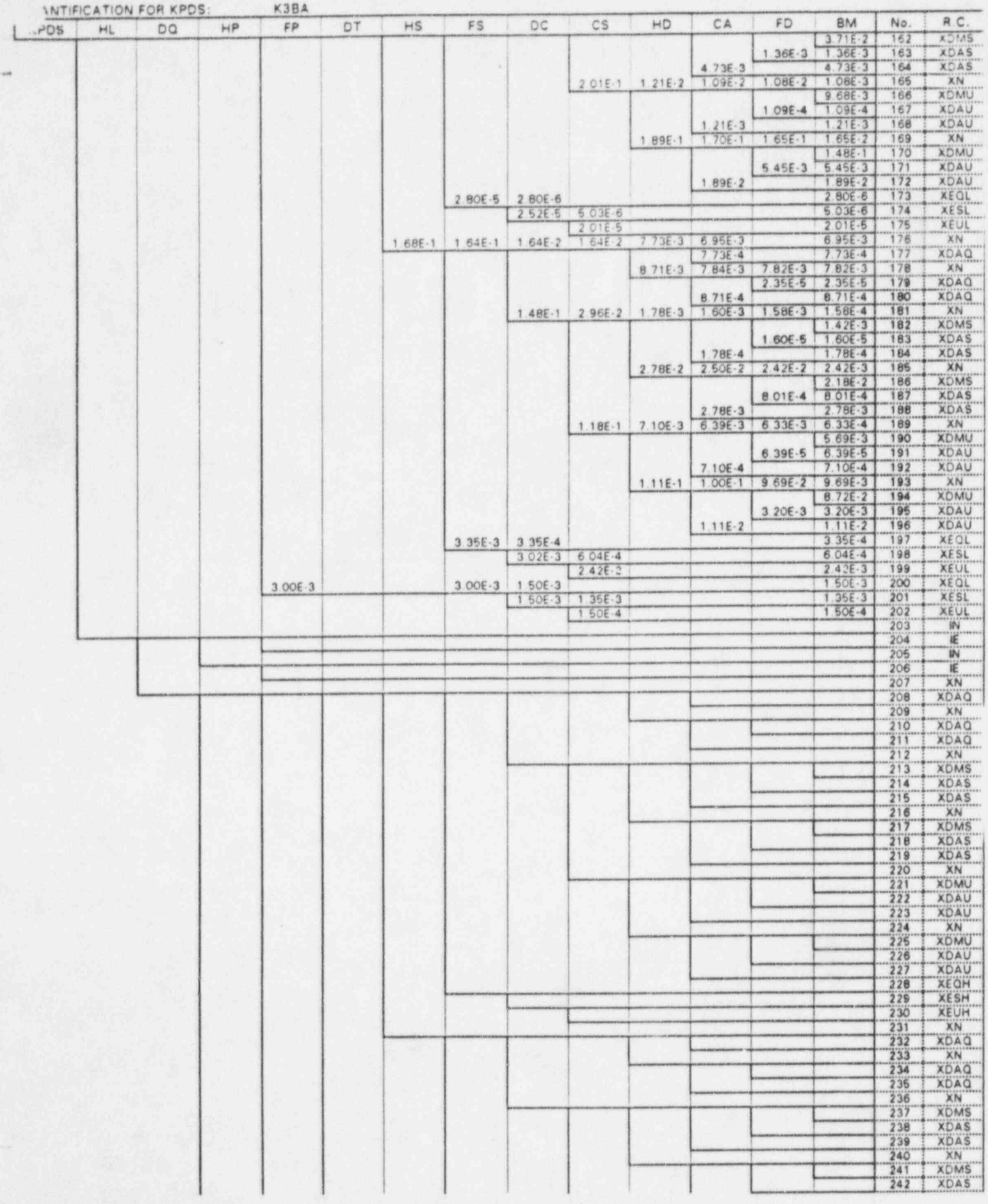

Figure H-5: CR3 Containment Event Tree (CPET) for KPDS K3BA

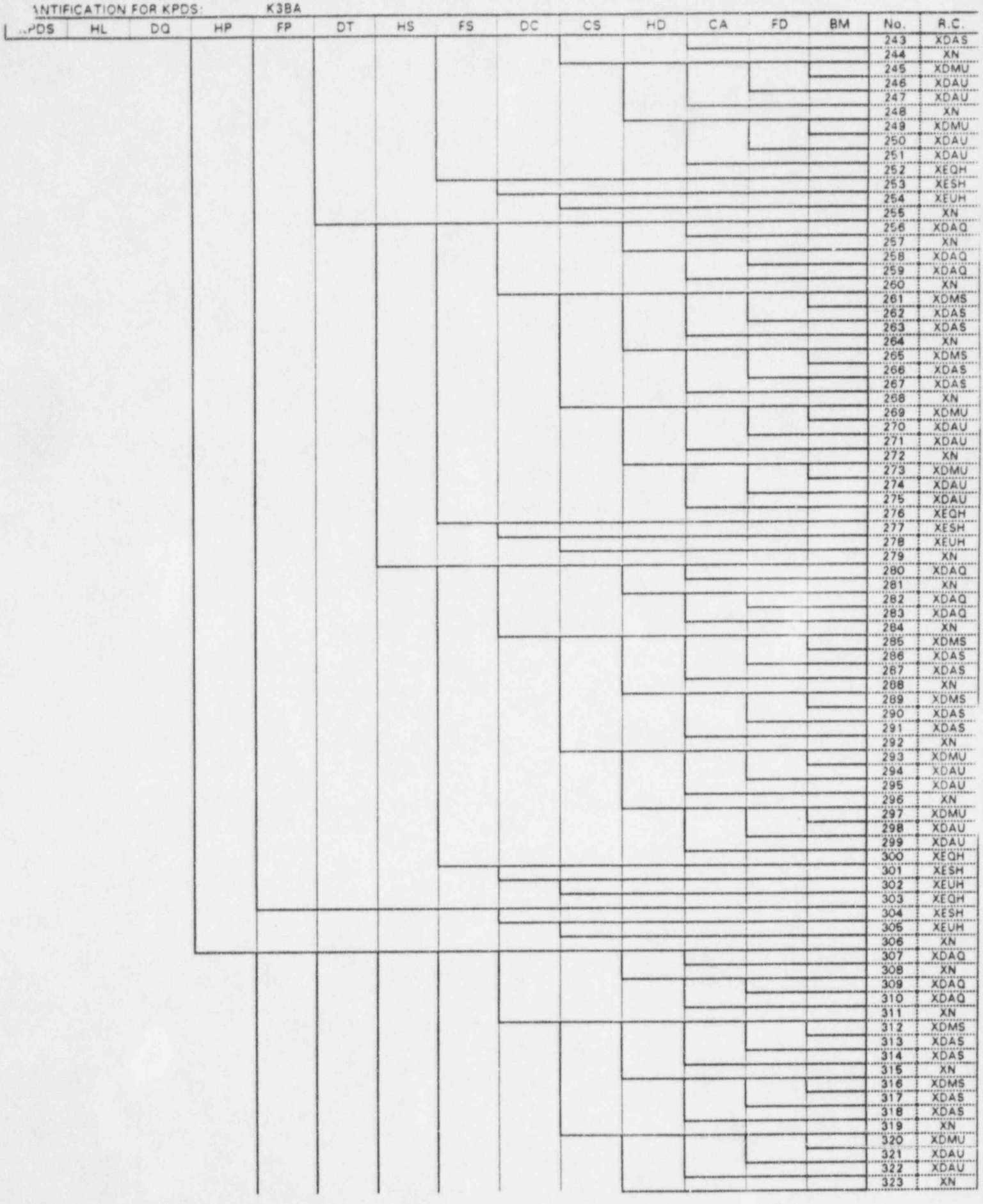

Figure H-5: CR3 Containment Event Tree (CPET) for KPDS K3BA

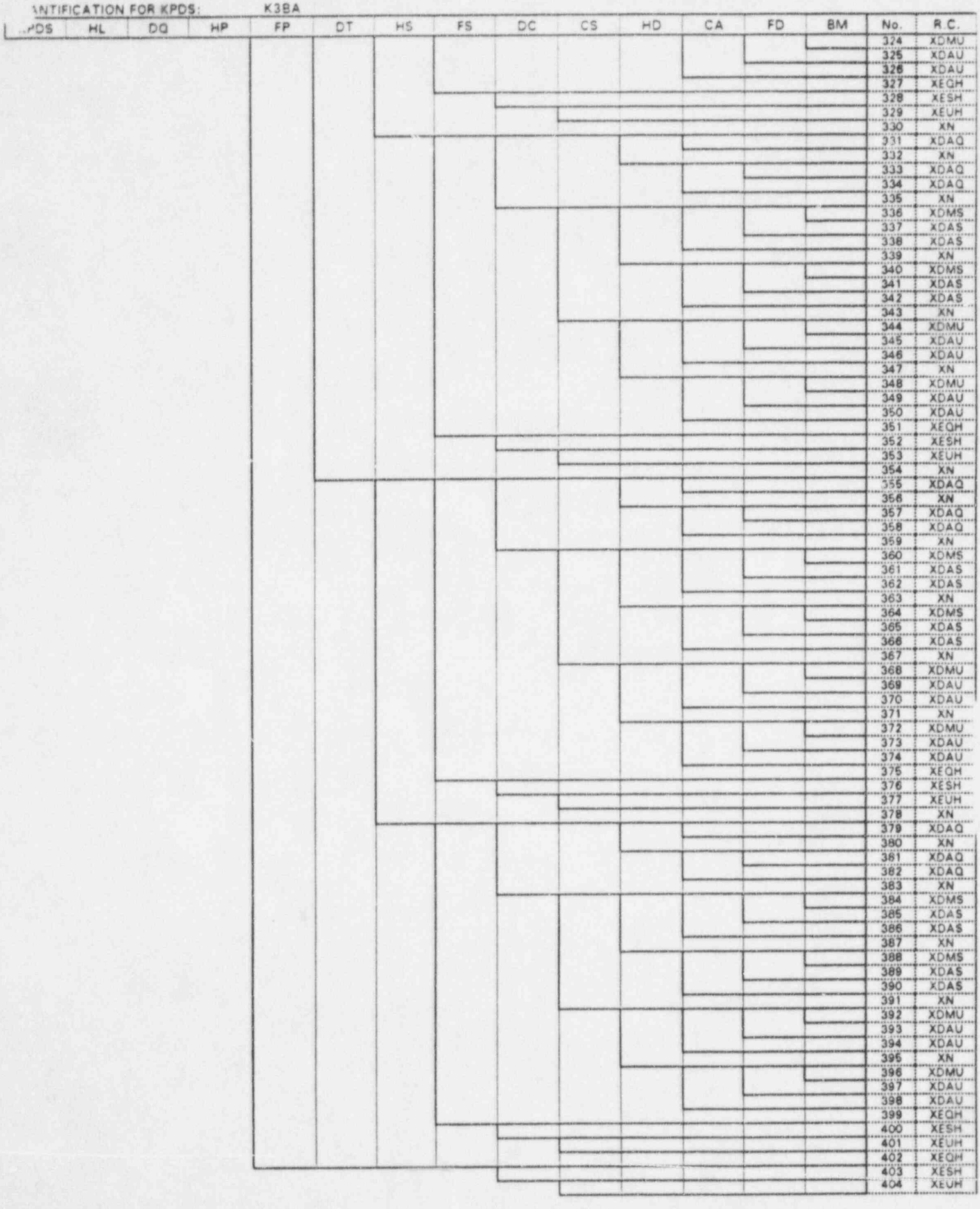

Appendix I: Disposition of Key Event Tree Considerations

This appendix describes how each of key phenomenological issues defined in Tables 2.2 and A.5 of NUREG-1335 were dealt with in the CR3 IPE Level 2 model. Table 2.2 defines potential containment failure modes and mechanisms, whereas Table A.5 addresses parameters that are considered to have significant phenomenological uncertainties.

I.1 Containment Failure Modes and Mechanisms

This section addresses the containment failure mode sensitivities identified in Table 2.2 of NUREG-1335.

I.1.1 Direct Containment Bypass

Bypass containment failure modes were considered as separate initiating events in the Level 1 model and assigned to a specific group of bypass PDS identified by the last three columns of the PDS Matrix shown in Table 4.3-3 of the submittal.

I.1.2 Failure to Isolate

Containment isolation failures were explicitly considered in the Level 1 model. Sequences with small penetrations isolation failures (< 3 inches in diameter) were assigned to the small containment failure group identified by the letters "E, F, G or H" as the second character in the PDS designator. Sequences with large penetrations isolation failures (> 3 inches in diameter) were assigned to the large containment failure group identified by the letter "I or J" as the second character in the PDS designator. These two containment isolation failure groups were separately considered in the Level 2 analysis.

I.1.3 Vapor Explosions

Vapor explosions which cause the reactor vessel head to become a missile that penetrates and fails the containment were considered by the NRC's steam explosion review group. The probability of this event occurring when the molten debris slumps to the bottom of the reactor vessel was concluded to be very low, on the order of 1E-4. If this event were postulated to occur at this probability, the frequency of the resulting early containment failure would be a factor of 1000 lower than the frequency of the dominant early containment failure sequence. Therefore, the CR3 IPE Level 2 results are not sensitive to assumptions about the probability of alpha-mode (steam explosion) containment failures, unless this probability is postulated to be on the order of 0.1 or larger.

I.1.4 Overpressurization

Containment failure due to overpressurization both due to steam and non-condensable gases is explicitly addressed in three distinct top events in the CPET, namely before vessel breach (FP), at vessel breach (FS) and late in the accident sequence (FD).

I.1.5 Combustion Processes

Hydrogen burns in the containment are explicitly considered in three distinct top events in the CPET, namely before vessel breach (HP), at vessel breach (HS) and late in the accident sequence (HD).

I.1.6 Core Concrete Interaction

Containment failure due to basemat penetration from core concrete interaction is explicitly considered in CPET top event BM for late basemat meltthrough.

I.1.7 Blowdown Forces

Vessel thrust forces during a high pressure vessel meltthrough exert forces on the reactor vessel in the upward direction. If a vessel meltthrough failure is postulated to occur away from the vessel bottom area, and if it is postulated to propagate around the vessel circumference, then larger forces can be exerted on the vessel in the upward direction, up to a maximum force bounded by the vessel pressure multiplied by the inside cross-sectional area of the vessel. This maximum cross sectional area failure could be outside the vessel support skirt and the force would be resisted by the hot legs and cold legs penetrating through the biological shield. Such a failure mode can be postulated to occur due to a creep rupture of the vessel circumference at the top of the debris pool. If this failure mode is postulated to occur before vessel depressurization occurs, then an early containment failure would be possible, either by the vessel impacting on the missile shield and containment dome.

In vessel designs with bottom instrument penetrations, like the CR3 design, vessel failure is expected to occur at one or several of the instrument penetrations inside the vessel support skirt, and not by this circumferential failure mode. Therefore the circumferential failure mode was not considered.

I.1.8 Liner Meltthrough

Liner meltthrough is a BWR issue, and it was not addressed in the CR3 IPE analysis.

I.1.9 Thermal Attack of Penetrations

Local or leak before break failure modes, including thermal attack of penetrations has been analyzed in several other IPEs and PRAs for large dry PWRs. They generally show local failure modes to occur at 10 to 20 psi lower than the first gross failure mode,

and generally in the vicinity of 130 to 140 psid. Since the lowest structural containment failure mode for the CR3 containment was identified at a pressure of 140 psi (at 300°F) to 122 psig (at 800°F), it was conservatively assumed that all containment failures would occur by the leading structural failure mode at the basemat to cylindrical wall juncture. For this reason local or leak before break failure modes were not analyzed.

I.2 Accident Phenomenology and Parameter Sensitivity

This section addresses the phenomenological and parameter sensitivities identified in Table A.5 of NUREG-1335.

I.2.1 Containment Heat Removal

The availability of containment heat removal is explicitly considered in the Containment Systems Event Tree (CSET) analysis. Four containment heat removal states are considered (containment heat removal and fission product scrubbing, containment heat removal only, containment fission product scrubbing only and no heat removal and scrubbing). Separate PDS columns were defined for each case and sequences are assigned to separate PDS bins for each containment heat removal state.

I.2.2 In-Vessel Phenomena - high vessel pressure

a. Hydrogen production and combustion: The MARCH3/CONTAIN calculation results were considered as best estimates and uncertainties were explicitly considered in the CPET quantification of the three hydrogen burn top events.

b. Induced RCS failure: The probability of an induced hot leg creep rupture after core uncovery is addressed in CPET top event HL, but it was not found to be numerically significant for the OSTG design.

c. Core relocation characteristics: These are considered in CR3 specific MARCH3 model. However, no sensitivity analyses for different blockage assumptions were performed due to the low importance of the hot leg and steam generator tube creep rupture issue.

d. Mode of reactor vessel failure: Downward vessel meltthrough at one or more instrument penetrations inside the vessel support skirt is considered the expected failure mode for bottom instrument tube designs. Therefore, other failure modes were not considered to be significant.

I.2.3 In-vessel phenomena - low vessel pressure

a. Hydrogen production and combustion: The MARCH3/CONTAIN calculation results were considered as best estimates and uncertainties were explicitly considered in the CPET quantification of the three hydrogen burn top events.

b. Core relocation characteristics: Same as Item I.2.2 (c) above.

c. Fuel coolant interactions: The effect and sensitivity to in-vessel fuel coolant interactions is addressed in Section I.1.3.

d. Mode of reactor vessel failure: Same as Item I.2.2 (d) above.

I.2.4 Ex-vessel phenomena - high vessel pressure

a. Direct containment heating: The potential and the effects of direct containment heating are explicitly considered in CPET top event DT, and the impact of DCH on containment integrity is explicitly considered in the quantification of top event FS.

b. Early containment failure due to pressure loads: The probability of early containment failure due to the pressure transient resulting from an early hydrogen burn is explicitly addressed in top event FP. The probability of early containment failure due to the pressure transient resulting from a high pressure vessel meltthrough is explicitly addressed and modeled in CPET top event FP, and it considers the effects of blowdown forces, hydrogen burns and DCH at the time of vessel failure.

c. Debris disposition and debris coolability: The CR3 IPE Level 2 analysis considered the debris disposition depending on the RCS pressure at vessel meltthrough. For high pressure sequences dispersal through overpressure failure of the two cavity access crawl tunnel doors and for low pressure sequences meltthrough of the doors by direct exposure to core debris and debris flow from the cavity through the cavity access crawl tunnel into the lower compartment was considered. In each case a debris bed of at least one foot in depth remaining in the reactor cavity was considered. Debris coolability, and the effects of the resulting core concrete interaction on containment failure and on the source term were explicitly modeled and assessed depending on the resulting debris configuration.

I.2.5 Ex-vessel phenomena - low vessel pressure

a. Early containment failure due to liner meltthrough: Liner meltthrough after vessel breach is a BWR issue, and it was not explicitly addressed.

b. Long-term core-concrete interactions: Core concrete interactions, non-condensable and flammable gas generation, and concrete penetration was explicitly considered in the CONTAIN model and calculations. These effects and the uncertainties associated with them on the time of containment failure and on the containment failure mode were explicitly considered in the quantification of split fractions for CPET top events DC, HD, FD and BM.